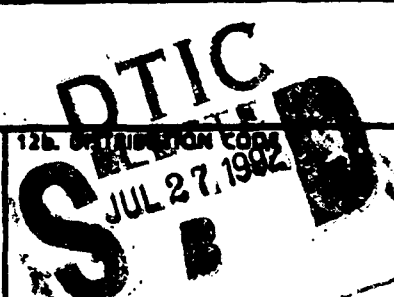


AD-A253 402 TATION PAGE

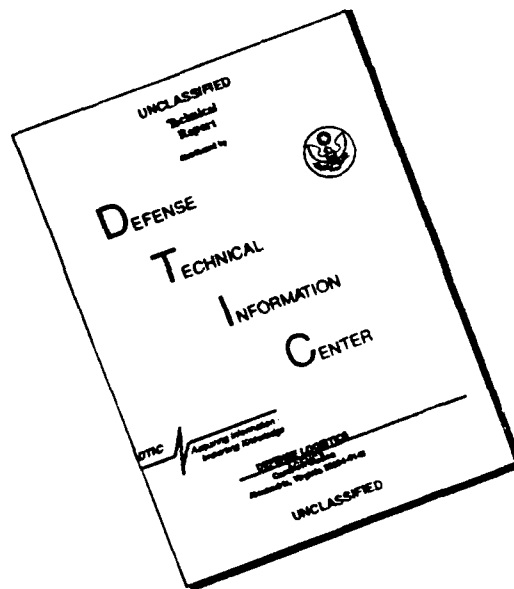


Form Approved
OMB No. 0704-0188

to average 1 hour per response, including the time for reviewing instructions, searching existing data sources, gathering the collection of information, send comments regarding this burden estimate or any other aspect of this report, to Washington Headquarters Services, Directorate for Information Operations and Reports, 1215 Jefferson Ave of Management and Budget, Paperwork Reduction Project (0704-0188), Washington, DC 20503.

1. AGENCY USE ONLY (Leave blank)		2. REPORT DATE		3. REPORT TYPE AND DATES COVERED	
				Final 10 Nov 88 To 31 Oct 91	
4. TITLE AND SUBTITLE				5. FUNDING NUMBERS	
Studies of collisional and nonlinear radiative processes for development of coherent UV and XUV Sources				AFOSR-89-0159	
6. AUTHOR(S)					
Professor Charles Rhodes and Ting Shan Luk					
7. PERFORMING ORGANIZATION NAME(S) AND ADDRESS(ES)				8. PERFORMING ORGANIZATION REPORT NUMBER	
University of Illinois @ Chicago Dept of Physics Chicago, IL 60680				AFOSR-77-02 0682	
9. SPONSORING/MONITORING AGENCY NAME(S) AND ADDRESS(ES)				10. SPONSORING/MONITORING AGENCY REPORT NUMBER	
AFOSR/NE Bldg 410 Bolling AFB DC 20332-6448 Schlossberg				2301/A1	
11. SUPPLEMENTARY NOTES		DISTRIBUTION STATEMENT A			
		Approved for public release; Distribution Unlimited			
12a. DISTRIBUTION / AVAILABILITY STATEMENT				12b. DISTRIBUTION CODE	
UNLIMITED				S B	
13. ABSTRACT (Maximum 200 words) Studies of the interaction of matter with high intensity radiation (greater than or equal to 10^{16} W/cm ²) are leading to the observation of new physical phenomena and the production of new classes of highly excited matter. These recently factor in the discussions is the ability to generate very high levels of electronic excitation in the manner which enables the system to remain kinetically cold for the time scale of the interaction. This conventionally paradoxical situation, in alliance with the existence of a new high-field mode of channeled propagation is highly conducive to coherent x-ray generation under a rather wide range of circumstances.					
14. SUBJECT TERMS				15. NUMBER OF PAGES	
				16. PRICE CODE	
17. SECURITY CLASSIFICATION OF REPORT	18. SECURITY CLASSIFICATION OF THIS PAGE	19. SECURITY CLASSIFICATION OF ABSTRACT	20. LIMITATION OF ABSTRACT		
UNCLASS	UNCLASS	UNCLASS	III		

DISCLAIMER NOTICE



THIS DOCUMENT IS BEST QUALITY AVAILABLE. THE COPY FURNISHED TO DTIC CONTAINED A SIGNIFICANT NUMBER OF PAGES WHICH DO NOT REPRODUCE LEGIBLY.

Laboratory for Atomic, Molecular, and Radiation Physics (M/C 273)
Department of Physics
College of Liberal Arts and Sciences
Box 4348, Chicago, Illinois 60680-4348
(312) 996-4868 Fax: (312) 996-8824

4 June 1992

FINAL TECHNICAL REPORT

**STUDIES OF COLLISIONAL AND NONLINEAR RADIATIVE
PROCESSES FOR DEVELOPMENT OF
COHERENT UV AND XUV SOURCES**

GRANT NUMBER: AFOSR-89-0159

PRINCIPAL INVESTIGATOR: Charles K. Rhodes

CO-INVESTIGATORS: Ting Shan Luk
Armon McPherson
Keith Boyer

PROGRAM MANAGER: Dr. Howard Schlossberg
Air Force Office of Scientific Research/NP
Building 410, Room C219
Bolling Air Force Base
Washington, D. C. 20332

SUBMITTED TO: Joyce A. Burch
Procurement Assistant
Air Force Office of Scientific Research
Bolling Air Force Base
Washington, D. C. 20332-6448

92 7 23 068

92-19919



TABLE OF CONTENTS

ABSTRACT	1
I. INTRODUCTION	2
II. GENERAL DISCUSSION OF RESEARCH	2
A. Laser Technology	2
B. Studies of Ion Production	7
1. Atoms	7
2. Molecules	15
a. Atomic Ion Production	16
b. Molecular Site-Specific Energy Deposition	20
c. Diatomic Ion Yields	23
C. Radiation Studies	24
1. Fluorescence from Atomic Ions	26
2. Fluorescence from Ionic Molecules	32
3. X-Ray Generation from Solid Targets	35
III. DISCUSSION OF NEW POSSIBILITIES	42
A. Molecular Processes for X-Ray Generation	42
B. Hard X-Ray Generation from Solid Targets	48
C. General Consideration of Multiquantum Strong-Field Excitation	49
1. Inner-Electron Excitation	49
2. General Features of Strong-Field Coupling	49
D. Strong-Field Propagation	59
IV. SUMMARY AND CONCLUSIONS	61
V. REFERENCES	62
VI. APPENDICES	72
Appendix A: "Measurement of Energy Penetration Depth of Subpicosecond Laser Energy into Solid Density Matter"	73
Appendix B: "High Intensity Generation of 9-13 Å X-Rays from BaF ₂ Targets"	77
Appendix C: "Plasma Production from Ultraviolet Transmitting Targets Using Subpicosecond Ultraviolet Radiation"	80
Appendix D: "Studies of the Interaction of Molecules and Solids with Intense Subpicosecond 248 nm Radiation"	84
Appendix E: "Stable Channeled Propagation of Intense Radiation in Plasma Arising from Relativistic and Charge-Displacement Mechanisms"	96
Appendix F: "Observation of Relativistic and Charge-Displacement Self-Channeling of Intense Subpicosecond Ultraviolet (248 nm) Radiation in Plasmas"	107
Appendix G: "Relativistic and Charge-Displacement Self-Channeling of Intense Ultrashort Laser Pulses in Plasmas"	112
Appendix H: "X-Ray Amplifier Energy Deposition Scaling with Channeled Propagation"	129

**STUDIES OF COLLISIONAL AND NONLINEAR RADIATIVE
PROCESSES FOR DEVELOPMENT OF
UV AND XUV SOURCES**

ABSTRACT

Studies of the interaction of matter with high intensity radiation ($\geq 10^{16}$ W/cm²) are leading to the observation of new physical phenomena and the production of new classes of highly excited matter. These recently discovered processes involve atoms, molecules, solids, and dense plasmas. A central factor in the discussion is the ability to generate very high levels of electronic excitation in a manner which enables the system to remain kinetically cold for the time scale of the interaction. This conventionally paradoxical situation, in alliance with the existence of a new high-field mode of channeled propagation, is highly conducive to coherent x-ray generation under a rather wide range of circumstances.

DTIC QUALITY INSPECTED 4

Accession For	
NTIS GRA&I	<input checked="" type="checkbox"/>
DTIC TAB	<input type="checkbox"/>
Unannounced	<input type="checkbox"/>
Justification	
By	
Distribution/	
Availability Codes	
Dist	Avail and/or Special
A-1	

I. INTRODUCTION

The controlled concentration of power in materials is the fundamental issue for the creation of bright sources of radiation in the x-ray range. If amplification is desired, this issue acquires a heightened prominence, since gain at these wavelengths (1–10 Å) requires truly prodigious energy deposition rates¹ spatially organized in a high-aspect-ratio volume of matter. The confluence of advances in femtosecond laser technology, the results of a range of physical measurements, and theoretical analysis all suggest that electromagnetic coupling, in the strong-field regime ($E \gg e/a_0$), may be capable of establishing the demanding conditions necessary for such amplification.² In addition, there is a growing body of evidence that fundamentally new forms of highly excited matter can be produced with strong-field interactions. Therefore, subjects of marked significance concerning the generation of radiation at x-ray wavelengths with strong-field coupling are (1) mechanisms leading to high levels of electronic excitation, particularly those involving ionization and the excitation of inner-shell states, (2) the characteristics of matter which govern the efficiency and specific power of x-ray generation, and (3) the physical processes determining the propagation of intense waves in plasmas. These three basic questions, and others related directly to them, are the subjects of this report.

II. GENERAL DISCUSSION OF RESEARCH

A. Laser Technology

Advances in femtosecond lasers are extending the exploration of multiphoton interactions well into the regime for which the external field is greater than an atomic unit (e/a_0). The performance projected for ultraviolet rare gas halogen technology is currently being realized²⁻¹¹ and new near-infrared solid state systems, such as $\text{Ti:Al}_2\text{O}_3$, are under vigorous development. Both technologies¹² should reach a field strength of $\sim 100 e/a_0$ with instruments that produce an output

energy of ~ 1 J. With these experimental tools, intensities approaching 10^{21} W/cm² will be available, a value comparable to that produced by radiating matter under vigorous thermonuclear conditions.

The KrF* (248) nm source used for the studies discussed herein is schematically shown in Fig. (1). This instrument has an output pulse width of ≈ 600 fs, a typical output pulse energy in the 300–400 mJ range, and good focusability,⁹ nominally within a factor of two of the diffraction limit. For example, with a simple f/10 CaF₂ lens, peak intensities of $\sim 10^{17}$ W/cm² are produced even though such a lens exhibits appreciable spherical aberration. This intensity corresponds to a peak electric field somewhat above one atomic unit. The application of more sophisticated focusing systems can clearly generate substantially greater field strengths.^{9,10}

A recent modification has incorporated a Ti:Al₂O₃ amplifier into the system for amplification of the radiation at 745 nm. This change has resulted in approximately a 40-fold increase in the 248 nm output energy from the crystals to a value of ~ 40 μ J. This enables the generation of a significantly more intense seed beam to drive the power amplifier. The use of Ti:Al₂O₃ to provide radiation at 745 nm greatly enhances the performance of the overall laser system. In addition, modifications of the power amplifier will be made this spring that are expected to raise the output energy to ~ 1 J or, perhaps, somewhat above.

A more detailed characterization of the pulse shape¹³ for this system is becoming available with the use of a technique involving a third order intensity correlation¹⁴. The data shown in Fig. (2) illustrate the character of the pulse shape observed at point A in Fig. (1). One of the properties is a clearly observed asymmetry in the profile of the pulse, in our case a waveform that rises more rapidly than it falls. The pulse width measured is $\tau \sim 260$ fs.

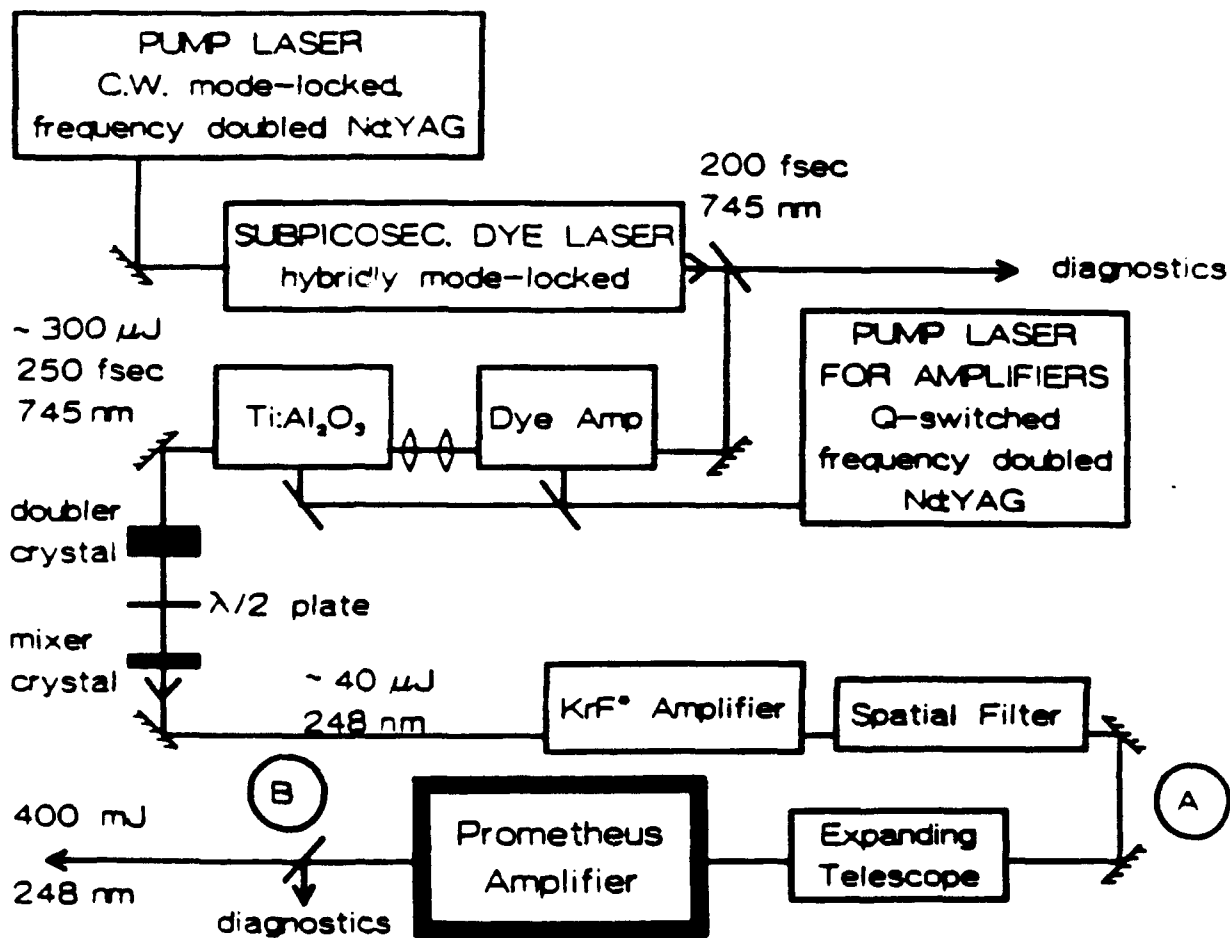


Fig. (1): Schematic showing the configuration of the ultrahigh-intensity KrF* laser system used in the studies discussed in the text.

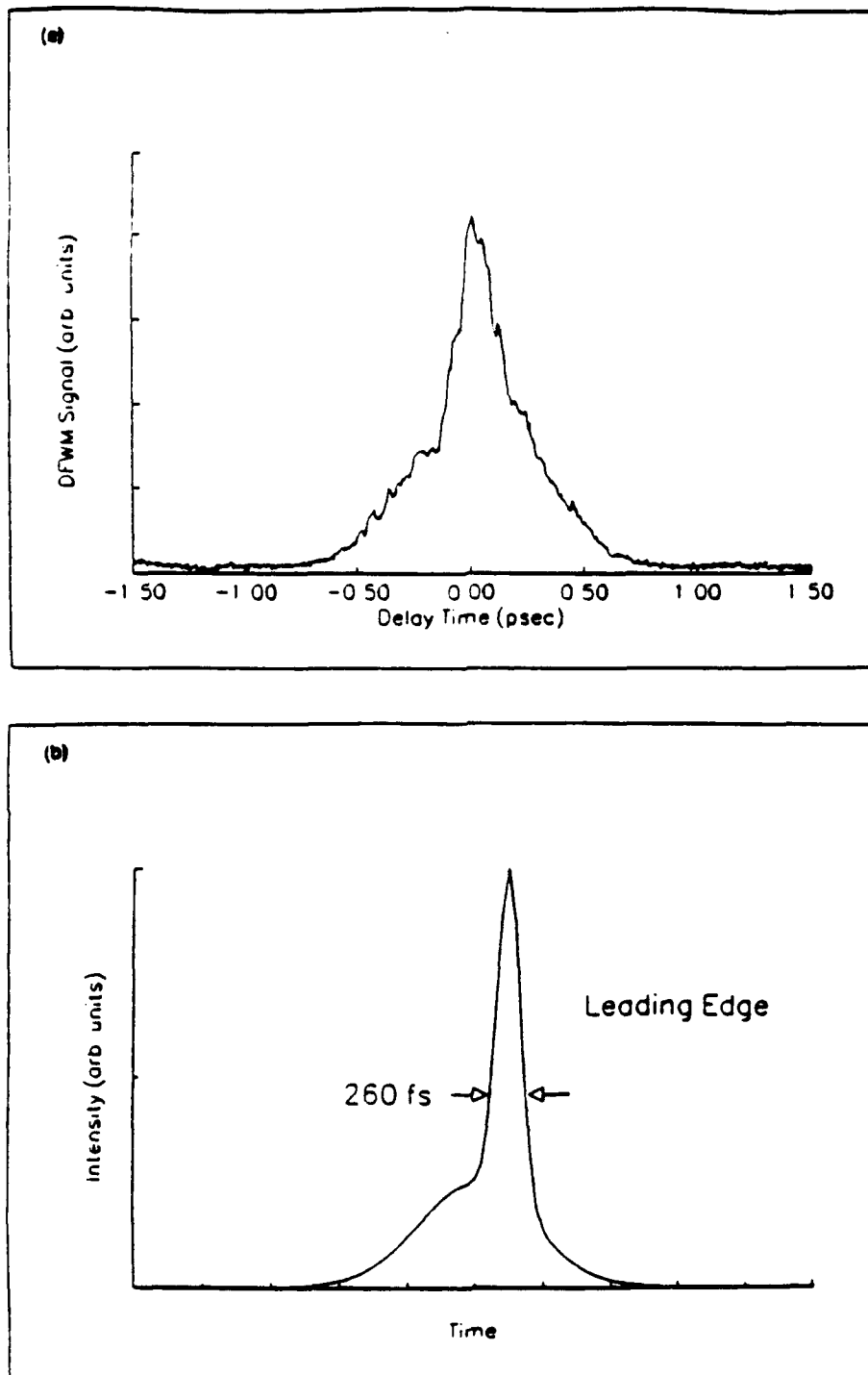


Fig. (2): Measurement of 248 nm pulse width taken at point (A) in Fig. (1) using 4-wave mixing process. (a) Measured third-order autocorrelation function of 260 fs pulse showing clear asymmetry. (b) Temporal profile of pulse derived from (a).

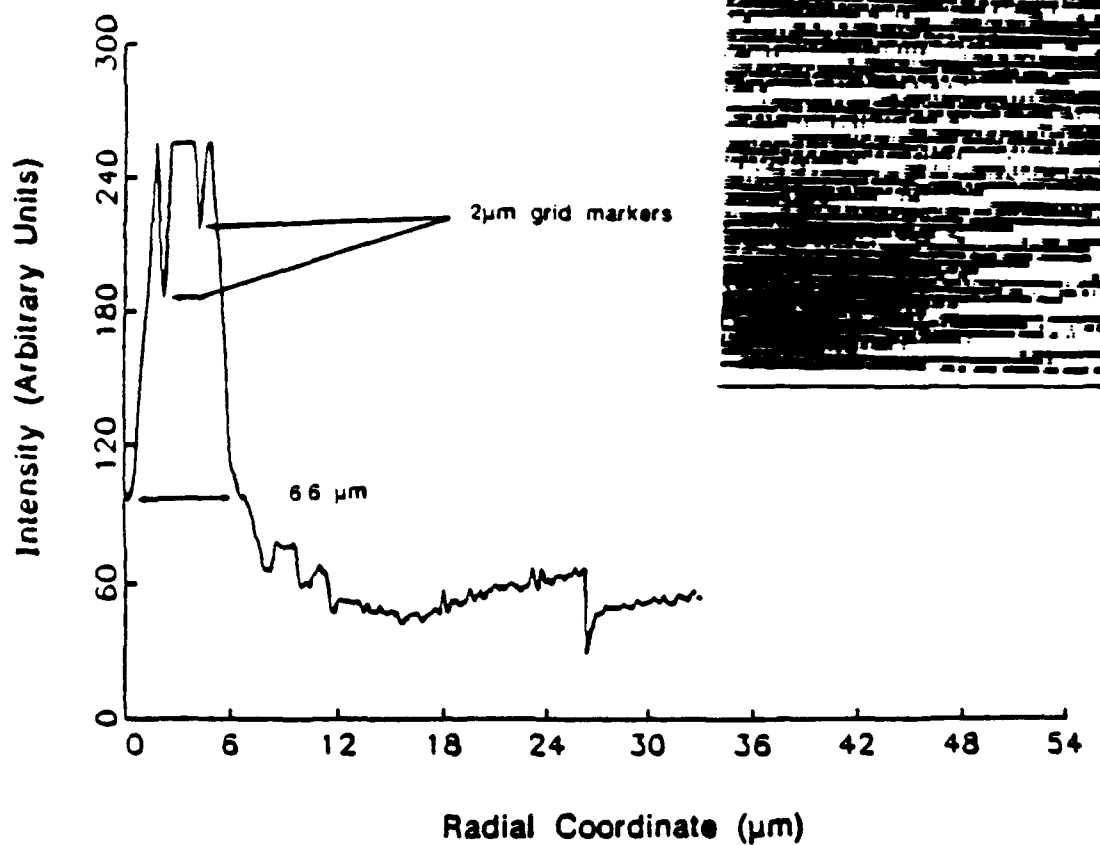


Fig. (3): Spatial intensity distribution of the 248-nm seed beam using an f/7 optical system measured for a 4.2 cm diameter beam. The diameter at the 1/e point is 6.6 μm a value which is ~ 1.5-fold the theoretical limit (4.2 μm). The dips are the 2 μm grid markers.

The ability to concentrate the pulse energy in a small focal zone is another crucial property necessary for the generation of high field strengths. Fig. (3) illustrates the focal spot measured at point B in Fig. (1) with an $f/7$ focusing system. The measured diameter of the focal zone is $\sim 6.6 \mu\text{m}$, a value which corresponds to ~ 1.5 -fold the diffraction limit.

This subpicosecond KrF^* (248 nm) laser system has been used to explore the coupling of intense radiation to atoms, molecules, and solids. The findings of these experimental studies are discussed in the following sections.

B. Studies of Ion Production

Studies of collision-free ionization have been a valuable source of information on multiphoton processes¹⁵⁻¹⁸. In particular, such experiments give a direct and unambiguous measure of the scale of the energy transfer occurring between the radiation field and the free atomic or molecular target. Although most studies have been conducted with atoms, recent work has begun to examine molecules, including certain polyatomic systems. The results obtained with both classes of materials are discussed below.

1. Atoms

Studies of atomic ion production have examined several aspects of the multiphoton interaction including (1) the intensity dependence,¹⁹⁻²² (2) the atomic number (Z) dependence,^{2,17} (3) the frequency dependence,^{18,23} and (4) the dependence upon pulse width.²¹ Important related data concerning the mechanism of ionization has also come from numerous photoelectron studies²⁴⁻²⁶, work which has accounted for the influence of the optical stark effect.²⁷⁻³⁰

Several models^{21,22,31-37} have been used to interpret the extant data on collision-free multiphoton ionization of the rare gases. If the customary distinction founded on the Keldysh parameter³¹ is made, which separates the multiphoton (γ

>> 1) and tunneling ($\Upsilon \ll 1$) regimes based on the magnitudes of the ionization and ponderomotive potentials, theories have been developed for both the former³¹⁻³³ and the latter,^{21,34-37} respectively.

A tunneling picture has recently been applied to data concerning threshold ionization of the rare gases in the infrared²¹ (1.06 μm) and ultraviolet²² (248 nm) spectral regions. For the infrared study, the data all conformed to the conventional tunneling regime ($\Upsilon < 1$), and good agreement was found between the experimental results and the theory. However, since the ponderomotive potential varies as the square of the wavelength, the data for the ultraviolet experiments corresponded to conditions significantly outside ($\Upsilon > 1$) of the validity of the normal tunneling analysis. Interestingly, although the ultraviolet study²² involved the Keldysh parameter in the range $1 < \Upsilon < 8$, reasonable agreement with the pure tunneling formulation was still found for the threshold intensities occurring in the $10^{13} - 10^{16} \text{ W/cm}^2$ range.

Figure (4a) presents the experimental data on the threshold ionization intensities of the rare gases observed with 248-nm irradiation.³⁸ Clearly, a meaningful statement of a threshold intensity requires some discussion of the ionization rate defining the limit (threshold) of observation. In these experiments, the ionization rate at threshold was estimated³⁸ to be $\sim 2 \times 10^9 \text{ s}^{-1}$. However, for all the models considered below, calculations show that only a factor of two change in intensity, either way around this threshold value, alters the ionization rate by at least two orders of magnitude. Thus, it is not necessary to know the threshold ionization rate to high accuracy in order to define the threshold intensity within relatively narrow limits.

Two important features in Fig. (4a) are readily apparent. Firstly, there is no obvious functional dependence of the threshold ionization intensity I_{th} on the ionization potential E_p , and second, a systematic lowering of I_{th} with increasing

atomic number exists. These two salient characteristics have been basic aspects of the data on multiphoton ionization originating with some of the earliest observations¹⁷ of these processes.

The simplest model of tunneling ionization consists of a one-dimensional (1-D) coulomb potential.²¹ In an external static electric field, an electron in this 1-D atom sees a finite potential barrier to ionization whose width and height depend on the strength of the field. The threshold intensity I_{th} for ionization can then be defined as the intensity at which the potential barrier is reduced to the ionization potential of the atom, the situation allowing for classically allowed escape of the electron. The result²¹ of this picture is the relationship

$$I_{th} = cE_p^4 / 128\pi e^6 Z^2, \quad (1)$$

where E_p , Z , c , and e are the ionization potential, the charge of the resulting ion, the speed of light, and the charge of an electron, respectively.

This model has two inherent defects which tend to cancel each other resulting in a fairly accurate prediction of I_{th} . First, when the barrier is lowered to the ionization potential, the barrier is completely removed producing ionization rates characteristic of atomic time scales ($\sim 10^{16} \text{ s}^{-1}$). Since a rate of this magnitude is much higher than the applicable threshold rate, the resulting value of the threshold ionization intensity tends to be overestimated. However, in contrast to the 1-D picture, the lowering of the potential barrier to the ionization potential for a three dimensional (3D) atom at the intensity given by Eq.(1), will occur in only a single spatial direction. In all other directions the potential barrier will be higher, a situation leading to an underestimation of the threshold ionization intensity.

Eq.(1) reveals two important scaling relationships despite these corrections. It shows that besides a dependence on E_p , I_{th} also depends inversely on Z^2 . This

latter scaling factor can be accounted for by simply considering the combined variable $I_{th} \cdot Z^2$. In addition, the variable $I_{th} \cdot Z^2$ varies in direct proportion to E_p^4 . Clearly, a plot of $I_{th} \cdot Z^2$ versus E_p should exhibit these basic scaling relationships and Fig. (4b) shows such a representation for the data illustrated in Fig. (4a). The experimental data are seen to fall almost perfectly on a straight line with a slope of four and the systematic dependence on atomic number has been significantly reduced. Furthermore, this agreement for the threshold intensities occurs over a span of five orders of magnitude in the parameter $I_{th} \cdot Z^2$. Nevertheless, the values of Eq.(1) appear consistently too high and there remains a more complex detailed dependence on the atomic number.

More sophisticated formulations of this process have been developed. For example, an improved model involves a 3-D atom and the calculation of the tunneling rate through the potential barrier at an arbitrary intensity.^{34,35} The resulting ionization rate for a static electric field in this theory³⁹ is given by

$$W_{st}(E_s) = 4\omega_0(2E_p)^{5/2}E_s^{-1} \exp(-2/3(2E_p)^{3/2}E_s^{-1}), \quad (2)$$

for $(2E_p)^{3/2} \gg E_s$, where E_s is the static field in atomic units (e/a_0), E_p the ionization potential in atomic units (e^2/a_0), and ω_0 the atomic frequency in atomic units ($4.1 \times 10^{16} \text{ s}^{-1}$). In order to compute the ionization rate generated, Eq.(2) can be time-averaged over one cycle of the field. This time average can be done exactly in terms of the K_0 modified Bessel function.⁴⁰ However, in the limit $(2E_p)^{3/2} \gg E_s$, the expression for the average reduces to a simpler form given by³⁶

$$W_{ac} = (3/\pi)^{1/2} E^{1/2} (2E_p)^{-3/4} W_{st}(E), \quad (3)$$

where E is the peak of the alternating field in atomic units.

Eq.(3) can be further improved to include non-hydrogenic systems. The static ionization rate in this orbital picture is given by^{36,37}

$$W_{st} = \omega_0 C_{n^*l}^2 E_p \frac{(2l+1)(l+|m|)!}{2^{|m|}(|m|)!(l-|m|)!} \left(2(2E_p)^{3/2} E^{-1} \right)^{2n^*-|m|-1} \exp(-2/3(2E_p)^{3/2} E^{-1}), \quad (4)$$

where n^* is the effective principle quantum number [$n^*=Z(2E_p)^{-1/2}$], l the orbital angular quantum number, and m the magnetic quantum number. C_{n^*l} is a numerical constant on the order of two. The approximate time average of Eq.(4) is also given by Eq.(3).

The last treatment that we consider is the well known Keldysh theory.³¹ Since the γ parameter is in the intermediate regime, $1 < \gamma < 8$, a limiting form⁴¹ of the theory is not valid and the full form is necessary.

Figures (5a) through (5c) compare the experimental data for He, Ar, and Xe from Fig. (5) with the results of the four models represented by Eq.(1), Eq.(3) using the static ionization rates for the hydrogenic and nonhydrogenic systems, and the Keldysh theory, respectively. Several features are manifest. First, both the 3-D simple atom picture and the Keldysh theory agree well with the experimental results for helium. However, they become consistently worse for the heavier atoms particularly at the higher charge states. This trend makes sense as these models assume exact hydrogenic potentials, a poor approximation for the heavier atoms. Second, as noted above, the 1-D model uniformly gives too high a threshold intensity and tends to be least successful in describing the neutral species. Third, the 3-D complex model, expressed by Eq.(4), consistently gives reasonable agreement over the entire range of atomic number and charge states studied. Fourth, the single

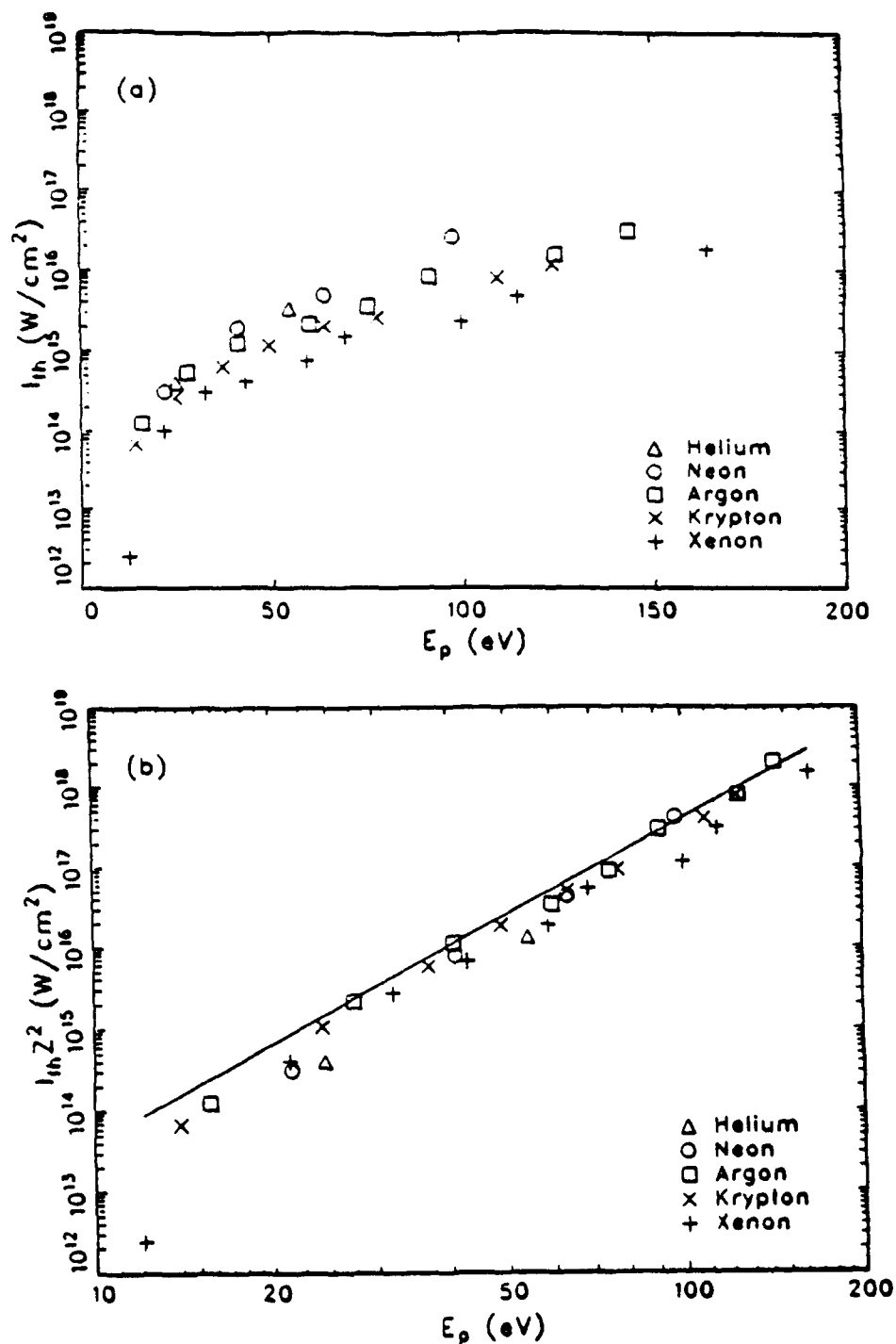


Fig. (4): (a) Threshold ionization intensities of the rare gases with subpicosecond 248-nm irradiation. (b) Same data replotted with Eq. (1) to show the scaling relationships. All intensities are peak values. [See Fig. (5) for the uncertainty in the intensities].

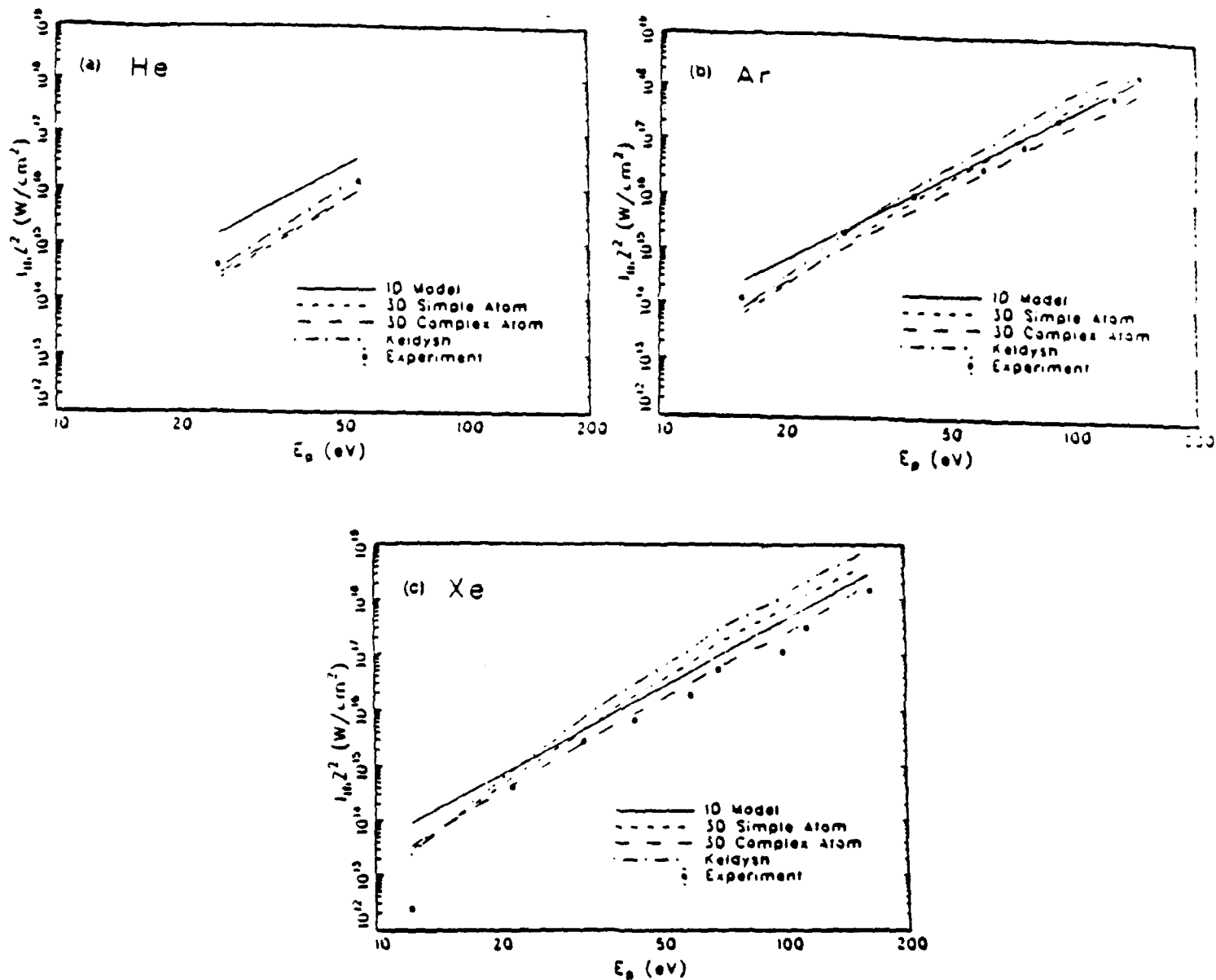


Figure 5: Threshold ionization intensities for (a) helium, (b) argon, and (c) xenon from Fig. (4) along with calculated results from various theories. The 1-D Model corresponds to Eq. (1), the 3-D Simple Atom to Eqs. (2) and (3), the 3-D Complex Atom corresponds to Eqs. (3) and (4). The Keldysh line was calculated from the equations in Ref. (19). All intensities are peak values. The relative uncertainty in the intensities is indicated by an error bar in the legend.

point which deviates considerably from all models is the threshold ionization of neutral xenon shown in Fig.(5c). However, this anomaly clearly arises from resonant multiphoton ionization, since there is a very close two-photon resonance ($5p \rightarrow 6p$) with 248-nm radiation.

The three tunneling models considered here are all quasi-static theories, equivalently, γ is vanishingly small. However, as mentioned above, the ultraviolet data all correspond to a regime in which γ is significantly greater than one. Although a full tunneling ionization model for a coulomb potential and an arbitrary γ has been solved,³⁶ the form of the solution is extraordinarily complicated. The consideration of a δ -function potential results in a considerably simpler expression for the ionization rate³⁶ and, from this model, the effect of a variation in γ on the threshold intensities has been estimated. The finding is that, up to a value of $\gamma \approx 3$, the threshold intensities decrease by less than a factor of two. Therefore, the dependence is not particularly strong, but the tendency is for a decrease in the threshold intensity.

The experimental measurement of threshold ionization intensities is a relatively simple procedure, but gives results which are rather insensitive to the actual ionization rates. Theoretical threshold values are correspondingly insensitive to the details of a given model on the same basis. It follows that it is difficult to use threshold data to evaluate the merits of various theories of ionization, unless very accurate measurements are made. On the other hand, the measurement of threshold intensities provides a practical and easy method of determining focused intensities to a reasonable accuracy.

Three main conclusions have emerged from studies of this nature on the production of atomic ions. First, even using 248-nm irradiation, threshold ionization intensities can be rather accurately described by a relatively elementary model of

tunneling ionization, at least for intensities $\gtrsim 10^{16}$ W/cm². Second, while a 1-D coulomb potential model qualitatively gives the basic scaling laws for tunneling ionization, a 3-D complex atom picture is required to give uniformly better quantitative agreement over the entire range of materials and charge states studied. Third, the measurement of threshold ionization intensities is rather insensitive to the details of the theoretical models and, therefore, has limited usefulness in testing alternative models of ionization. Finally, on the basis of the scaling revealed in these studies, we note that with the use of intensities in excess of 10^{18} W/cm², which are now achievable, it should be possible to remove completely the 4d shell from xenon producing krypton-like Xe¹⁸⁺. The total energy invested in ionization for this case would be ~ 3.5 keV. Species with this level of ionization are appropriate for the production of radiation in the soft x-ray range. Furthermore, considering that these ions can be kinetically cold, this is a rather unusual state of highly ionized matter.⁴²

2. Molecules

Studies of molecular ionization have produced additional insights into the dynamics of multiphoton processes.⁴³⁻⁵¹ Energetic coulomb explosions have been studied having kinetic energies of the fragments with several tens of eV per particle, evidence for molecular inner-shell excitation has been observed, and molecular atomic site-dependent energy deposition has been detected. Furthermore, these measurements have given rise to the hypothesis that appropriately designed molecules may enable the selective production of highly excited ionic fragments suitable for the generation of radiation in the x-ray range⁵². This possibility is discussed in Section III.A below.

a. Atomic Ion Production

Many interesting results have come from the study of a simple triatomic system (N_2O) whose structure is linear and asymmetric ($\text{C}_{\infty\text{v}}$). With irradiation at 248 nm at an intensity of $\sim 3 \times 10^{16} \text{ W/cm}^2$, both atomic and molecular (diatomic) ionic fragments are seen. Furthermore, since some of the studies⁵² have been performed with isotopic material ($^{14}\text{N}^{15}\text{N}^{16}\text{O}$), it has been possible to distinguish the original molecular sites of all the fragments observed in simple measurements of the ions.

The study of energetic atomic fragments from N_2O can reveal considerable information on the process of molecular multiphoton ionization. In particular, it is possible to measure the kinetic energies of the products arising from a molecular coulomb explosion with a suitably arranged time-of-flight apparatus.⁴⁷ As an example, we discuss below the results of recent measurements of atomic fragments produced in $^{14}\text{N}_2^{16}\text{O}$ conducted under conditions for which the fragment energy distributions have been determined.

Figure (6) illustrates the observed energy distribution for $^{14}\text{N}^{3+}$ produced from $^{14}\text{N}_2^{16}\text{O}$. Of course, this experiment does not distinguish between the two nonequivalent nitrogen positions and both nitrogen sites in the molecule contribute to the signal. Two aspects of the data are manifest, namely, the presence of significant structure in the distribution and the scale of the maximum energy observed. In consideration of the latter, the arrow in Fig. (6) represents a kinetic energy of $\sim 77.5 \text{ eV}$, the value which represents the endpoint of the observable signal. Interestingly, 77.5 eV is also the ionization potential⁵³ of ground state N^{3+} ions. This may be a coincidence, but a possible implication of these data is that a mechanism exists which effectively limits the kinetic energy of the fragment to its corresponding ionization potential. Molecular crossings to other state

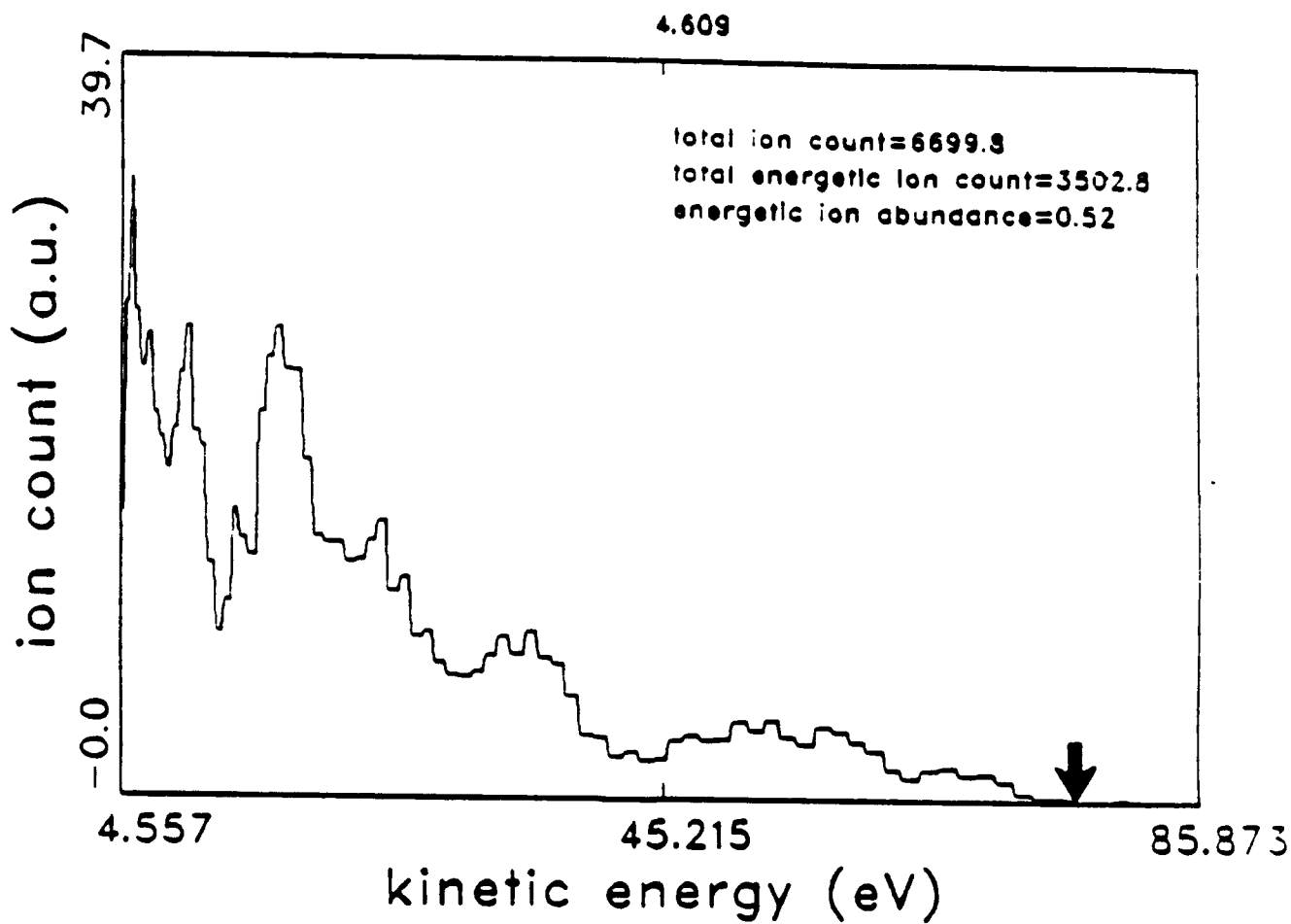


Fig. (6): The kinetic energy distribution of $^{14}\text{N}_2^+$ fragments observed in preliminary studies from $^{14}\text{N}_2^{16}\text{O}$ irradiated at 248 nm with ~ 600 fs pulses at a peak intensity of $\sim 3 \times 10^{16}$ W/cm 2 . The location of the arrow (*) corresponds to a kinetic energy for the fragment of ~ 77.5 eV, the value of the ionization potential of N^{2+} .

involving differently charged species, in this case the $N^{3+} + e^-$ channel, could provide the necessary mechanism. In this way, sufficiently energetic molecular dissociation may, through the action of a crossing, be directed into channels representing either electronic excitation or ionization. This process could be imagined as one involving electron promotion in a manner similar to that developed by Fano and Lichten⁵⁴ for the description of energetic ion-atom collisions. Basically, new channels including N^{3+} could be opening with the consequence that the N^{3+} yield is depressed. Related aspects of this type of interaction are considered in Section III.A.

The N^{3+} kinetic energy distributions, as measured from both N_2 and N_2O , are distinguished in another way, which may be related to this observation. From both N_2 and N_2O nitrogen ions with a charge as high as N^{5+} are detected.⁵⁵ Among these ions, however, the N^{3+} species clearly are clearly the most energetic. This aspect of the observed behavior remains to be understood.

A rough appraisal of the kinetics of molecular dissociation for the N^{3+} data shown in Fig. (6) is also informative. For this estimate we will assume that the dissociation occurs as a two-body event of the form



with the participation of a $(NO)^{q+}$ fragment. In the ground state⁵⁶, N_2O has equilibrium N-N and N-O spacings of 1.128 Å and 1.184 Å, respectively. If we assume that the effective location of the $(q+)$ charge on the NO fragment is located at its midpoint, then the N^{3+} ion is at a distance of $r_0 \sim 3.25 a_0$. The total coulomb energy release E_C is then given approximately by

$$E_c = \left(\frac{3q}{3.25} \right) \left(\frac{e^2}{a_0} \right). \quad (6)$$

The full kinetic energy E_k associated with the dissociation, given the equal magnitudes of the momenta for the two fragments, is

$$E_k = E_{N^{3+}} \left(1 + \frac{M_N}{M_{NO}} \right) = 1.47 E_{N^{3+}}, \quad (7)$$

in which $E_{N^{3+}}$ corresponds to the measured N^{3+} kinetic energy with M_N and M_{NO} representing the masses of the N^{3+} and $(NO)^q$ fragments, respectively. For $E_{N^{3+}} = 77.5$ eV, $E_k \approx 114$ eV. Equating $E_k \approx E_c$, we obtain $q \approx 4.6$, which we interpret as $q \approx 5$ for the NO^q fragment. Since the NO^q fragment involves two atoms, an effective value of $q \approx 5$ for the diatomic fragment does not appear unreasonable for conditions that would generate N^{3+} . Obviously, considerable further study will be necessary to fully ascertain the dynamics of these complex dissociations.

An important basic consideration relates to these molecular data. In the example examined in relation to Fig. (6), the nascent system produced is a species of the form $(N_2O)^{q_0}$ with a charge q_0 representing several electrons, perhaps, with a value of $q_0 \sim 8$ as estimated above. Moreover, this multiply charged system is produced by an interaction causing a negligible transfer of momentum to the molecule. Core state excitation followed by Auger decay can produce multiple ionization, but generally that process generates for this molecule only doubly ionized material^{57,58} with perhaps, a small fraction of triply ionized ions. Basically, the maximum level of ionization that can be attained by the Auger mechanism for molecules composed of atoms having relatively low atomic numbers is modest. Energetic heavy ion collisions^{59,60} can generate considerably higher levels of ionization, but this interaction generally imparts a very substantial recoil momentum

to the constituents of the molecular targets⁵². However, the combination of (1) a recoil-free interaction and a (2) high level of ionization can be quite simply achieved by the strong-field multiquantum mechanism. This method, therefore, enables the unique production of forms of kinetically cold highly excited matter⁴² that are essentially impossible to produce by other available methods⁵². Therefore, these results give evidence that entirely new forms of excited material can be generated by strong-field coupling. Further discussion of this important point is presented in Section III.C.2.

b. Molecular Site-Specific Energy Deposition

Previous experimental studies^{42,47,51} of N_2 and N_2O suggest that strong-field coupling may produce atomic site-selective energy deposition in molecules. Such a process would represent the multiphoton analogue of the site-specific excitation that can be achieved with the absorption of x-rays.⁶¹⁻⁶⁴ This could be observed, for example, with the nitrogen atoms in N_2O , a linear molecule with the structure NNO. The two nitrogen atoms sites in N_2O are nonequivalent; one resides on the end of the molecule while the other is located in the central position.

In preliminary experiments, the comparison of the fluorescence spectra exhibited by N_2 and N_2O in the 70-nm to 80-nm range, in relation to the behavior of certain N^{2+} lines involving $1s^2 2p^3$ doubly excited levels, has furnished specific evidence indicating this type of site-selective behavior. In order to verify this hypothesis, isotopic studies of ionic fragmentation have been performed to more fully examine these processes. For example, since $^{15}N^{14}NO$ and $^{14}N^{15}NO$ can be readily synthesized⁶⁵ from isotopically substituted NH_4NO_3 , the phenomenon of site-selective energy deposition can be sensitively and easily detected by comparative studies of ion production in $^{14}N^{14}NO$ and the isotopic variants. The same isotopic

material was also used to facilitate the measurements described below in Section II.B.2.c concerning the production of diatomic ionic fragments.

Initial experiments using $^{14}\text{N}^{15}\text{N}^{16}\text{O}$, have confirmed the expected site dependence from measurements of the charge state spectrum of the nitrogen ion fragments. A clear demonstration of this dependence is illustrated in Fig. (7). For the range of flight times involving the singly charged species N^+ and O^+ ($13 \leq M/q \leq 17$), normal ($^{14}\text{N}^{14}\text{N}^{16}\text{O}$) material produces the signal shown in Fig. (7a). In this case, it is impossible to distinguish the N^+ ions coming from the two different molecular sites.

In considering the data shown in Fig. (7), it should be understood that the shapes of the ion signals are determined by both the instrumental response and the kinetic energies of the fragments. The individual ion signals are actually composed of two components which are not fully resolved in these relatively low energy resolution data. One component arises from ions initially formed with velocities parallel to the time-of-flight direction while the other arises from ions whose initial velocity is anti-parallel to that vector. The two peaks are of unequal height and width due to the detailed nature of the trajectories which, in turn, are determined by the extraction and acceleration voltages used in the time-of-flight apparatus⁴⁷. Naturally, the total ion yield is given by the integral of the signal.

The same region of the time-of-flight spectrum is shown in Fig. (7b) for $^{14}\text{N}^{15}\text{N}^{16}\text{O}$. In this case, a small quantity of ^{40}Ar was present and the $^{40}\text{Ar}^{3+}$ signal is clearly seen. The argon peak can be used to calibrate the time-of-flight axis and give a direct measure of the instrumental width determined by the apparatus. In this regard, note the narrow and symmetric shape of the $^{40}\text{Ar}^{3+}$ signal.

Three distinct signals arising from the $^{14}\text{N}^{15}\text{N}^{16}\text{O}$ are clearly represented in Fig. (7b). Plainly, the total yield of the $^{15}\text{N}^+$ ions is approximately one half of

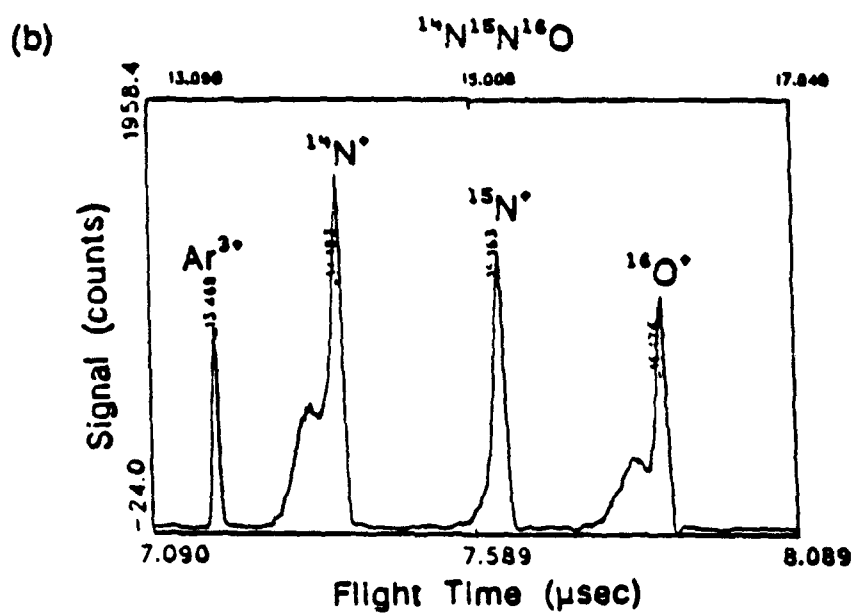
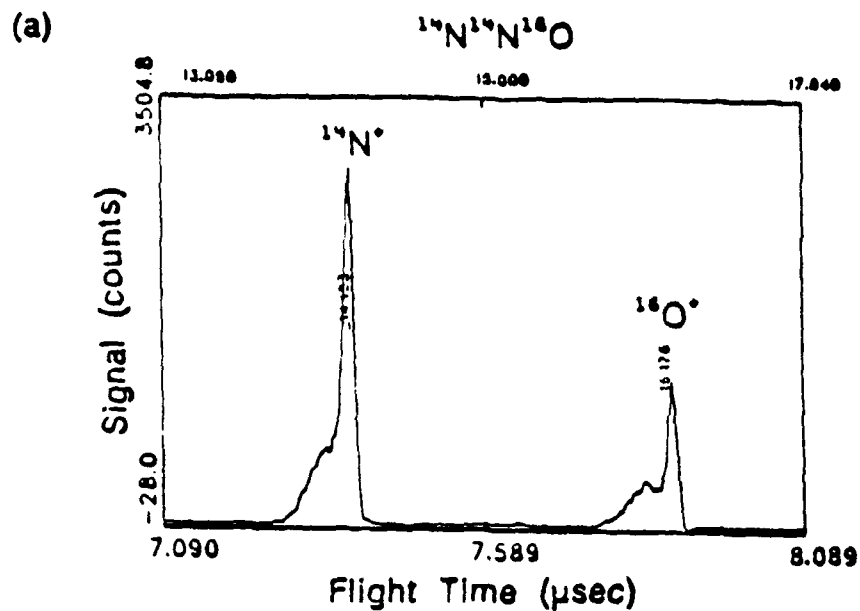


Fig. (7): Charge state fragments observed from N_2O in the range $13 \leq M/q \leq 17$
 (a) Spectrum from $^{14}\text{N}^{14}\text{N}^{16}\text{O}$. (b) Spectrum from $^{14}\text{N}^{15}\text{N}^{16}\text{O}$. See text for discussion.

the $^{14}\text{N}^+$ yield. Although several different detailed pathways can lead to the observed distribution, the outcome is that the total probability of producing singly charged ions depends upon the molecular site. We note that the widths of ^{15}N and ^{14}N signals, which indicate the range of kinetic energies of the fragments, are also quite different, with the former exhibiting a considerably narrower value. This conforms to the expectation that the atom in the center (^{15}N) would develop, in the process of fragmentation, a relatively smaller kinetic energy than the atoms on the ends of the molecule.^{50,66} Similar general characteristics, in regard to both the signal strengths and widths, are also seen in the N^{3+} channel in comparison of the $^{14}\text{N}^{3+}$ and $^{15}\text{N}^{3+}$ signals.

c. Diatomic Ion Yields

Informative behavior is also exhibited by the observation of diatomic fragments such as N_2^+ and NO^+ . The data on these ions for $^{14}\text{N}^{15}\text{N}^{16}\text{O}$ are shown in Fig. (8). In this case, the $^{15}\text{N}^{16}\text{O}^+$ yield appears to be slightly greater than the $^{14}\text{N}^{15}\text{N}^+$ yield. This result provides an interesting comparison with the yield ratio of these fragments formed by other known processes. For example, it is considerably different than that observed by photoionization^{67,68} of N_2O at 30.4 nm and also appears to differ from the ratio observed in other multiphoton studies,⁵⁰ conducted under somewhat different conditions of irradiation, at least for the $\text{N}_2\text{O}^{3+} \rightarrow \text{N}^+ + \text{NO}^+$ channel. However, the observed ratio is rather close to that seen⁶¹ when monochromatic soft x-rays (~ 405 eV) are used to excite N_2O . With a quantum energy of ~ 405 eV, the 2σ core electron on the central nitrogen atom is selectively excited to an empty 3π orbital, thereby initially concentrating the deposited energy at the molecular midpoint. A similar conclusion follows⁵⁷ when the $1s \rightarrow 2p^*$ orbital is excited on the O atom at ~ 536 eV. Interestingly, it is also known that Auger spectra in N_2O are sensitive to the site of excitation^{57,64}. Finally,

the comparison of the results in Fig. (7) with those obtained from electron scattering⁷⁰ is at present uncertain, since the latter reveal an unexpected difference in the NO^+/N_2^+ ratio in relation to the findings observed with soft x-ray excitation⁵⁷. Overall, the comparison on the basis of the fragment yield ratio of the multiphoton data with the results of other experiments on N_2O suggests that the experimental findings are consistent with a picture of the interaction involving a significant level of localization of the deposited energy in the NO region of the molecule. Considerable further work will be necessary to fully test this hypothesis.

The appreciable yield of NO^+ gives rise to a further interpretation⁷¹. The NO^+ system represents a triple bond⁷², whereas, initially in the N_2O system, the considerably stronger bond occurs between the two nitrogens. This implies the movement of a significant electron density along the axis of the molecule in the mechanism leading to the formation of the NO^+ fragment. Given the large number of molecular state crossings⁷² that are expected to exist at the level of excitation pertinent to such a transition, it seems unlikely that this flow of charge would occur adiabatically⁷¹ and channels leading to the production of excited states may be significant. The application of a sufficiently strong external field could be effective in generating such a motion. Considerable further analysis of these questions, particularly in light of known information on the photodissociation of highly excited molecules,^{72,73} is clearly necessary.

C. Radiation Studies

Over the past several years, many processes involving the production of radiation have been examined. These studies have involved measurements of fluorescence,^{51,74,75} harmonic generation in gases,^{74,76,77} parametric processes,⁷⁸ and x-ray generation from solid matter.⁷⁹⁻⁸⁵ In the sections following directly below, we discuss certain aspects of this area of research.

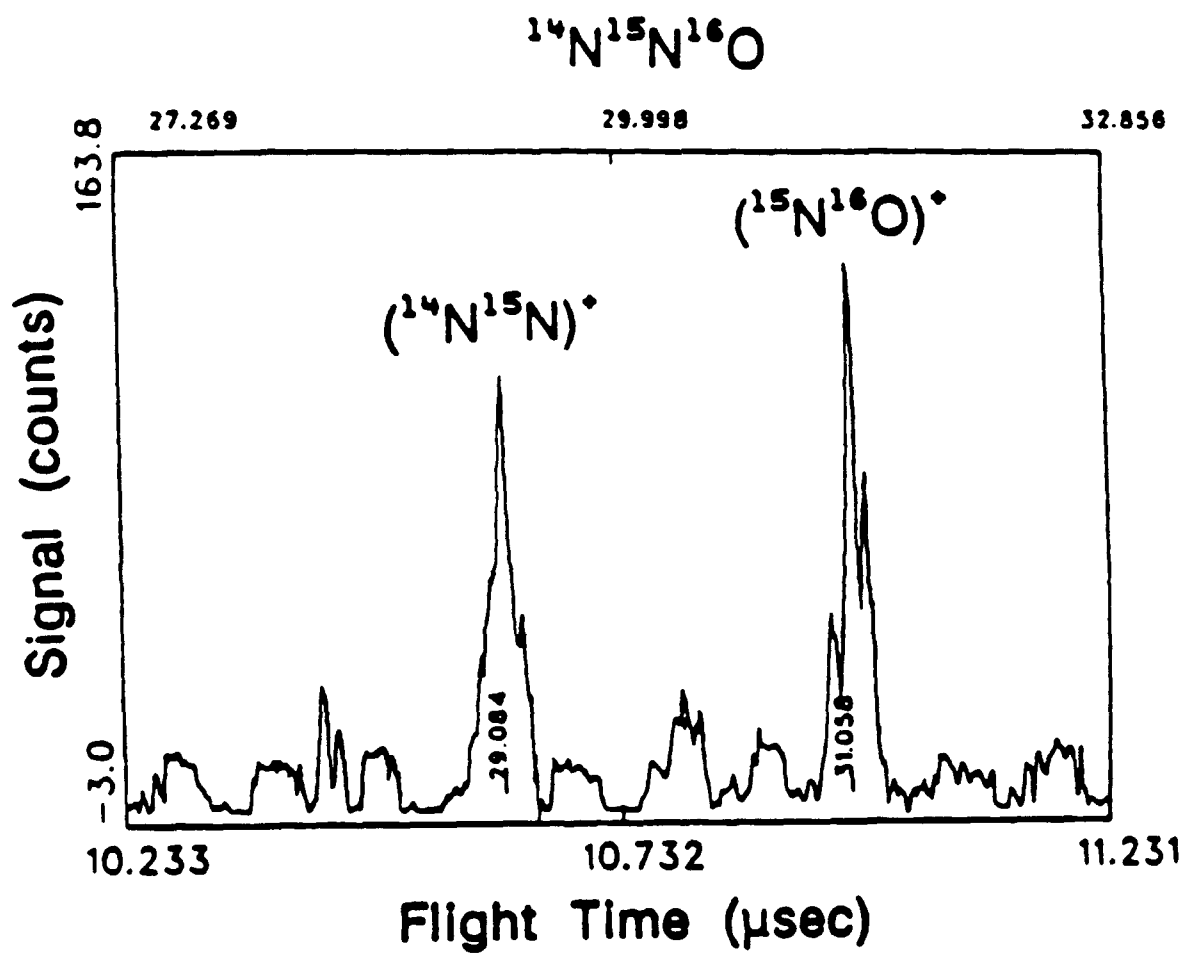


Fig. (8): Charge state spectrum of diatomic ions $(^{14}\text{N}^{15}\text{N})^+$ and $(^{15}\text{N}^{16}\text{O})^+$ observed from $^{14}\text{N}^{15}\text{N}^{16}\text{O}$. For discussion see text.

1. Fluorescence from Atomic Ions

The experimental arrangement used to conduct the studies of the radiation produced in gases is illustrated in Fig. (9). The source initially used for irradiation of the target gases was KrF* (248-nm) laser system⁷ that produced pulses having a maximum energy of ~ 20 mJ and a minimum pulse duration⁸⁶ of ~ 350 fs. A 23-cm (f/10) focal-length lens focused the 248-nm laser radiation into a gaseous target produced by a modified Lasertechnics pulsed gas jet. With this optical system, the intensity in the focal region was estimated to be in the range of $\sim 10^{15}$ – 10^{16} W/cm². Subsequently experiments utilizing the more powerful source illustrated in Fig. (1) enabled the achievement of focal intensities approximately one order of magnitude higher.

The gas jet was mounted 11.5 cm in front of the entrance slit of a 2.2-m grazing-incidence spectrometer (McPherson Model 247) equipped with a 600-line/mm gold-coated spherical grating blazed at 120 nm. A single-stage microchannel plate with a phosphored fiber-optic anode served as the detector. Mounting of the detector tangentially to the Rowland circle of the spectrometer allowed the observation of radiation between 7.5 and 80 nm. The FWHM resolution and accuracy of the spectrometer-detector system were typically ~ 0.1 nm. The pulsed-gas valve, which was modified to allow a backing pressure up to $\sim 5 \times 10^4$ Torr (1000 psi), was typically operated in the range of $\sim 10^4$ to $\sim 3 \times 10^4$ Torr with a pulse repetition rate of 2 Hz. Background pressures in various parts of the apparatus are indicated in Fig. (9). The laser was focused to a position a few hundred micrometers above the nozzle tip which had a diameter of 0.5 mm and a throat depth of 1 mm. The estimated gas density in the interaction region was $\sim 10^{18}$ cm⁻³.

In the studies employing the gas jet, fluorescence shorter than 10 nm from orbitally excited ions of Ar, Kr, and Xe has been observed. A region of the spectrum

Radiation Detection System

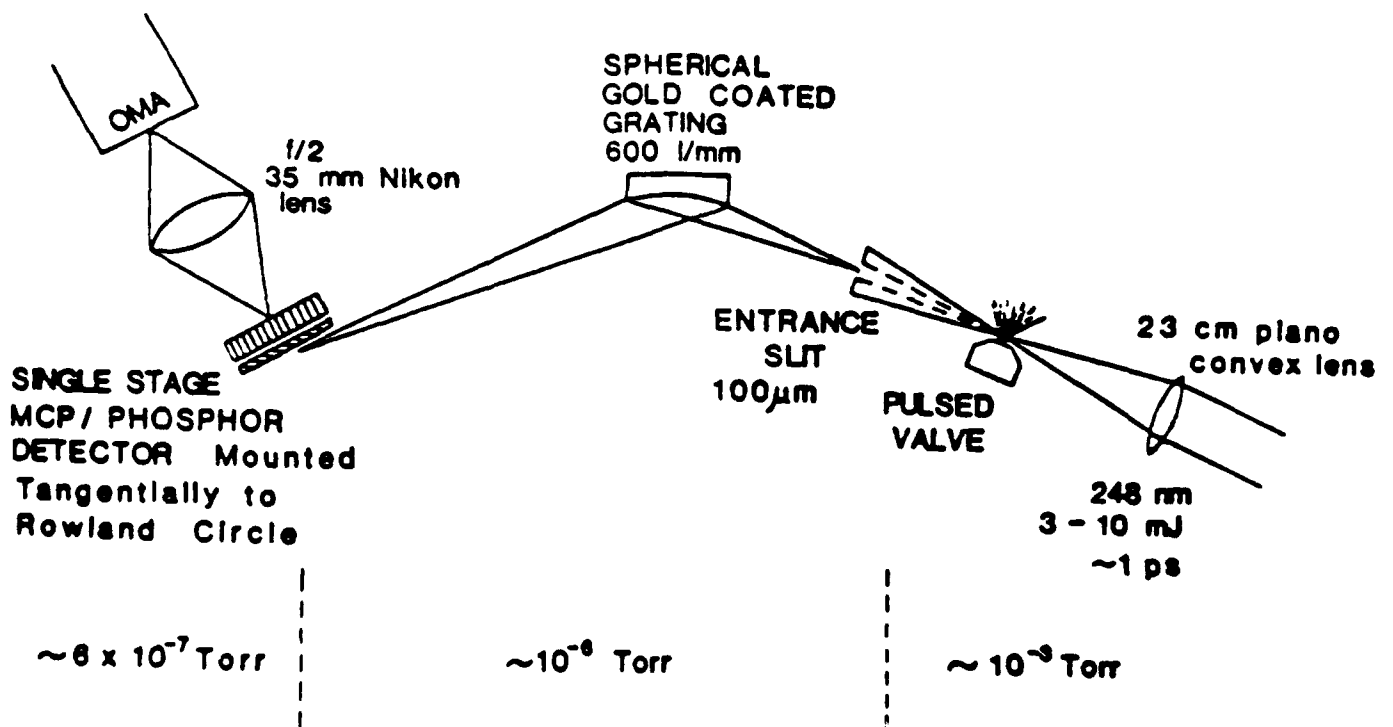


Fig. (9): Schematic of pulsed-gas jet and spectrometer-detector assembly used in studies of emitted radiation. Typical background pressures are indicated.

obtained for Kr is shown in Fig. (10), which illustrates two general features of these observed spectra. They are (1) identified radiation from high charge states and (2) an abundance of unidentified lines.

Table I summarizes the main properties of the observed fluorescence in Ar, Kr, and Xe. In all three materials a large number of emissions was seen. Although specific identification was often possible, as illustrated in Fig. (10) and Table I, a considerable fraction of the observed transitions could not be associated with the known spectra of any ionic species. It seems possible that multiply excited levels and/or core-excited states could account for some of these anomalous spectral features. At present, the information on the properties of such states, particularly for ionic spectra,¹⁰⁶⁻¹⁰⁷ is quite meager.

The large aperture KrF (248 mm) laser system⁹ shown in Fig. (1) has also been used for spectroscopic studies of gaseous targets. With this system, the intensity produced is somewhat greater than that used for the lines observed in Table I and radiation from the L-shell of argon originating from Ar^{3+} has been observed. The spectrum of argon shown in Fig. (11) clearly shows the presence of the well known⁵³ $2s2p^6 \rightarrow 2s^22p^5$ doublet along with the $4p \rightarrow 3s$ line of Ar^{7+} . It is also noted that the production of ground state Ar^{3+} from Ar^{8+} , by the removal of a 2p electron, requires a minimum of 422 eV and that the total energy investment needed to produce Ar^{3+} from the neutral atom exceeds a kilovolt. Analysis¹⁰⁸ of these data showed that the most consistent explanation is that the laser pulse creates a plasma, through a process not yet thoroughly understood, containing Ar^{7+} , Ar^{8+} , and Ar^{9+} with an effective electron temperature of ~ 20 eV. This temperature is sufficient to excite the Ar^{7+} states and the first excited state of Ar^{8+} , but no levels in Ar^{9+} . The conclusion¹⁰⁸ is that the lines observed in Ar^{7+} are fully consistent with a collisional-radiative model of the plasma with

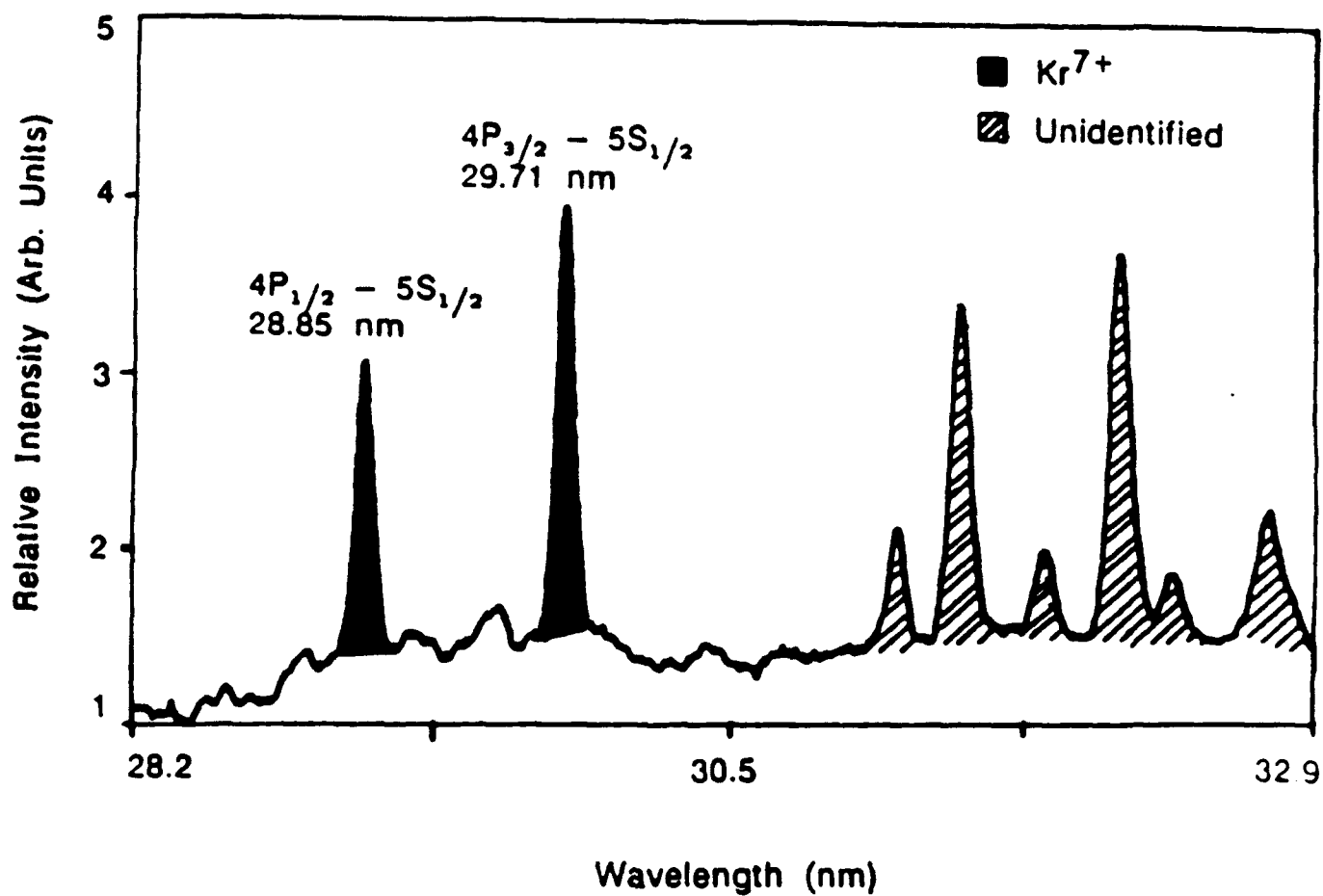


Fig. (10): A section of the Kr spectrum near 30 nm illustrates identified features from Kr^{7+} and unidentified lines of comparable strength.

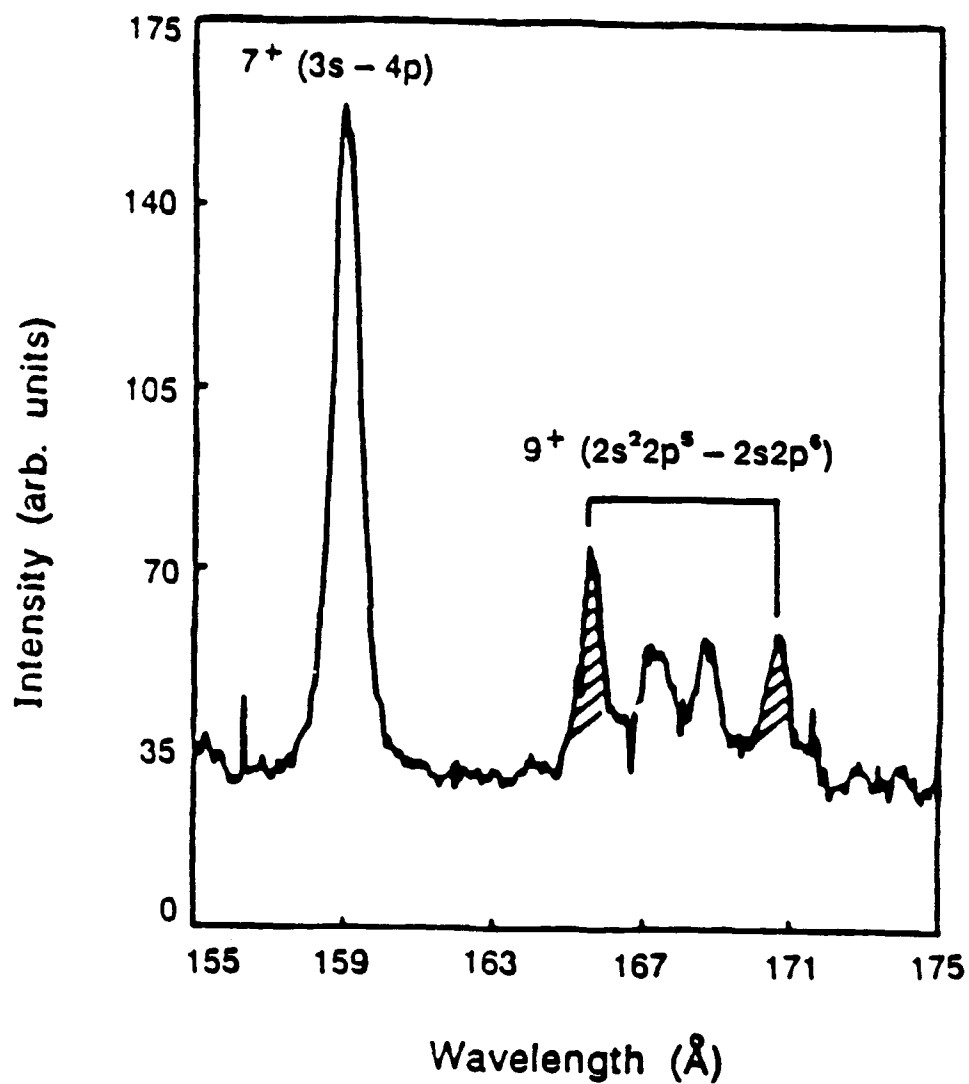


Fig. (11): Spectrum of Ar showing features from Ar^{7+} and Ar^{9+} observed in a gaseous target with a subpicosecond 248 nm pulse produced by the 10^2 cm^2 aperture laser system illustrated in Fig. (1).

Table I
Main Properties of the Fluorescence Observed
from Ar, Kr, and Xe with 248-nm Radiation at an
Intensity of $\sim 10^{15} - 10^{16}$ W/cm²

Material	Ar	Kr	Xe
Ionic charge states observed	4+, 5+, 6+, 7+	6+, 7+, 8+	6+, 7+, 8+
Wavelength range of emission (nm)	12.0-47.1	9.9-45.3	9.8-48.1
Typical identified transition	7+ 4f \longrightarrow 3d	7+ 5p \longrightarrow 4s	7+ <u>6s \longrightarrow 5p</u> 4d ⁹ 5s5p \longrightarrow 4d ¹⁰ 5s
Unidentified emissions	Many	Many	Many
References	53,85-88	53,89-95	96-103

an electron temperature of ~ 20 eV. However, in this picture the mechanism of formation of the Ar^{9+} ions is not explained, since independent ion production studies in the collision-free regime did not show production of Ar^{9+} under the same conditions of irradiation. It is conjectured that the third harmonic radiation at $83 \text{ nm}^{76,77}$ produced in the plasma may be playing a role in the appearance of the Ar^{9+} transitions. Therefore, although much has been accomplished to understand the properties of these rare gas plasmas, considerable work remains to be done in unraveling the details of the observed spectra, particularly in connection with radiation originating from the higher charge states.

2. Fluorescence from Ionic Molecules

Intense fluorescence from an intact molecular ion (N_2^{2+}) has been observed⁵¹ after irradiation of N_2 at an intensity of $\sim 10^{16} \text{ W/cm}^2$. The emission was strong and somewhat unexpected, since the probability for survival of intact molecular species might be presumed to be small under such conditions. Certain molecular systems, nevertheless, are detected in ion charge state spectra, as shown in Fig. (8). These findings are providing hints on the details of the complex nature of the molecular coupling to intense radiation.

The experimental results on fluorescence from N_2^{2+} indicate the excitation of inner electrons by a direct multiquantum process. The specific system illustrating this process is the production of $2\sigma_g$ holes in N_2 , the formation of which have been detected in two different kinds of experimental studies. The initial hint came from the measurement⁴⁷ of kinetic energy distributions of ionic fragments produced in N_2 with subpicosecond 248-nm radiation which indicated the presence of the charge asymmetric channel



resulting from multiphoton ionization. Interestingly, in experiments performed with subpicosecond 600-nm radiation, although some differences in the branching of the fragment charge distributions appear,^{46,47} additional evidence was also indicated¹⁰⁹ for reaction (8).

Since other experiments¹¹⁰ examining soft x-ray produced fragmentation of N_2 showed that process (8) corresponds to the production of a two-hole state having an excitation energy of ~ 70 eV, the obvious implication was that the laser excitation produced a similar configuration of molecular excitation. The states^{111,112} implicated in the x-ray studies¹¹⁰ of N_2 , which has the ground state configuration $(1\sigma_g)^2(1\sigma_u)^2-(2\sigma_g)^2(2\sigma_u)^2(1\pi_u)^4(3\sigma_g)^2$, were $^1\Sigma_g[2\sigma_g^{-1}, 3\sigma_g^{-1}]$, $^1\Sigma_u[2\sigma_g^{-1}, 2\sigma_u^{-1}]$, and $^1\Pi_u[2\sigma_g^{-1}, 1\pi_u^{-1}]$, all involving a $2\sigma_g$ hole. We note that the $2\sigma_g$ orbital has a binding energy of 37.7 eV, a value considerably higher than the $2\sigma_u$ (18.7eV), $1\pi_u$ (15.6 eV), and $3\sigma_g$ (16.7eV) orbitals. Therefore, the N_2^{2*} states having a $2\sigma_g$ vacancy and correlating to the $N^{2*} + N$ asymptote have an energy substantially above the lowest manifold of states¹¹³ in N_2^{2*} which are associated with the $N^* + N^*$ limit.

We describe below the observation of a very intense band of radiation at ~ 55.8 nm which appears to be fundamentally related to the mode of excitation producing the charge asymmetric fragmentation represented by process (8). These experiments were performed at an intensity of $\sim 10^{16}$ W/cm² with a pulse width of ~ 600 fs, conditions close to those pertaining to the ion studies reported in Section II.B.2.

The 55.8-nm emission was, at the outset, highly unusual in one obvious respect. Although the spectrum of N_2 has been studied for nearly a century¹¹² with many techniques of excitation, it was not possible to find any previous report^{53,112,114} of such a characteristic emission originating from material composed solely of nitrogen atoms or molecules in either neutral or ionic form. From this

fact alone, it appears that the observation of the 55.8-nm band originates from the excitation of a new class of states and that the strong production of these levels is intimately connected with the basic nature of the multiquantum mechanism involved in the coupling to the molecule. This line of reasoning and its implications in regard to the generation of x-rays and the comparison with collisional processes are explored below in Sections III.A and III.C, respectively.

The hypothesis that emerged from the analysis of the 55.8-nm radiation is that it originates from a quasi-bound $^3\Pi_U$ level of N_2^{2+} having a $(2\sigma_g^{-1}, 1\pi_U^{-1})$ configuration which undergoes a bound-bound transition terminating on the $D^3\Pi_g$ level associated with the $N^+ + N^+$ asymptote⁵¹. In addition, the previous studies of ionic fragmentation,⁴⁷ combined with the comparison of the results under comparable experimental conditions with N_2O , indicate that the $2\sigma_g$ vacancy is produced by a direct multiphoton process in N_2 leading to an excited state of the type $(N^{2+} + N)$, namely, a level with evident charge-transfer character. Therefore, the findings concerning the fluorescence are fully consistent with the results independently derived from the ion studies⁴⁷.

Overall, several transitions were assigned arising from the production of the $2\sigma_g$ vacancy. Qualitatively, the relative strengths of the molecular features could be accounted for by the overlap of the wavefunctions involved in the transitions. Basically, the transition producing the 55.8-nm radiation is



a case which has a very favorable overlap, a fact that can be seen directly by visualization of the wavefunctions of those two orbitals.^{115,116}

The spectrum in the region ~ 56 nm is shown in Fig. (12). Particularly significant from the standpoint of the identification is the measured width of the molecular feature, with respect to the widths of known N^+ lines, and the accompanying

presence of a vibrational progression ($v = 0, 1, 2$). The molecular energy level diagram derived from the analysis⁵¹ is illustrated in Fig. (13). Finally, Table II summarizes the assignments of the molecular features observed.

This spectroscopic evidence carries with it an important implication. Combined with the results stemming from the ion studies,⁴⁷ the indication is that the $2\sigma_g$ vacancy is produced by a direct multiphoton process in N_2 leading to an excited state of $(N^{2+} + N)$ character. Indeed, in referring to Table II, the presence of one transition (59.15 nm) implies that the $2\sigma_g$ electron can be removed without the additional loss of any valence electrons. For this to occur, the removal of the outer more weakly bound electrons must be sufficiently slow so that the interaction can communicate the energy needed to excite the $2\sigma_g$ orbital before the outer shells are ionized. Controversy has existed on this point for some years.^{26,43,117-119} There is, however, some more recent theoretical analysis indicating that such a suppression of the ionization rate may be able to occur at sufficiently high frequency.¹²⁰⁻¹²³

3. X-Ray Generation from Solid Targets

Solid materials offer the possibility of combining a high particle density with a very high level of electronic excitation, if the deposition of energy in the solid can be made to occur sufficiently rapidly. High brightness subpicosecond light sources of the type shown in Fig. (1) now enable such rapid excitation to be achieved. Given the fact that the studies of ionization described in Section II.B indicated total energy investments of ~ 1 keV per atom, at least for the heavier materials, the immediate suggestion is that a properly irradiated solid could serve as a powerful source of x-rays in the kilovolt region.

Consider a slab of unit area with density ρ and thickness δ which, upon excitation with intense subpicosecond radiation, produces radiation in the kilovolt

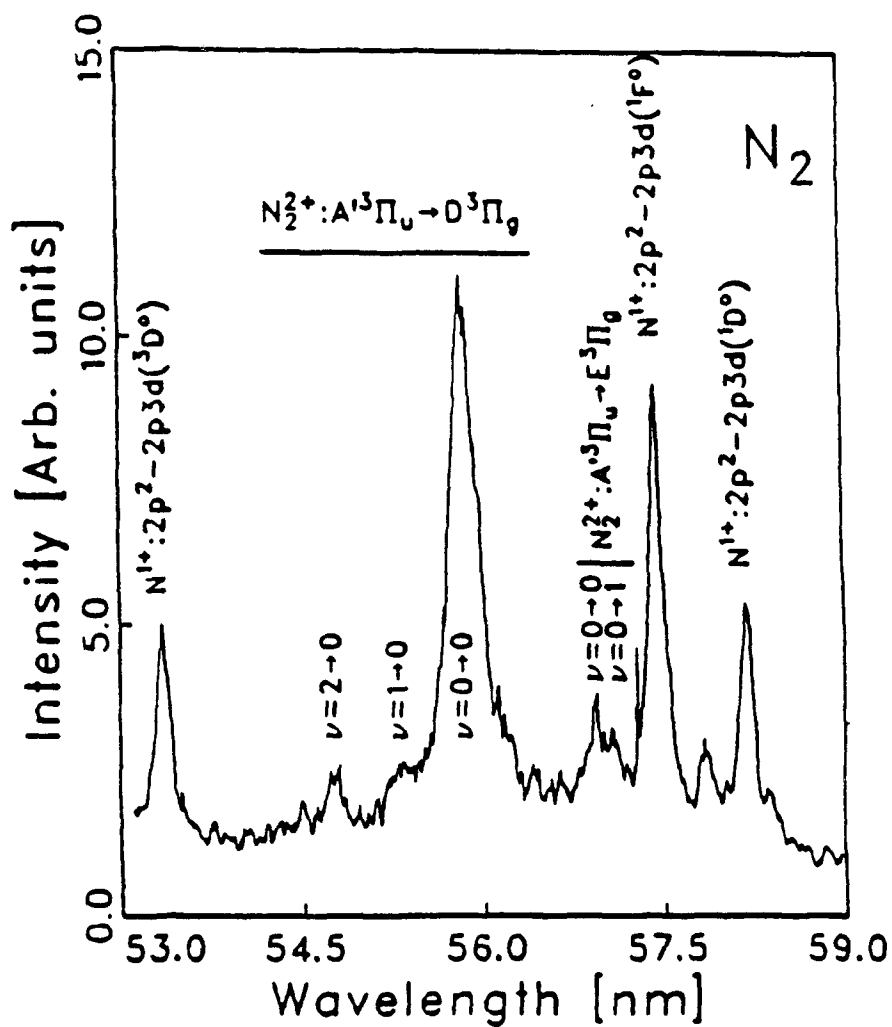


Fig. (12): The spectrum observed in N₂ in the 56-nm region produced with intense subpicosecond (~ 600 fs) 248-nm irradiation. Two groups of molecular features are identified, including the main transition at 55.8-nm, as well as several atomic lines. The density of N₂ used was ~ 10¹⁹ cm⁻³.

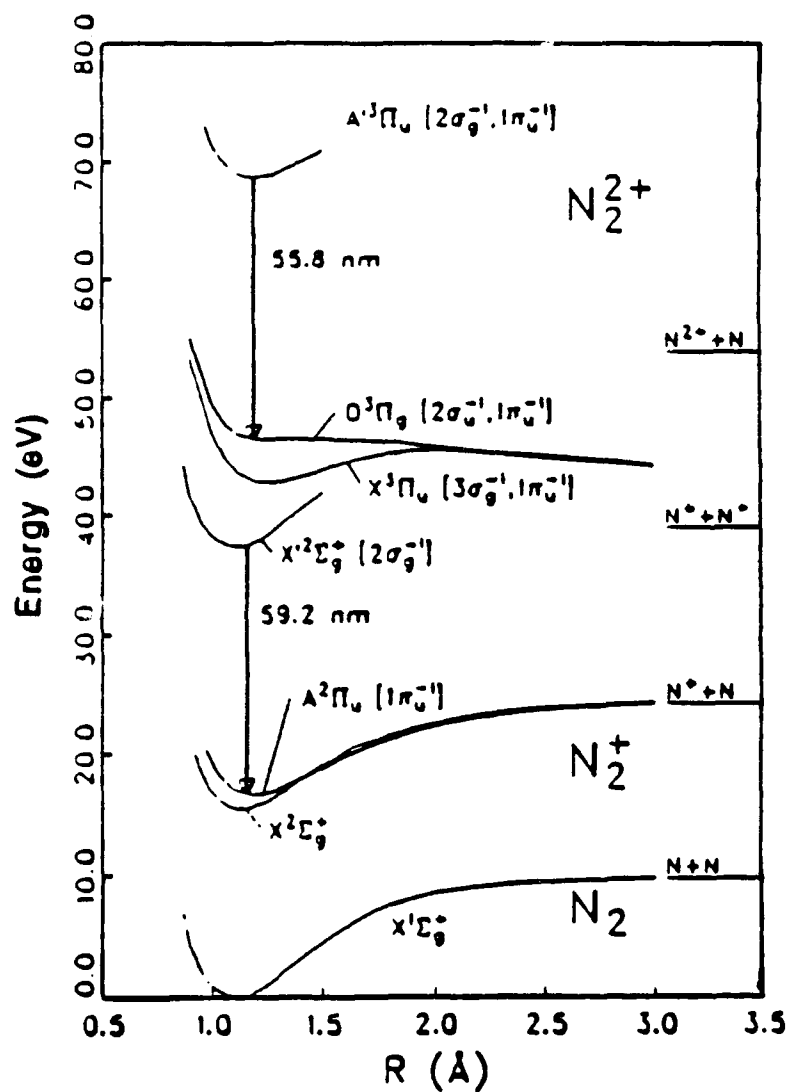


Fig. (13):

Potential energy curves for N_2 for selected states of interest. Two observed transitions involving a 2σ hole are indicated. Data for the curves were taken from a variety of sources (Refs. 109–111) as well as the author's own estimates. Dissociation limits are given for reference.

TABLE II

Assignment of Observed Transitions to
States of Molecular Nitrogen Ions

Observed Wavelength (nm)	Energy (eV)	Identification*	Vibrational* Levels ($\nu - \nu'$)	Electronic Configuration**
67.57	18.35	$N_2^{2+}: A' \ ^3\Pi_U \rightarrow G \ ^3\Pi_g$	0 - 1	$2\sigma_g^{-1} 1\pi_U^{-1} - 2\sigma_U^{-1} 1\pi_U^{-1}$
59.15	20.96	$N_2^{1+}: X' \ ^2\Sigma_g \rightarrow A \ ^2\Pi_U$	0 - 0	$2\sigma_g^{-1} - 1\pi_U^{-1}$
57.16	21.69	$N_2^{2+}: A' \ ^3\Pi_U \rightarrow E \ ^3\Pi_g$	0 - 1	$2\sigma_g^{-1} 1\pi_U^{-1} - 2\sigma_U^{-1} 1\pi_U^{-1}$
57.02	21.74	$N_2^{2+}: A' \ ^3\Pi_U \rightarrow E \ ^3\Pi_g$	0 - 0	$2\sigma_g^{-1} 1\pi_U^{-1} - 2\sigma_U^{-1} 1\pi_U^{-1}$
55.84	22.20	$N_2^{2+}: A' \ ^3\Pi_U \rightarrow D \ ^3\Pi_g$	0 - 0	$2\sigma_g^{-1} 1\pi_U^{-1} - 2\sigma_U^{-1} 1\pi_U^{-1}$
55.21	22.46	$N_2^{2+}: A' \ ^3\Pi_U \rightarrow D \ ^3\Pi_g$	1 - 0	$2\sigma_g^{-1} 1\pi_U^{-1} - 2\sigma_U^{-1} 1\pi_U^{-1}$
54.76	22.64	$N_2^{2+}: A' \ ^3\Pi_U \rightarrow D \ ^3\Pi_g$	2 - 0	$2\sigma_g^{-1} 1\pi_U^{-1} - 2\sigma_U^{-1} 1\pi_U^{-1}$
48.56	25.53	$N_2^{2+}: A' \ ^3\Pi_U \rightarrow A \ ^3\Sigma_g^-$	0 - 0	$2\sigma_g^{-1} 1\pi_U^{-1} - ***$

* Using calculations from Ref. (111) and authors' estimates

** Determined from Ref. (109)

*** Lower state not included in Ref. (109)

spectral range. In order to set the scale, we want to obtain a simple upper bound on the achievable x-ray intensity. Since the time of excitation is short, as a first approximation, we will ignore the hydrodynamical expansion, a process which will occur roughly at a rate of $\sim 1\text{--}10 \text{ \AA/fs}$. An upper limit on the x-ray intensity I_{xm} can then be simply written as

$$I_{xm} \sim \frac{\hbar\omega_x \rho \delta}{2\tau_x}, \quad (10)$$

in which $\hbar\omega_x$ represents a kilovolt quantum and τ_x is the effective radiative rate of the excited material. For the present discussion, we will set ρ as solid density ($\sim 1.7 \times 10^{22} \text{ cm}^{-3}$) and take as the lower limit for τ_x a typical radiative rate for kilovolt transitions. For the latter we will use the range $2 \times 10^{-14} \leq \tau_x \leq 10^{-13} \text{ s}$ as a rough measure.¹²⁴ If we take for δ the recently measured value⁸⁵ of the depth of energy penetration of $\sim 250\text{--}300 \text{ nm}$ for $\text{MgF}_2/\text{SiO}_2$ targets irradiated with 248 nm at an intensity of $\sim 3 \times 10^{16} \text{ W/cm}^2$, as described in Appendix A, Eq. (2) can be evaluated. With these parameters we find $3 \times 10^{14} \leq I_{xm} \leq 2 \times 10^{15} \text{ W/cm}^2$. This simple upper limit on I_{xm} can now be compared to the experimental result,¹²⁵ as described in Appendix B.

An experimental concern in studies of the interaction of intense radiation with solid matter is the influence of any low intensity prepulse on the true state of the irradiated system. As discussed in Appendix C, it has been experimentally found¹²⁶ that the interference of the prepulse can be entirely eliminated at 248 nm by the use of a target composed of ultraviolet transmitting materials. For example, MgF_2 , CaF_2 , and BaF_2 exhibit essentially no absorption up to relatively high intensities and studies have demonstrated that these values are sufficiently high to prevent any significant influence by the prepulse. This enables the intense subpicosecond

energy to couple directly to virgin solid matter.^{85,125,126}

The experimental configuration used for the measurement of the x-ray emission from solid BaF₂ targets is described fully in Appendix B. The spectrum observed from BaF₂ irradiated at a peak intensity of $\sim 0.3\text{--}1.0 \times 10^{17} \text{ W/cm}^2$ exhibited strong emission in the 9–13 Å range as shown in Fig. (14). The positions of three M-shell thresholds for Xe (Z = 54) are also indicated for reference. In addition to the spectrum, calibration of the film revealed that $\sim 2\text{--}4 \text{ mJ}$ of x-rays were produced on each shot. These measurements showed, assuming isotropic emission from the plasma, that the experimentally radiated intensity I_r was approximately $I_r \sim (0.5 \times 1.0) \times 10^{15} \text{ W/cm}^2$. We see immediately that this value falls in the range given by the estimate of the upper bound I_{xm} . The measured performance, therefore, appears very close to the maximum possible. Although such a source is incoherent, a radiation rate of this magnitude, coupled with the relatively narrow spectrum shown in Fig. (14), constitutes a source of extremely high spectral brightness that can produce unusually high excitation rates in absorbing material. We consider the case of xenon as an example, a material whose M-shell absorptions, as shown in Fig. (14), are very well matched to the measured BaF₂ spectrum.

Consider the response of xenon atoms located close to the x-ray source. The production rate ϕ_M of M-shell vacancies is given approximately by

$$\phi_M \sim \frac{I_r \sigma_M}{\hbar \omega_X} \quad (11)$$

in which σ_M ($\sim 2 \times 10^{-18} \text{ cm}^2$) denotes the absorption cross section¹²⁸ of xenon at $\sim 1 \text{ keV}$. From Eq. (11) we obtain $\phi_M \sim 10^{14} \text{ s}^{-1}$, a rate which is not far below the Auger decay rates of such M-shell vacancies. For example, an M₂

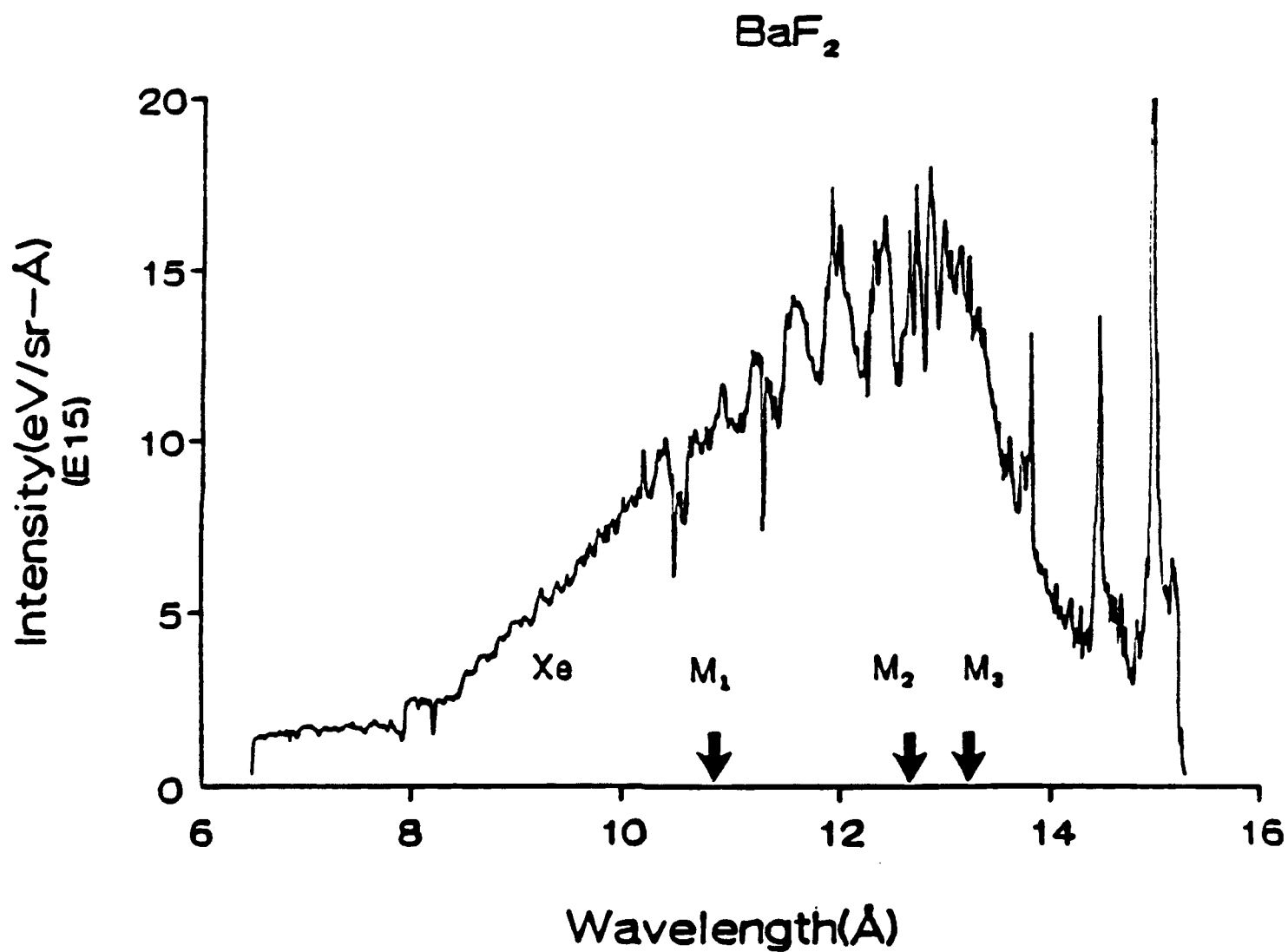


Fig. (14): Spectrum obtained from BaF_2 at an intensity of $\sim 0.3\text{--}1.0 \times 10^{17} \text{ W/cm}^2$. The positions of the M_1 , M_2 , and M_3 thresholds of Xe are indicated for reference. For details see the text and Appendix B.

vacancy has a theoretically estimated width^{129,130} in xenon of $\Gamma(M_2) \cong 4.83$ eV, a value which corresponds to a decay time $\tau \sim 0.4$ fs. The probability P_2 of producing a direct double vacancy is then on the order of

$$P_2 \sim (\phi_M \tau)^2 \sim 10^{-3} . \quad (12)$$

Since such double M-shell vacancy¹³¹ states would be expected to have Auger patterns significantly different from both single vacancies¹³² or double vacancies produced sequentially, a fraction of this magnitude ($\sim 10^{-3}$) may be sufficiently large for experimental detection. With very few exceptions, such shell-specific double-vacancy states constitute a virtually unexplored class of excited matter.¹³³⁻¹³⁷

III. DISCUSSION OF NEW POSSIBILITIES

The production of bright x-ray sources, as stated in the Introduction, is centered on the controlled and rapid production of x-ray emitters in an appropriate spatial volume. In this context three concepts are currently beginning evaluation. One involves the behavior of highly excited molecules, and is related to the discussions in Sections II.B.2, II.C.2, the second involves the studies of solids, as described in Section II.C.3, and the final topic concerns modes of electromagnetic propagation occurring in the strong-field regime. While not fully examined and speculative, on the basis of the experimental and theoretical results currently available, these topics clearly represent fertile and important new areas of active research.

A. Molecular Processes for X-Ray Generation

The results described in Sections II.B.2 and II.C.2 above lead directly to the formulation of a new principle of molecular design for x-ray emitting systems. The specific findings that lead to this conclusion are summarized in Table III.

The properties of the strong-field coupling compiled in Table III are fundamental to the production of coherent radiation of x-ray wavelengths primarily because

they enable the combination of (1) very highly excited forms of matter with (2) the characteristics of dense cold materials. This aspect of the coupling⁵² is considered further, particularly in comparison with collisional process,⁵² in Section III.B of Appendix D. Such circumstances are exceptionally conducive to the generation of amplification at x-ray wavelengths. It is the achievement of this conventionally paradoxical condition, which can be made to occur in the molecular frame, that permits the controlled generation of the very high rate of excited state production necessary for x-ray amplification. Moreover, since molecular systems are utilized, specific molecular designs can be created whose properties selectively govern the flow of energy into particular excited states. The resulting wavelength of emission will thereby be dependent upon the detailed structure of the molecular system.

These considerations are now illustrated within the framework of a particular example. Since we desire a high energy deposition *localized* on a particular atom, the results of the work described above indicate that this may be accomplished by placing a relatively heavy atom on a line between two lighter systems. We now assume that the axis defined in this way coincides with the polarization vector of the incident radiation. In order to take advantage of the anisotropy of the interaction^{44,46,47,50}, we now place two atoms, one on either side adjacent to the heavy atom on a line perpendicular to the original axis. In this form, the system has the shape of a cross. Since it is inconvenient to orient molecules, we now add two more atoms extending on either side of the central atom out of the plane of the cross. If, for simplicity, we let the six lighter systems be equivalent, the result is an octahedral molecule (O_h symmetry) with the heavy atom in the center.

TABLE III

Features of Strong-Field Multiquantum
Interaction Which Lead to Molecular X-Ray Emitter Design

Property of Interaction	References to Discussion
(1). Fields $\epsilon \gg e/a_0^2$ can be readily produced	(1). Ref. (9) and Ref. (10)
(2). Rapid energy transfer to molecule, $\Delta\tau \sim \lambda/c$, Δr small $\sim 0.1 \text{ \AA}$	(2). Ref. (47) and Ref. (51)
(3). Coupling exhibits strong anisotropy, mainly parallel to molecular axis	(3). Ref. (44), Ref. (46), and Ref. (50), and Ref. (107)
(4). Substantial e^- displacements Δx driven for $\epsilon \gg e/a_0^2$; $\Delta x \gtrsim r_0$	(4). Ref. (47) and Ref. (51)
(5). Inner molecular shells can be directly excited [e.g. $N_2(2\sigma_g)$].	(5). Ref. (51)
(6). Site selective molecular energy deposition (N_2O/N_2).	(6). Ref. (42) and Section II.B. 2.b above.

Specific examples would be SF_6 , MoF_6 , and UF_6 , all of which are convenient gas phase species at room temperature. A molecule with O_h symmetry, of course, will always present an axis involving the two lighter atoms with the central heavy atom which is favorably aligned with the polarization vector of the incident radiation.

We now consider, as a specific example, the behavior of a molecule (SF_6) as a result of intense irradiation in light of the considerations described above. In order to perform this analysis, we introduce a simplification that enables the system to be regarded as a diatomic molecule. Hence, we will assume that the central S atom interacts primarily with a single F atom. A slight breaking of the O_h symmetry occurring, for example, through vibrational excitation could be envisioned as the physical basis for this dynamical choice. Although we anticipate that the remaining F atoms will influence the molecular behavior, we expect that many of the important features of the dynamics will be revealed by the simpler diatomic picture.

Consider the SF diatom in the charge state SF^{17+} as a simple illustration. Due to the ability to produce site-selective energy deposition (point (6) in Table III), we will assume that the ionization is distributed as $S^{12+} - F^{6+}$. For ground state atoms, this gives the configurations $S^{12+}(1s^2 2s^2)$ and $F^{6+}(1s^2 2s^2)$, both of which give 1S_0 terms and, consequently, a single $^1\Sigma^+$ molecular state. Furthermore, since the energy transfer producing the ionization occurs very rapidly (point (2) in Table III, also see Section III.B in Appendix D), we take the initial internuclear separation of the SF^{17+} system as equivalent to the S-F internuclear distance occurring in the neutral parent SF_6 molecule. This distance is $r_0 \approx 1.56 \text{ \AA}$. The point (A) representing this situation can now be placed on the molecular energy level diagram shown in Fig. (15) along with the corresponding $^1\Sigma^+$ coulomb state. From this initial configuration, point (A), the system will begin to evolve along the $^1\Sigma^+$ curve. Furthermore, since essentially no momentum⁵² was communicated to atoms in the molecule during the strong-field multiquantum excitation, the dissociative motion along the $^1\Sigma^+$ curve begins with a vanishing velocity ($v \approx 0$). As the diatomic system dissociates, curve crossings will be encountered, such as the one labeled (B), shown arising from the $(S^{11+})^* + F^{6+}$ curve.

Several important aspects of the process are illustrated in the diagram of Fig. (15). They are (1) a crossing to the ground state $S^{11+} + F^{6+}$ configuration is not accessible, (2) the crossing leading to excited $(S^{11+})^*$ by electron transfer is reached, since $r'_0 > r_0$, (3) the velocity at point (B) can be very low, and (4) the dynamics of the crossing will be governed only by radial couplings.

The behavior at such crossings is well described in the Landau-Zener picture¹³⁸. The probability P of going through the crossing and remaining on the original curve is given by

$$P = \exp \left[- \left(\frac{\hbar}{2\pi v} \right) \left(\frac{|V_{12}|^2}{d/dR(E_1 - E_2)} \right) \right] \quad (13)$$

in which R is the internuclear coordinate, v is the velocity, V_{12} represents the matrix element for the radial coupling, and $E_1(R)$ and $E_2(R)$ denote the energies of the participating states. We note immediately that

$$\lim_{v \rightarrow 0} P = 0, \quad (14)$$

so that efficient crossing is expected to the $(S^{11'})^* + F^{**}$ curve, which generates highly excited $(S^{11'})^*$ ions, since v is small. Furthermore, such crossings confer substantial selectivity on the state $(S^{11'})^*$ produced through the properties of the radial matrix element V_{12} . For example, since the interaction is radial, no angular momentum is coupled to the electrons and crossings are only permitted to other curves of the same $(^1\Sigma^*)$ symmetry. This is a powerful selection rule⁵⁴ for the selective channeling of energy into a restricted set of excited quantum states. Experimental evidence has shown that such mechanisms can be quite effective in selectively generating excited states from both molecular¹³⁹ and quasi-molecular/collisional¹⁴⁰ systems. Finally, for the states shown in Fig. (15) representing the $(S^{11'})^*$ levels, the corresponding wavelength is $\lambda_x \approx 40 \text{ \AA}$ ($\sim 300 \text{ eV}$).

The most important aspect of Fig. (15) is the fact that the nature of the particle interactions is such that no single step enables a direct transition from the initially excited configuration to the ground state of the atomic system of interest $(S^{11'})$. Therefore, the dynamics of the excited material force the energy to flow in an orderly pathway that leads inevitably to the excited states of the system. For the free ion, the only available downward channel involves radiation. In summary, a dominant energy pathway in the mechanism of molecular relaxation of the excited system is established which contains a segment that can be traversed only by the emission of radiation. When this general circumstance is present,

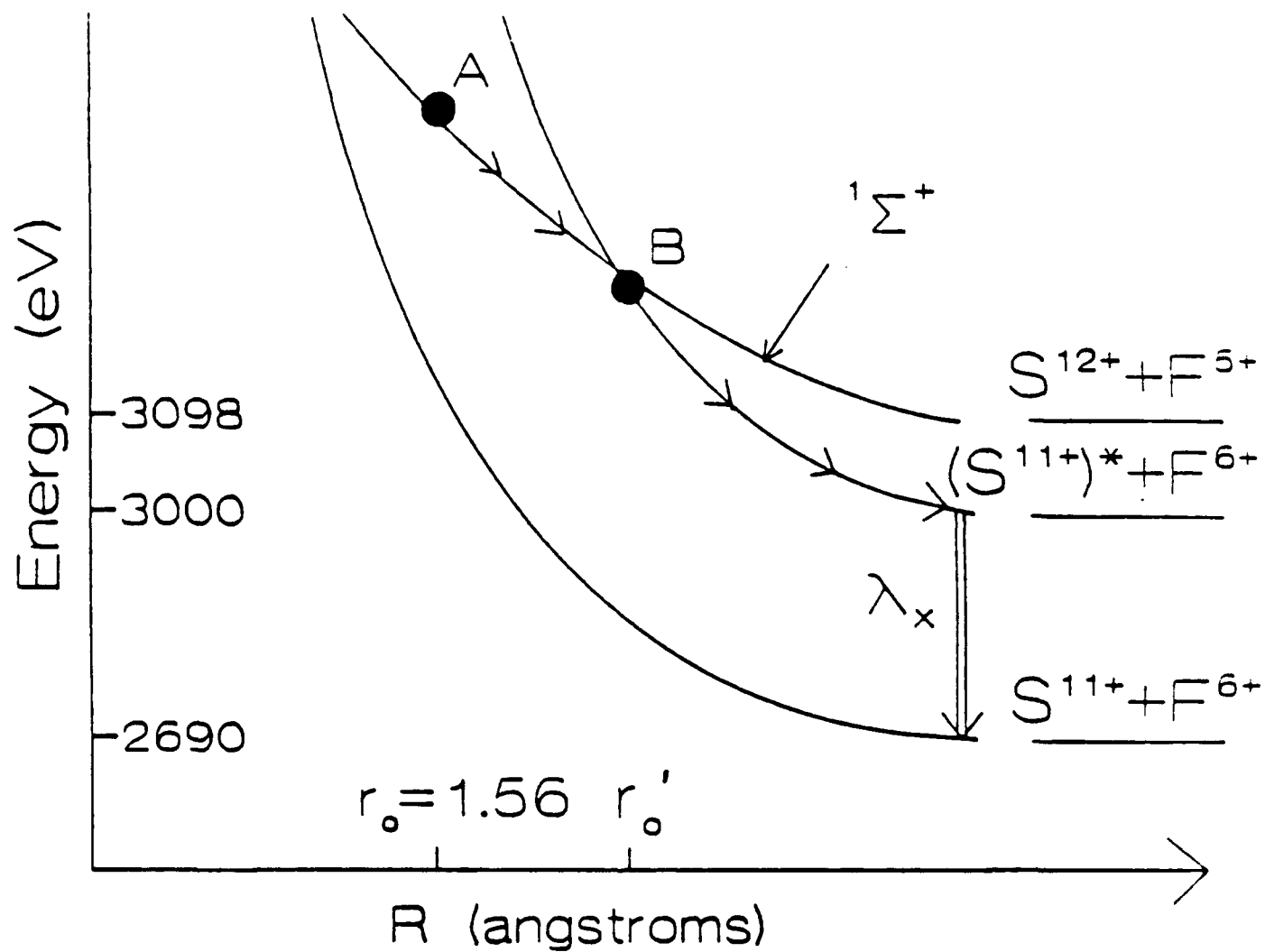


Fig. (15): Partial potential energy diagram of $S^{q_1\cdot} + F^{q_2\cdot}$ ($q_1 + q_2 = 17$) system. Note that the electron transfer crossing at r'_o is such that $r'_o > r_o$. For $S^{11\cdot}$, $\lambda_x \approx 40 \text{ \AA}$ ($\sim 300\text{eV}$). The ordinate is not drawn to a linear scale.

stimulated emission from the resulting highly nonequilibrium distribution of states can be readily generated. This situation is directly analogous to that occurring in excimer media¹⁴¹.

B. Hard X-Ray Generation from Solid Targets

As discussed in Section II.C.3 and Appendix B, very intense emission in the 9–13 Å range arising from M-shell transitions in Ba ions was observed from BaF₂. Indeed, the strength of the observed emission was so great that it was only slightly below an estimate of the upper bound possible. The model used to develop the estimate of the upper bound was both simple and extreme. Basically, it required that every atom in the radiating volume radiate a kilovolt quantum in the radiative lifetime of the Ba ion. This type of picture, obviously, represents an extraordinary level of excitation. In such circumstances, it is natural to inquire if excitation of deeper lying states might also be occurring, albeit, at a significantly lower rate.

For Ba, the next level of excitation would correspond to the L-shell, the edges¹²⁸ of which lie in the 5–6 keV region (~ 2 Å). In order to check for the presence of such radiation in this range, we equipped the spectrometer with a Si (111) crystal and examined the region ~ 2 Å experimentally. The spectrum produced in this preliminary study is shown in Fig. (16). The film shows a definite exposure in the region (shaded) ~ 2 Å. We note that the calibration of the wavelength may be uncertain as much as ~ 0.5 Å. The recorded strength of the exposure is ~ 1 –2% of the kilovolt (9–13 Å) spectrum shown in Fig. (14). Although the detected emission lies in the anticipated spectral region, the lineshape is not of the expected form and considerable further work needs to be done to clarify the origins and properties of this observed radiation. Obvious points of interest are the scaling relationships on intensity and atomic number (Z) governing the production of emission in the multi-kilovolt range.

C. General Consideration of Multiquantum Strong-Field Excitation

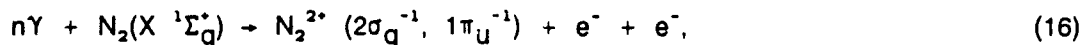
Two important conclusions concerning the character of strong-field multiquantum coupling stem from the discussion given in sections above. They involve (1) the ability to selectively excite inner electrons and (2) the general nature of the strong-field coupling to molecules.

1. Inner-Electron Excitation

As described in Section II.C.2, the observation of new band radiation at 55.8 nm from transitions involving inner-orbitals in N_2^+ and N_2^{2+} , produced by a direct multiphoton process involving N_2 in reactions of the form



and



provides strong evidence that deeply bound electrons, in this case $2\sigma_g$, can be directly excited^{117,119} by strong-field processes without extensive loss of more weakly bound outer valence electrons. It is expected that this feature of the interaction will manifest itself in many materials. Conventional pictures of multiphoton processes, particularly those involving the sequential emission of outer electrons from the system, do not provide a basis for understanding these results. Moreover, although N_2 has been one of the most common subjects of spectroscopic analysis for nearly a century, it is striking that the 55.8 nm band was one of the strongest features in the spectrum, but had never previously been observed. These facts suggest the presence of an important new feature in the mechanism of coupling. We now examine that aspect with the use of a simple approximate model of the interaction.

2. General Features of Strong-Field Coupling

In addition to providing specific data on N_2 and its ions, the information obtained from the studies of ion production⁴⁷ and fluorescence described above in Section II.C.2 leads to an important general hypothesis concerning the basic character

Shot #3 7-Feb-1991

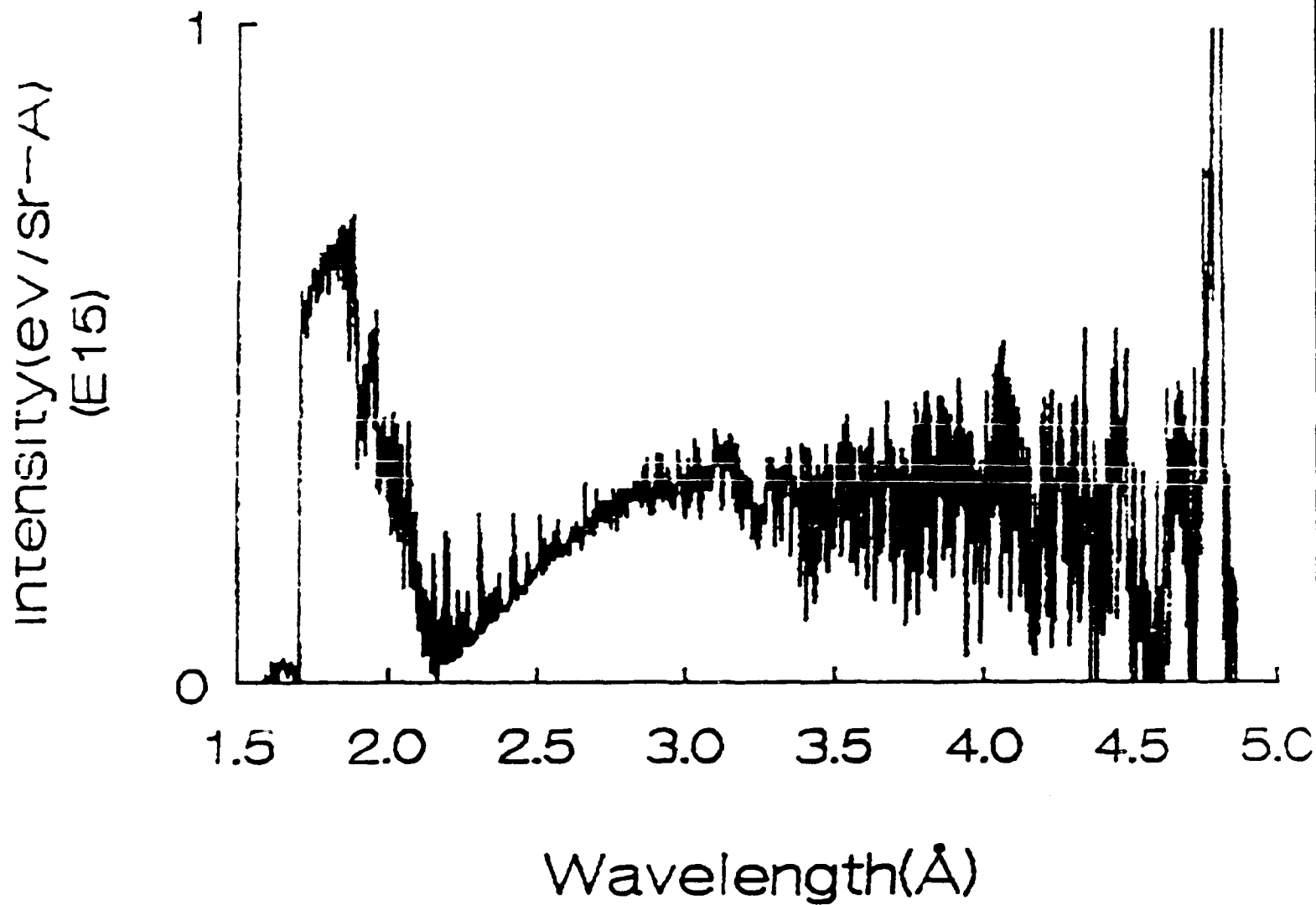


Fig. (16): Spectrum of BaF₂ in the region $\sim 2 \text{ \AA}$. The wavelength scale may be uncertain in the amount of $\sim 0.5 \text{ \AA}$. The visible exposure on the film corresponds to the shaded zone. The peak at $\sim 4.8 \text{ \AA}$ was caused by damage from the film holder.

of molecular multiphoton interactions in the strong-field ($E > e/a_0^2$) regime. Through comparison with electron and ion collisional processes, it will be shown that there is a large class of excitations which can be strongly excited only by strong-field coupling. Therefore, new states of excitation uniquely produced by the strong-field mode of interaction are generally expected for all molecular materials regardless of structure or composition. Furthermore, it will be seen that the excited states produced naturally by this form of interaction would commonly embody highly asymmetric charge distributions.

The comparison⁴² with charged-particle collisions can be accomplished in two ways, both of which express different aspects of the dynamics of coupling. One examines the pattern of the electric force developed during the collision while the other represents the encounter graphically in terms of variables describing (1) the maximum electric field ϵ_m produced and (2) the energy transfer E_t communicated to the molecular system during the collisional event.

We now describe a very simple approximate picture in order to present this comparison. Consider the ion-molecule (N_2) collisional process illustrated in Fig. (17a) involving an ion having charge Ze and velocity v colliding with impact parameter b . We assume that the ion follows a classical straight-line trajectory approximately perpendicular to the molecular axis. As the collision proceeds, the electric field from the ion experienced by the molecule varies appreciably in both magnitude and direction. Only at point B on the trajectory is the field aligned along the molecular axis. Otherwise the direction of the force on the molecular electrons deviates considerably from the molecular axis. The situation can be made more favorable for the excitation of electronic motions along the molecular axis by going to large impact parameter ($b \gg r_0$), but then the maximum collision field

$$\epsilon_m = \frac{Ze}{b^2} \quad (17)$$

is greatly reduced.

The electric field of a short-duration (τ_p) intense pulse of radiation polarized along the molecular axis represents a qualitatively different type of interaction. In this case, the resulting force field acts primarily to excite electronic motions along the molecular axis. For a sufficiently short pulse, nominally in the $\tau_p < 1$ ps range, the effect of molecular rotation for thermally excited levels at normal temperatures is negligible for almost all molecular materials. This can be seen by noting that molecular rotational frequencies ν_r are given approximately by $\nu_r \approx 2BJ$ for rotational constant B and angular momentum J . With the exception of the hydrides, if we take $B \sim 1 \text{ cm}^{-1}$ as a typical value, $\nu_r \tau_p \ll 1$ even for $J = 10$.

Further comparison is shown in Fig. (17b) for the case involving a parallel orientation of the ionic trajectory and the molecular axis. The main effect in this orientation is a force transverse to the molecular axis. Although the field can have an appreciable component along the molecular axis in the limit $b \rightarrow 0$, this situation has a vanishing probability of collision. In addition, as shown below, such close encounters with charged particles, particularly ions, differ from the strong-field coupling in another important way, since they generally impart a substantial recoil energy to the molecular system.¹⁴³ In sharp contrast, the strong-field coupling, although capable of exerting a force with a magnitude representative of ion collisions,¹⁴² is extremely ineffective in transferring kinetic energy directly to the target molecule or its constituent atoms.

The differences between the charged-particle collisional processes and the strong-field radiative interaction can be further understood by determining the relationship between kinetic energy transferred to the target system and the strength of the peak electric field occurring in the interaction. To find this relationship, these two processes can be parameterized by the peak field strength,

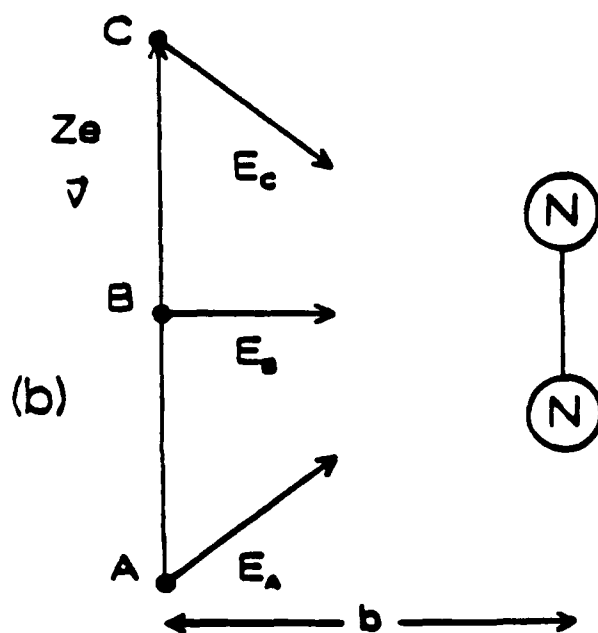
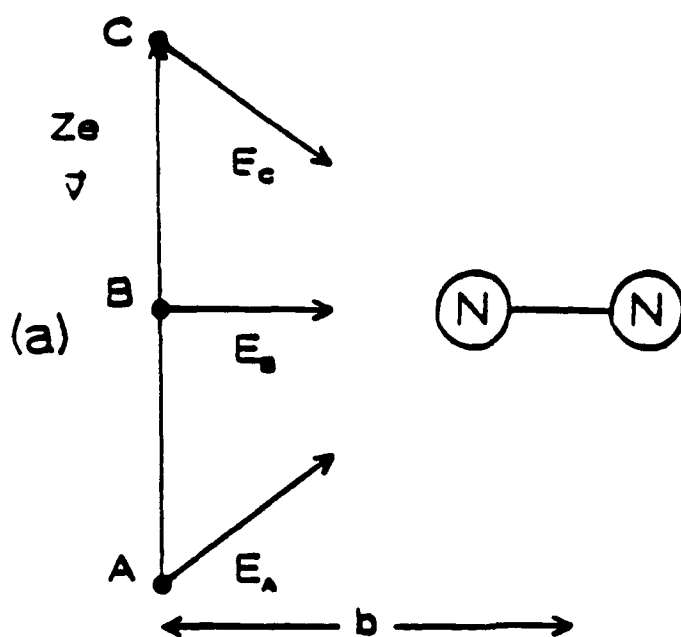
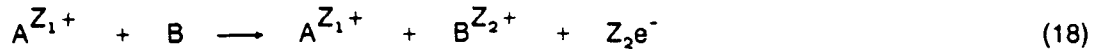


Fig. (17a): Geometry of ion-molecule (N_2) collisions showing the changing electric fields experienced by the target during the collisional event. (a) Ionic trajectory perpendicular to molecular axis; (b) ionic trajectory parallel to molecular axis.

ϵ_m , and the effective duration of the interaction, τ . For a given field strength, we set the interaction times equal for the two processes so that the comparison is made for a fixed transition probability. In the case of the strong-field process, the studies of ion fragmentation⁴⁷ indicated that the interaction time can be taken as approximately comparable to a period of the electromagnetic wave $\tau = \lambda/c$, while the corresponding field strength is given by $\epsilon_m = (4\pi I/c)^{1/2}$ in which I is the laser intensity.

For the charged particle collisions, we consider a process of the form



in which a projectile ion A of charge Z_1 collides with a neutral system B at rest producing a recoiling ion B^{Z_2+} with the collateral generation of Z_2 electrons. The recoil energy E_t of the target system B, for a projectile with energy E at impact parameter b , is given^{143,144} approximately by

$$E_t \approx \frac{Z_1^2 Z_2^2 e^2 M_A}{E M_B b^2} \quad (19)$$

with M_A and M_B representing the masses of the particles A and B, respectively, and e denoting the electronic charge. The time-scale of the collisional interaction will be given by

$$\tau = \left(\frac{b^2 M_A}{2E} \right)^{1/2} \quad (20)$$

The combination of Eqs. (17), (19), and (20) gives the desired relationship between E_t and ϵ_m , namely,

$$E_t = \frac{Z_2^2 e^2}{M_B} \tau^2 \epsilon_m^2 \quad (21)$$

Interestingly, the energy transfer E_t is independent of the nature of the charged projectile. The final connection between the strong-field interaction and the

charged-particle collision is obtained by setting the time scale of the collision equal to λ/c which yields

$$E_t = Z_2^2 f^2 \left(\frac{(e^2/a_0)^2}{M_B c^2} \right) \left(\frac{\lambda}{a_0} \right)^2 \quad (22)$$

where f is the maximum field strength in atomic units.

The validity of Eq. (22), for the simple collisional picture used, requires that

$$\frac{\Delta q}{M_A v_A} \ll 1 \quad (23)$$

where Δq is the momentum transfer occurring in the collision and v_A is the velocity of the projectile. Using Eqs. (17), (21), and (22), we find that

$$\frac{\Delta q}{M_A v_A} = \left(\frac{Z_2^2 f^2}{Z_1} \right)^{1/2} \left(\frac{\lambda^2}{a_0^2} \right) \left(\frac{e^2/a_0}{M_A c^2} \right) \quad (24)$$

If we take $Z_2^2/Z_1 \sim 1$ as a characteristic example, Eq. (23) is satisfied for $f \leq 30$. Actually, for field strengths larger than ~ 30 atomic units, the energy transfer will actually be greater than that given by Eq. (22). Thus, Eq. (22) represents a lower bound for charged-particle collisions. Furthermore, since the characteristics of the projectile do not appear in Eq. (22), this relationship is also valid for electron collisions.

We now examine the magnitude of other physical processes which can impart energy transfer to atomic or molecular systems. Generally, for the electron collisions, the emission of Auger electrons will impart a recoil energy exceeding that arising from the incident electron, the magnitude of which can be readily estimated from the kinematics of two-body decay. If we assume that an electron with mass m_e is emitted with an Auger energy E_a , then

$$E_t \approx E_a \left(\frac{m_e}{M_B} \right) \quad (25)$$

In order to estimate an upper bound, we will assume an energy scale for E_a on the order of the K-edge. In this case, for light materials in which the Auger

yields arising from a K-vacancy are high, a system such as Ne ($\hbar\omega_K \approx 870$ eV), gives $E_t \approx 24$ meV, a value almost exactly equal to the mean thermal energy at 300 K.

For heavy materials, such as uranium, since radiative yields dominate the decay of K-shell vacancies, the recoil developed is given approximately by

$$E_t \approx \frac{(\hbar\omega_K)^2}{2Mc^2} \quad (26)$$

where $\hbar\omega_K$ is the emitted photon energy. For U, Eq. (26) gives $E_t \approx 30$ meV, a magnitude close to that arising from Auger decay in light elements. L-shell Auger decay from U (~ 21 keV) gives $E_t \approx 46$ meV, so it is also in the same range. Less energetic excitations arising from electron scattering will, of course, produce smaller recoil energies. Overall, for a wide range of scattering conditions and materials, the recoil energies induced by electron scattering will fall in the range $\sim 3 \times 10^{-5} \leq E_t \leq 5 \times 10^{-2}$ eV.

The recoil energy imparted to an ion during multiphoton ionization is naturally expected to be small, since the incident photons carry very little momentum. For a given number N of quanta absorbed with energy $\hbar\omega$, the recoil is expressed as

$$E_t \approx \frac{(N\hbar\omega)^2}{2Mc^2} \quad (27)$$

the multiquantum counterpart of Eq. (26). From the previous discussion, for a total energy such that $N\hbar\omega = \hbar\omega_K$, E_t is less than 30 meV for all materials.

Two additional mechanisms can communicate recoil energy to the ion produced by multiphoton ionization. They are (1) the interaction of the field-driven ionized electron with the ion, a process equivalent to inverse-bremsstrahlung in the field of the ion, and (2) the subsequent emission of Auger electrons similar to that discussed above in relation to electron collisions. Since the latter can be associated

with essentially the same bounds as the electron scattering case, we now consider the former.

During the inverse-bremsstrahlung process a photon ($\hbar\omega$) is absorbed with the resulting energy appearing in the kinetic energy of the electron-ion pair. Assuming the ion to be structureless, this is a form of elastic electron scattering for which the resulting recoil can be approximately estimated from Eq. (19) provided that it is possible to determine appropriate values for the electron energy E and the impact parameter b . In terms of the particle energy, we can associate the average energy of driven motion with the ponderomotive potential. For radiation at 248 nm, an intensity of 10^{16} W/cm² gives an equivalent ponderomotive potential of 57 eV.

Measurements⁴⁷ of ion energy distributions for N_2^{2+} ions give an upper bound on $E_t \approx 60$ meV and, therefore, a lower limit on the effective value of b . For N_2^{2+} irradiated at 248 nm for ~ 600 ps at an intensity of $\sim 10^{16}$ W/cm², with $Z_1 = 1$, $Z_2 = 2$, $E \approx 57$ eV, and $M_A = m_e$, Eq. (19) gives $b \geq 0.1 a_0$. This value of the impact parameter is expected to be a considerable underestimate, since the experimental bound on E_t was instrumentally limited.⁴⁷ We now scale, for a fixed value of this impact parameter, to fully ionized uranium ($Z_2 = 92$) and let $I \approx 10^{21}$ W/cm² ($\epsilon_m \approx 170$), a procedure which gives $E_t < 1$ meV. Even accounting for multiple electron emission, most of which occurs for rather low values of Z_2 , it is unlikely that the recoil will be above the experimental bound established for N_2^{2+} , namely, within a factor of two of the thermal energy for $T = 300$ K. This places an upper bound on the kinetic energy transfer associated with the strong-field coupling to be on the order of those arising in the case of electron scattering.

We observe that any ion will also experience a ponderomotive potential in the high intensity wave. For a proton irradiated with 248 nm radiation at an intensity of 10^{21} W/cm², the ponderomotive potential is ~ 3.1 keV. This energy, however, is fully returned^{145,146} to the radiation field during the course of the

pulse so that no net displacement of any molecular ions, regardless of charge or mass, will occur as a result of the ponderomotive potential.

This analysis leads to the following general conclusions. Ion collisions can present strong forces ($\epsilon_m \gg 1$) and large recoil energies while electron collisions generate relatively weak forces ($\epsilon_m \leq 1$) and correspondingly small recoil effects. Furthermore, both of these scattering processes are ineffective in exciting organized electronic motions along specific molecular axes. In comparison, since the short-pulse strong-field excitation (1) can generate a high force strength ($\epsilon_m \gg 1$), (2) communicates a recoil energy which is very small in relation to molecular bond strengths, and (3) readily excites electronic motions along specific molecular directions, it represents a unique domain of interaction.

These respective regions of interaction can be conveniently displayed in the $\epsilon_m - E_t$ plane shown in Fig. (18). In this picture, the strong-field multiquantum coupling ($\epsilon_m \geq 1$) clearly represents a distinct regime of interaction that is totally unachievable with charged particle collisions and permits strong electronic forces to be applied to a system whose molecular frame can remain intact. It is this situation, in combination with the dynamical features illustrated in Fig. (17), that enables the strong-field coupling to efficiently produce new modes of excitation in molecular materials. The region corresponding to the experiments on N_2 , as shown in Fig. (18), clearly falls in this new zone. It is this feature of the interaction which can account for the otherwise anomalous appearance of the $2\sigma_g$ vacancies and the 55.8 nm emission described in Section II.C.2. Although N_2 has served as a specific example, such processes are expected to occur generally for all materials regardless of structure or composition. Given the nature of this form of excitation, it is particularly well suited for the direct generation of states involving a very large charge asymmetry, such as that represented in N_2 by Eq. (8).

D. Strong-Field Propagation

A fundamentally new regime of electromagnetic propagation is expected to arise in plasmas for subpicosecond radiation at a sufficiently high intensity¹⁴²⁻¹⁵³. Among the important new phenomena that may occur is a mode of channeled propagation, a key process for the generation of coherent radiation in the x-ray region.¹⁴⁹ When a very intense pulse of radiation enters a cold medium, multiphoton ionization locally produces a plasma, and the following qualitative behavior involving a relativistic/charge-displacement mechanism can develop. The conversion of electrons from bound to free states by the ionization induces a strong reduction in the refractive response of the atomic material. The resulting plasma exhibits a further decrease in index from the free-electron component collaterally produced. If the ambient electron density n_0 is such that the plasma frequency $\omega_p = \sqrt{4\pi n_0 e^2/m}$ is below the frequency of the radiation ω , an interesting mode of channeled propagation could develop. Indeed, calculations indicate that the presence of both relativistic motion and charge-displacement can lead to stable self-focusing, as discussed in Appendix E.

The influence of the charge-displacement can be seen in the following way. For a sufficiently short pulse (~ 100 fs), the ions remain spatially fixed while the relatively mobile electrons are expelled by the ponderomotive potential from the central high-intensity region of the beam. A state of equilibrium can then be established between the ponderomotive and the electrostatic force densities owing to the net charge displacement. Since the electrons, which embody a negative contribution to the index, are expelled, an on-axis region of relatively high refractive index is formed which can support channeling of the laser beam.

Preliminary analysis concerning the channeling indicates (1) that the Compton intensity ($\sim 4.5 \times 10^{19}$ W/cm² at $\lambda = 248$ -nm) establishes the scale for the prominence of this phenomenon and (2) that the frequency scaling strongly favors the use of the shortest wavelength available at high power¹⁴⁹. A channel radius of several

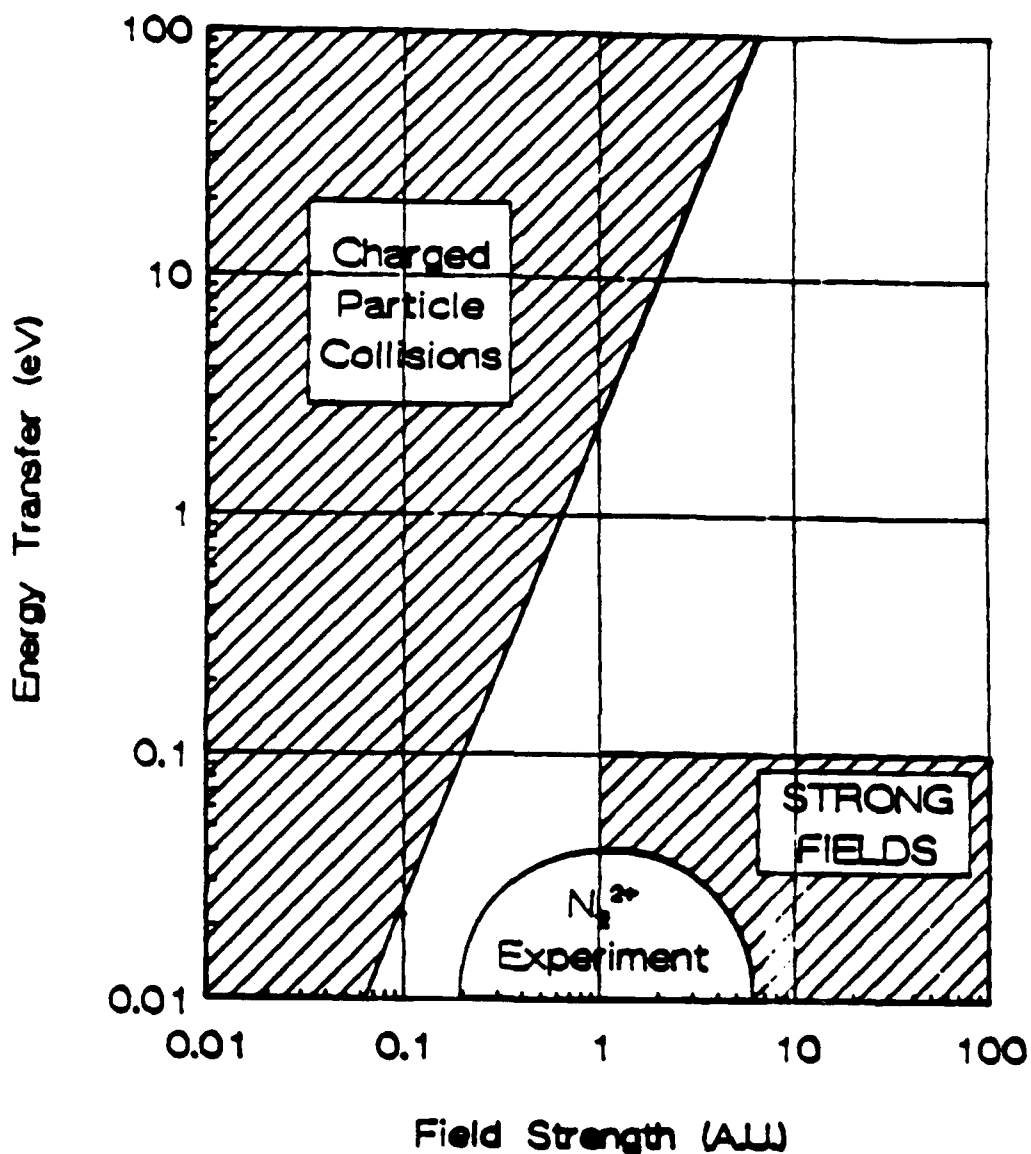


Fig. (18): Display of the comparison of the energy transfer versus electric field strength for charged particle collisions and strong-field interactions, including the influence of Auger events and Inverse-bremsstrahlung. Clearly, strong-field interactions lie in a region totally inaccessible by the collisional processes. The region of the N_2 experiments discussed in the text is shown. The parameters for the ion boundary stemming from Eq. (22) correspond to $\lambda = 248$ nm and the other data conforming to the N_2^{2+} case.

wavelengths also emerges from this analysis. Moreover, recent dynamical calculations¹⁵⁹ support the conclusion that such modes of propagation can be formed under stable conditions. A description of the stability that arises from the interplay of relativistic and charge-displacement mechanisms is given in Appendix E. The ability to stably propagate high intensity radiation in this manner would be a fundamental advance in the control and concentration of power in materials, the key question relevant to the production of amplification in the x-ray range. Furthermore, it facilitates the spatial control necessary to produce a high brightness output.

Recent experiments have led to the observation of this mode of propagation, as described in Appendix F. A comprehensive theoretical treatment is given in Appendix G. The importance of these results on the scaling of x-ray amplifiers is profound. This influence is described in Appendix H.

IV. SUMMARY AND CONCLUSIONS

The use of recently developed high brightness subpicosecond light sources for the study of the interaction of matter with strong electromagnetic fields is leading to the observation of new phenomena associated with new classes of excited states of matter and new modes of electromagnetic propagation. One important consequence of these findings is the generation of powerful x-ray sources associated with properly controlled plasma environments.

This report has discussed several aspects related to the general question of the controlled deposition of energy at high power levels in materials, the central issue in the development of bright x-ray sources. The common factor linking the various topic is the ability to produce extremely high levels of electronic excitation in a manner which enables the system to remain kinetically cold for the time scale of the interaction. For the situations considered, this time interval is generally less than a picosecond. It is the mastery and control of this class of physical processes that will inevitably lead to a new generation of extremely bright sources in the x-ray range.

V. REFERENCES

1. A. V. Vinogradov and I. I. Sobel'man, "The Problem of Laser Radiation Sources in the Far Ultraviolet and X-Ray Regions," *Sov. Phys. - JETP* **36**, 1115 (1973).
2. C. K. Rhodes, "Multiphoton Ionization of Atoms," *Science* **229**, 1345 (1985).
3. S. Szatmári, F. P. Schäfer, E. Müller-Horsche, and W. Mückenheim, "Hybrid Dye-Excimer Laser System for the Generation of 80 fs, 900 GW Pulses at 248 nm," *Opt. Comm.* **63**, 305 (1987).
4. A. Endoh, M. Watanabe, N. Sarukura, and S. Watanabe, "Multiterawatt Subpicosecond KrF Laser," *Opt. Lett.* **7**, 353 (1989).
5. J. R. M. Barr, N. J. Overall, C. J. Hooker, I. N. Ross, M. J. Shaw, W. T. Toner, "High Energy Amplification of Picosecond Pulses at 248 nm," *Opt. Comm.* **66**, 127 (1988).
6. J. G. Glowina, J. Misevich, and P. P. Sorokin, "160-fsec XeCl Excimer Amplifier System," *J. Opt. Soc. Am.* **B4**, 1061 (1987).
7. A. P. Schwarzenbach, T. S. Luk, I. A. McIntyre, U. Johann, A. McPherson, K. Boyer, and C. K. Rhodes, "Supicosecond KrF* Excimer-Laser Source," *Opt. Lett.* **11**, 499 (1986).
8. J. P. Roberts, A. I. Taylor, P. H. Y. Lee, and R. B. Gibson, "High-Irradiance 248-nm Laser System," *Opt. Lett.* **13**, 734 (1988).
9. T. S. Luk, A. McPherson, G. Gibson, K. Boyer, and C. K. Rhodes, "Ultrahigh-Intensity KrF* Laser System," *Opt. Lett.* **14**, 1113 (1989).
10. A. J. Taylor, C. R. Tallman, J. P. Roberts, C. S. Lester, T. R. Gosnell, P. H. Lee, and G. A. Kyrala, *Opt. Lett.* **15**, 39 (1990); A. J. Taylor, T. R. Gosnell, and J. P. Roberts, "Ultrashort-Pulse Energy-Extraction Measurements in XeCl Amplifiers," *Opt. Lett.* **15**, 118 (1990).
11. I. A. McIntyre, and C. K. Rhodes, "High Power Ultrafast Excimer Lasers," *J. Appl. Phys.*, to be published.
12. T. S. Luk, private communication.
13. B. Bouma, private communication.
14. H. Schulz, H. Schüler, T. Engers, and D. von der Linde, "Measurement of Intense Ultraviolet Subpicosecond Pulses Using Degenerate Four-Wave Mixing," *IEEE J. Quantum Electron.* **25**, 2580 (1990).
15. A. L'Huillier, L.-A. Lompré, G. Mainfray, and C. Manus, "Multiply Charged Ions Formed by Multiphoton Absorption Processes in the Continuum," *Phys. Rev. Lett.* **48**, 1814 (1982).
16. A. L'Huillier, L.-A. Lompré, G. Mainfray, and C. Manus, "Multiply Charged Ions Induced by Multiphoton Absorption in Rare Gases at 0.53 μm ," *Phys. Rev. A* **27**, 2503 (1983).

17. T. S. Luk, H. Pummer, K. Boyer, M. Shahidi, H. Egger, and C. K. Rhodes, "Anomalous Collision-Free Multiple Ionization of Atoms with Intense Picosecond Ultraviolet Radiation," *Phys. Rev. Lett.* 51, 110 (1983).
18. T. S. Luk, U. Johann, H. Egger, H. Pummer, and C. K. Rhodes, "Collision-Free Multiple Photon Ionization of Atoms and Molecules at 193 nm," *Phys. Rev. A* 32, 214 (1985).
19. M. D. Perry, O. L. Landen, A. Szöke, and E. M. Campbell, "Multiphoton Ionization of the Noble Gases by an Intense 10^{14} W/cm² Dye Laser," *Phys. Rev. A* 37, 747 (1988).
20. F. Yergeau, S. L. Chin, and P. Lavigne, "Multiple Ionization of Rare-Gas Atoms by an Intense CO₂ Laser (10^{14} W/cm²)," *J. Phys. B* 20, 723 (1987).
21. S. Augst, D. Strickland, D. D. Meyerhofer, S. L. Chin, and J. H. Eberly, "Tunneling Ionization of Noble Gases in a High-Intensity Laser Field," *Phys. Rev. Lett.* 63, 2212 (1989).
22. G. Gibson, T. S. Luk, and C. K. Rhodes, "Tunneling Ionization in the Multiphoton Regime," *Phys. Rev. A* 41, 5049 (1990).
23. O. L. Landen, M. D. Perry, and E. M. Campbell, "Resonant Multiphoton Ionization of Krypton by Intense UV Laser Radiation," *Phys. Rev. Lett.* 59, 2558 (1987).
24. P. Agostini, F. Fabre, G. Mainfray, G. Petite, and N. K. Rohman, "Free-Free Transitions Following Six-Photon Ionization of Xenon Atoms," *Phys. Rev. Lett.* 42, 1127 (1979).
25. P. Kruit, J. Kimman, and M. J. van der Wiel, "Absorption of Additional Photons in the Multiphoton Ionization Continuum of Xenon at 1064, 532 and 440 nm," *J. Phys. B* 14, L597 (1981).
26. U. Johann, T. S. Luk, H. Egger, and C. K. Rhodes, "Rare-Gas Electron-Energy Spectra Produced by Collision-Free Multiquantum Processes," *Phys. Rev. A* 34, 1084 (1986).
27. A. G. Muller and A. Tip, "Multiphoton Ionization in Strong Fields," *Phys. Rev. A* 30, 3039 (1984).
28. R. R. Freeman, P. H. Bucksbaum, H. Milchberg, S. Darack, D. Schumacher, and M. E. Geusic, "Above-Threshold Ionization with Subpicosecond Laser Pulses," *Phys. Rev. Lett.* 59, 1092 (1987).
29. P. Agostini, P. Breger, A. L'Huillier, H. G. Muller, G. Petite, A. Antonetti, and A. Migus, "Giant Stark Shifts in Multiphoton Ionization," *Phys. Rev. Lett.* 63, 2208 (1989).
30. T. S. Luk, T. Graber, H. Jara, U. Johann, K. Boyer, and C. K. Rhodes, "Subpicosecond Ultraviolet Multiphoton Electron Spectroscopy of Rare Gases," *J. Opt. Soc. Am. B* 4, 847 (1987).
31. L. V. Keldysh, "Ionization in the Field of a Strong Electromagnetic Wave," *Sov. Phys. JETP* 20, 1307 (1965).

32. R. M. Potvliege and Robin Shakeshaft, "Time-Independent Theory of Multiphoton Ionization of an Atom by an Intense Field," *Phys. Rev. A* **38**, 4597 (1988).
33. H. Reiss, "Effect of an Intense Electromagnetic Field on a Weakly Bound System," *Phys. Rev. A* **22**, 1786 (1980).
34. L. D. Landau and E. M. Lifshitz, Quantum Mechanics, 3rd. Ed., (Pergamon Press, London, 1978).
35. B. M. Smirnov and M. I. Chibisov, "The Breaking Up of Atomic Particles by An Electric Field and by Electron Collisions," *Sov. Phys. JETP* **22**, 585 (1966).
36. A. M. Perelomov, V. S. Popov, and M. V. Terent'ev, "Ionization of Atoms in an Alternating Electric Field," *Sov. Phys. JETP* **23**, 924 (1966).
37. M. V. Ammosov, N. B. Delone, and V. P. Krainov, "Tunnel Ionization of Complex Atoms and of Atomic Ions in an Alternating Electromagnetic Field," *Sov. Phys. JETP* **64**, 1191 (1986).
38. U. Johann, T. S. Luk, I. A. McIntyre, A. McPherson, A. P. Schwarzenbach, K. Boyer, and C. K. Rhodes, in Proceedings of the Topical Meeting on Short Wavelength Coherent Radiation, J. Bokor and D. Attwood, eds., AIP Conference Proceedings No. 147, (AIP, New York, 1986), p.202.
39. N. H. Burnett and P. B. Corkum, "Cold-Plasma Production for Recombination Extreme-Ultraviolet Lasers by Optical-Field-Induced Ionization," *J. Opt. Soc. Am. B* **6**, 1195 (1989).
40. I. S. Gradshteyn and I. M. Ryzhik, Tables of Integrals, Series, and Products, (Academic Press, New York, 1965).
41. H. R. Reiss, "Complete Keldysh Theory and Its Limiting Cases," *Phys. Rev. A* **42**, 1476 (1990).
42. "Ion Production and Molecular Excitation Occurring in Multiphoton Processes," A. McPherson, T. S. Luk, G. Gibson, K. Boyer and C. K. Rhodes, *Nuclear Instruments and Methods in Physics Research, Section B43*, (North-Holland Physics Publishing Division, 1989) p. 468.
43. J. Frasinski, K. Codling, P. Hatherly, J. Barr, I. N. Ross, and W. T. Toner, "Femtosecond Dynamics of Multielectron Dissociative Ionization by Use of Picosecond Laser," *Phys. Rev. Lett.* **58**, 2424 (1987).
44. K. Codling, L. J. Frasinski, P. Hatherly, and J. R. M. Barr, "On the Major Mode of Multiphoton Multiple Ionization," *J. Phys. B* **20**, L525 (1987).
45. T. S. Luk and C. K. Rhodes, "Multiphoton Dissociative Ionization of Molecular Deuterium," *Phys. Rev. A* **38**, 6180 (1988).
46. K. Codling, L. J. Frasinski, and P. A. Hatherly, "On the Field Ionization of Diatomic Molecules in Intense Laser Fields," *J. Phys. B* **22**, L321 (1989).
47. K. Boyer, T. S. Luk, J. C. Solem, and C. K. Rhodes, "Kinetic Energy Distributions of Ionic Fragments Produced by Subpicosecond Multiphoton Ionization of N_2 ," *Phys. Rev. A* **39**, 1186 (1989).

48. P. A. Hatherly, L. J. Frasinski, K. Codling, A. J. Langley, and W. Shaikh, "The Angular Distribution of Atomic Ions Following the Multiphoton Ionization of Carbon Monoxide," *J. Phys. B* 23, L291 (1990).
49. P. H. Bucksbaum, A. Zavriyev, H. G. Muller, and D. W. Schumacher, "Softening of the H_2^+ Molecular Bond in Intense Laser Fields," *Phys. Rev. Lett.* 64, 1883 (1990).
50. L. J. Frasinski, K. Codling, and P. A. Hatherly, "Covariance Mapping: A Correlation Method Applied to Multiphoton Multiple Ionization," *Science* 246, 1029 (1989).
51. G. Gibson, T. S. Luk, A. McPherson, K. Boyer, and C. K. Rhodes, "Observation of a New Inner-Orbital Molecular Transition at 55.8 nm in N_2^{2+} Produced by Multiphoton Coupling," *Phys. Rev. A* 40, 2378 (1989).
52. T. S. Luk, A. McPherson, G. N. Gibson, K. Boyer, and C. K. Rhodes, "Molecular X-Ray Laser Research," to be published in the Proceedings of SWLA - 90 International Symposium, "Short Wavelength Lasers and Their Applications," Samarcand, USSR, May 14-18, 1990.
53. R. L. Kelly, "Atomic and Ionic Spectrum Lines below 2000 Angstroms: Hydrogen through Krypton," Part I, *J. Phys. Chem. Ref. Data* 16, Suppl. No. 1 (1987).
54. U. Fano and W. Lichten, "Interaction of Ar^+ -Ar Collision at 50 KeV," *Phys. Rev. Lett.* 14, 627 (1965).
55. T. S. Luk, A. McPherson, K. Boyer, and C. K. Rhodes, "Studies of the Interaction of Molecules and Solids with Intense Subpicosecond 248 nm Radiation," Proceedings of the ICOMP V Conference, Paris, September 1990, to be published.
56. G. Herzberg, Molecular Spectra and Molecular Structure, III, Electronic Spectra and Electronic Structure of Polyatomic Molecules (D. Van Nostrand Co., Inc., New York, 1966).
57. J. Murakami, M. C. Nelson, S. L. Anderson, and D. M. Hanson, "Fragmentation of Nitrous Oxide by Monochromatic Soft X-Rays," *J. Chem. Phys.* 85, 5755 (1986).
58. R. Murphy and W. Eberhardt, "Site Specific Fragmentation in Molecules: Auger-Electron Ion Coincidence Studies on N_2O ," *J. Chem. Phys.* 89, 4054 (1988).
59. K.-H. Scharfner, "Highly Charged Recoil Ions," in Fundamental Processes in Energetic Atomic Collisions, edited by H. O. Lutz, J. S. Briggs, and H. Kleinpoppen, Series B, Vol. 103 (Plenum Press, New York, 1983) p. 637.
60. A. S. Schlachter, W. Groh, A. Müller, H. F. Beyer, R. Mann, and R. E. Olson, "Production of Highly Charged Rare-Gas Recoil Ions by 1.4 MeV/amu U^{92+} ," *Phys. Rev. A* 26, 1373 (1982).
61. W. Eberhardt, T. K. Sham, R. Carr, S. Krummacher, M. Strongin, S. L. Weng, and D. Wesner, "Site-Specific Fragmentation of Small Molecules Following Soft X-ray Excitation," *Phys. Rev. Lett.* 50, 1038 (1983).
62. K. Müller-Dethlefs, M. Sander, L. A. Chewter, and E. W. Schlag, "Site-Specific

Excitation in Molecules at Very High Energies: Changes in Ionization Patterns of CF_3CH_3 ," J. Phys. Chem. 88, 6098 (1984).

63. P. Morin, G. G. B. de Souza, I. Nenner, and P. Lablanquie, "Selective Resonant Photoionization Processes Near the Si 2p Edge of Tetramethylsilane," Phys. Rev. Lett. 56, 131 (1986).
64. W. Habenicht, H. Baiter, K. Müller-Dethlefs, and E. W. Schlag, "Selective Fragmentation of Nitrous Oxide by Site-Specific N (1s) Excitation Using Soft X-Ray Synchrotron Radiation," Phys. Scripta 41, 814 (1990).
65. L. Friedman and J. Bigeleisen, "Oxygen and Nitrogen Isotope Effects in the Decomposition of Ammonium Nitrate," J. Chem. Phys. 18, 1325 (1950).
66. T. Matsuo, T. Tonuma, M. Kase, T. Kambara, H. Kumagai, and H. Tawara, "Production of Multiply Charged Ions from CO and CO_2 Molecules in Energetic Heavy-Ion Impact," Chem. Phys. 121, 93 (1988).
67. D. M. Curtis and J. H. D. Elands, "Coincidence Studies of Doubly Charged Ions Formed by 30.4 nm Photoionization," Int. J. Mass. Spectrom. Ion Processes 63, 241 (1985).
68. S. D. Price, J. H. D. Elands, P. G. Fournier, J. Fournier, and P. Millie, "Electronic States and Decay Mechanisms of the N_2O^{2+} Dication," J. Chem. Phys. 88, 1511 (1988).
69. F. P. Larkins, W. Eberhardt, In-Whan Lyo, R. Murphy, and W. E. Plummer, "The Core Hole Decay of N_2O Following Core to Bound State Excitation," J. Chem. Phys. 88, 2948 (1988).
70. A. P. Hitchcock, C. E. Brion, and M. J. Van der Wiel, "Ionic Fragmentation of Inner Shell Excited States of CO_2 and N_2O ," Chem. Phys. Lett. 66, 213 (1979).
71. A. D. Bandrauk, private communication.
72. N. Levasseur and P. Millié, "Potential Energy Surfaces of the Low-Lying States of N_2O^{+} and Photodissociation Mechanisms," J. Chem. Phys. 92, 2974 (1990).
73. I. Nenner, P. Morin, P. Lablanquie, M. Simon, N. Levasseur, et P. Millié, "Photodissociation of Core Excited Molecules," J. Electron Spectrosc. Relat. Phenom. 52, 623 (1990).
74. C. K. Rhodes, "Physical Processes at High Field Strengths," Physica Scripta T 17, 193 (1987).
75. A. McPherson, G. Gibson, H. Jara, U. Johann, T. S. Luk, I. A. McIntyre, K. Boyer, and C. K. Rhodes, "Studies of Multiphoton Production of Vacuum Ultraviolet Radiation in the Rare Gases," J. Opt. Soc. Am. B 4, 595 (1987).
76. R. Rosman, G. Gibson, K. Boyer, H. Jara, T. S. Luk, I. A. McIntyre, A. McPherson, J. C. Solem, and C. K. Rhodes, "Fifth-Harmonic Production in Neon and Argon with Picosecond 248-nm Radiation," J. Opt. Soc. Am. B 5, 1237 (1988).

77. L. A. Lompré, A. L'Huillier, M. Ferray, P. Monot, G. Mainfray, and C. Manus, "High-Order Harmonic Generation in Xenon: Intensity and Propagation Effects," *J. Opt. Soc. Am. B* 7, 754 (1990).
78. G. Gibson, T. S. Luk, A. McPherson, and C. K. Rhodes, "Generation of Coherent EUV and IR Radiation Using Six-Wave Mixing in Argon," *Phys. Rev. A*, 43, 371 (1991).
79. H. M. Milchberg, R. R. Freeman, S. C. Davey, and R. M. More, "Resistivity of a Simple Metal from Room Temperature to 10^6 K," *Phys. Rev. Lett.* 61, 2364 (1988).
80. M. M. Murnane, H. C. Kapteyn, and R. W. Falcone, "High-Density Plasmas Produced by Ultrafast Laser Pulses," *Phys. Rev. Lett.* 62, 155 (1989).
81. J. C. Kieffer, P. Audebert, M. Chaker, J. P. Matte, H. Pépin, T. W. Johnston, P. Maine, D. Meyerhofer, J. Delettrez, D. Strickland, P. Bado, and G. Mourou, "Short-Pulse Laser Absorption in Very Steep Plasma Density Gradients," *Phys. Rev. Lett.* 62, 760 (1989).
82. J. A. Cobble, G. A. Kyrala, A. A. Hauer, A. J. Taylor, C. C. Gomez, N. D. Delamater, and G. T. Schappert, "Kilovolt X-Ray Spectroscopy of a Subpicosecond-Laser-Excited Source," *Phys. Rev. A* 39, 454 (1989).
83. R. Fedosejevs, R. Ottmann, R. Sigel, G. Kühnie, S. Szatmári, and F. P. Schäfer, "Absorption of Femtosecond Laser Pulses in High-Density Plasma," *Phys. Rev. Lett.* 64, 1250 (1990).
84. C. H. Nam, W. Tighe, E. Valeo, and S. Suckewer, "The Effect of Prepulse on X-Ray Laser Development Using a Powerful Subpicosecond KrF⁺ Laser," *Appl. Phys. B* 50, 276 (1990).
85. A. Zigler, P. G. Burkhalter, D. J. Nagel, M. D. Rosen, K. Boyer, G. N. Gibson, T. S. Luk, A. McPherson, C. K. Rhodes, "Measurement of Energy Penetration Depth of Subpicosecond Laser-Energy into Solid Density Matter," submitted to *Appl. Phys. Lett.*
86. M. H. R. Hutchinson, I. A. McIntyre, G. N. Gibson, and C. K. Rhodes, "Measurement of 248-nm, subpicosecond pulse durations by two-photon fluorescence of xenon excimers," *Opt. Lett.* 12, 102 (1987).
87. R. P. Madden, D. L. Ederer, and K. Codling, "Resonances in the Photo-Ionization Continuum of Ar I (20–150 eV)," *Phys. Rev.* 177, 136 (1969).
88. S. Bashkin and J. O. Stoner, Jr. Atomic Energy Level and Grottrian Diagrams (North-Holland, Amsterdam, 1975–1982), Vols. 1–4 and addenda.
89. B. C. Fawcett, A. Ridgeley, and G. E. Bromage, "The Spectrum ArIX and Extended Spectral Classification in ArV to ArVIII and ArX," *Phys. Scr.* 18, 315 (1978).
90. M. C. Buchet-Poulizac, J.-P. Buchet, and P. Ceyzeriat, *Nucl. Instrum. Methods* 202, 13 (1982).
91. A. E. Livingston, L. J. Curtis, R. M. Schectman, and H. G. Berry, "Energies and Lifetimes of Excited States in Copperlike Kr VIII," *Phys. Rev. A* 21, 771 (1980).

92. K.-T. Chang and Y.-K. Kim, "Energy Levels, Wavelengths, and Transition Probabilities of Ca-Like Ions," *At Data Nucl. Data Tables* 22, 547 (1978).
93. E. H. Pinnington, W. Ansbacher, and J. A. Kernahan, "Energy-Level and Lifetime Measurements for Kr VII," *J. Opt. Soc. Am. B* 1, 30 (1984).
94. M. Druetta and J. P. Buchet, "Beam-Foil Study of Krypton between 400 and 800 Å," *J. Opt. Soc. Am.* 66, 433 (1976).
95. D. J. G. Irwin, J. A. Kernahan, E. H. Pinnington, and A. E. Livingston, "Beam-Foil Mean - Life Measurements in Krypton," *J. Opt. Soc. Am.* 66, 1396 (1976).
96. L. J. Curtis and D. G. Ellis, "A Formula for Cancellation Disappearances of Atomic Oscillator Strengths," *J. Phys. B* 11, L543 (1978).
97. L. A. Jones and E. Källne, "A Study of the VUV Emission from Highly Ionized Krypton in a Theta Pinch Plasma," *J. Quant. Spectrosc. Radiat. Transfer* 30, 317 (1983).
98. J. Sugar and V. Kaufman, "Resonance Lines in the Pd I Isoelectronic Sequence: I VIII to Ho XXII," *Phys. Scr.* 26, 419 (1982).
99. J. R. Roberts, E. J. Krysaugas, and J. Sugar, "One-Electron Spectrum of Xe VIII," *J. Opt. Soc. Am.* 69, 1620 (1979).
100. V. Kaufman and J. Sugar, "Ag I-Like Array $4d^{10}5s - 4d^95s5p$ of I VII through Eu XVII," *J. Opt. Soc. Am. B* 1, 38 (1984).
101. E. J. Krystaugas, J. Sugar, and J. R. Roberts, "New Line Classifications and Energy Levels in the Triplet System of Xe VIII," *J. Opt. Soc. Am.* 69, 1726 (1980).
102. J. Blackburn, P. K. Carroll, J. Costello, and G. O'Sullivan, "Spectra of Xe VII, VIII, and IX in the Extreme Ultraviolet: $4d$ - mp , nf Transitions," *J. Opt. Soc. Am.* 73, 1325 (1983).
103. K. Codling and R. P. Madden, "Resonances in the Photoionization Continuum of Kr and Xe," *Phys. Rev. A* 4, 2261 (1971).
104. D. L. Ederer, "Cross-Section Profiles of Resonances in the Photoionization Continuum of Krypton and Xenon (600-400 Å)," *Phys. Rev. A* 4, 2263 (1971).
105. V. Kaufman and J. Sugar, "Ag I Isoelectronic Sequence: Wavelengths and Energy Levels for I VII through LaXI," *Phys. Scr.* 24, 738 (1981).
106. N. J. Peacock, R. J. Speer, and M. G. Hobby, "Spectra of Highly Ionized Neon and Argon in a Plasma Focus Discharge," *J. Phys. B* 2, 798 (1969).
107. C. W. Clark, M. G. Littman, R. Miles, T. J. McIlrath, C. H. Skinner, S. Suckewer, and E. Valeo, "Possibilities for Achieving X-Ray Lasing Action by Use of High-Order Multiphoton Processes," *J. Opt. Soc. Am. B* 3, 321 (1986).
108. G. Gibson, R. Rosman, T. S. Luk, I. A. McIntyre, A. McPherson, G. Wendin, K. Boyer, and C. K. Rhodes, "Characteristics of a Non-Equilibrium Picosecond Laser Plasma," OSA Proceedings on Short Wavelength Coherent Radiation:

Generation and Application, R. W. Falcone and J. Kirz, editors, (Optical Society of America, Washington D.C. 1988), p. 246.

109. L. J. Frasinski, K. Codling, and P. A. Hatherly, "Multiphoton Multiple Ionization of N_2 Probed by Covariance Mapping," preprint 1988.
110. W. Eberhardt, E. W. Plummer, I.-W. Lyo, R. Carr and W. K. Ford, "Auger-Electron-Ion Coincidence Studies of Soft X-Ray-Induced Fragmentation of N_2 ," Phys. Rev. Lett. 58, 207 (1987).
111. H. Ågren, "On the Interpretation of Molecular Valence Auger Spectra," J. Chem. Phys. 75, 1267 (1981).
112. A. Lofthus and P. H. Krupenie, "The Spectrum of Molecular Nitrogen," J. Phys. Chem. Ref. Data 6, 113 (1977).
113. R. W. Wetmore and R. K. Boyd, "Theoretical Investigation of the Dication of Molecular Nitrogen," J. Phys. Chem. 90, 5540 (1986).
114. G. Herzberg, private communication.
115. R. S. Mulliken and W. C. Ermler, Diatomic Molecules, Results of ab initio Calculations (Academic Press, New York, 1977) p. 127.
116. A. C. Wahl, "Molecular Orbital Densities: Pictorial Studies, Comparisons of the Hydrogen, Lithium, Boron, Carbon, Nitrogen, Oxygen, and Fluorine Molecules," Science 151, 961 (1966).
117. K. Boyer, and C. K. Rhodes, "Atomic Inner-Shell Excitation Induced by Coherent Motion of Outer-Shell Electrons," Phys. Rev. Lett. 54, 1490 (1987).
118. P. Lambropoulos, "Mechanisms for Multiple Ionization of Atoms by Strong Pulsed Lasers," Phys. Rev. Lett. 55, 2141 (1985).
119. A. Szöke and C. K. Rhodes, "Theoretical Model of Inner-Shell Excitation by Outer-Shell Electrons," Phys. Rev. Lett. 56, 720 (1986).
120. Q. Su, J. A. Eberly, and J. Javarainen, "Dynamics of Atomic Ionization Suppression and Electron Localization in an Intense High-Frequency Radiation Field," Phys. Rev. Lett. 64, 862 (1990).
121. M. Pont, N. R. Walet, M. Gavrilă, and C. W. McCurdy, "Dichotomy of the Hydrogen Atom in Superintense, High-Frequency Laser Field," Phys. Rev. Lett. 61, 939 (1988).
122. M. V. Fedorov and A. M. Movsesian, "Interference Suppression of Photoionization of Rydberg Atoms in a Strong Electromagnetic Field," J. Opt. Soc. Am. B 6, 928 (1989).
123. J. Parker and C. R. Stroud, Jr., "Population Trapping in Short-Pulse Laser Ionization," Phys. Rev. A 41, 1602 (1990).
124. J. H. Scofield, "Radiative Transitions," in Atomic Inner-Shell Processes, Vol. I, edited by Bernd Crasemann (Academic Press, New York, 1975), p. 265.

125. A. Zigler, P. G. Burkhalter, D. J. Nagel, K. Boyer, T. S. Luk, A. McPherson, J. C. Solem, and C. K. Rhodes, "High Intensity Generation of 9–13 Å X-Ray from BaF₂ Targets," submitted to Appl. Phys. Lett.
126. A. Zigler, P. G. Burkhalter, D. J. Nagel, M. D. Rosen, K. Boyer, T. S. Luk, A. McPherson, and C. K. Rhodes, "Plasma Production from Ultraviolet Transmitting Targets Using Subpicosecond Ultraviolet Radiation," Opt. Lett., submitted.
127. P. Simon, H. Gerhardt, and S. Szatmári, "Intensity-Dependent Loss Properties of Window Materials at 248 nm," Opt. Lett. 14, 1207 (1989).
128. E. F. Plechaty, D. E. Cullen, and R. J. Howerton, "Tables and Graphs of Photon-Interaction Cross Sections from 0.1 keV to 100 MeV Derived from the LLL Evaluated-Nuclear-Data Library," UCRL-50400, Vol. 6, Rev. 3, 11 November 1981, p. 268.
129. E. J. McGuire, "Atomic M-Shell Coster-Kronig, Auger, and Radiative Rates, and Fluorescence Yields for Ca-Th," Phys. Rev. A 5, 1043 (1972).
130. W. Bambynek, B. Crasemann, R. W. Fink, H.-U. Freund, H. Mark, C. D. Swift, R. E. Price, P. V. Rao, "X-Ray Fluorescence Yields, Auger, and Coster-Kronig Transition Probabilities," Rev. Mod. Phys. 44, 716 (1972).
131. M. Ya. Amusia, Atomic Photoeffect (Plenum Press, New York, 1990) p. 292.
132. T. A. Carlson, W. E. Hunt, and M. O. Krause, "Relative Abundances of Ions Formed as the Result of Inner-Shell Vacancies in Atoms," Phys. Rev. 151, 41 (1966).
133. A. Z. Devdariani, T. M. Kereselidze, and A. L. Zagrebin, "Formation of Vacancies in Inner Electron Shells of Fragments in Nuclear Fission of Heavy Elements," J. Phys. B 23, 2457 (1990).
134. N. Stolterfoht, C. C. Havener, R. A. Phaneuf, J. K. Swenson, S. M. Shafrath, and F. W. Meyer, "Evidence for Correlated Double-Electron Capture in Low-Energy Collisions of O⁸⁺ with He," Phys. Rev. Lett. 57, 74 (1986).
135. G. Soff, V. Oberacker, and W. Greiner, "Inner-Shell Ionization by Nuclear Coulomb Excitation in Collisions of Very Heavy Ions," Phys. Rev. Lett. 41, 1167 (1978).
136. L. N. Ivanov, U. I. Safronova, V. S. Serashenko, and D. S. Viktorov, "The Radiationless Decay of Excited States of Atomic Systems with Two K-Shell Vacancies," J. Phys. B 11, L175 (1978).
137. Ch. Stoller, W. Wölfl, G. Bonani, M. Stöckli, and M. Suter, "Two-Electron One-Photon Transitions into the Doubly Ionized K Shell," Phys. Rev. A 15, 990 (1977).
138. P. H. Mokler and F. Folkmann, "X-Ray Production in Heavy Ion-Atom Collisions" in Structure and Collisions of Ions and Atoms, edited by I. A. Sellin (Springer-Verlag, Berlin, 1978) p. 201.
139. G. Dujardin, L. Hellner, B. J. Olsson, M. J. Besnard-Ramage, and A. Dadouch, "Negative-Fragment-Ion Formation by Photon Excitation of Molecules in the

- Vicinity of the Core-Ionization and Direct-Double Ionization Thresholds," Phys. Rev. Lett. 62, 745 (1989).
140. T. J. M. Zouros, D. H. Lee, and P. Richard, "Projectile $1s \rightarrow 2s$ Excitation Due to Electron-Electron Interaction in Collisions of O^{5+} and F^{6+} Ions with H_2 and He Targets," Phys. Rev. Lett. 62, 2261 (1989).
 141. Excimer Lasers, Second Edition, edited by C. K. Rhodes (Springer-Verlag, Berlin, 1984).
 142. K. Boyer, G. Gibson, H. Jara, T. S. Luk, I. A. McIntyre, A. McPherson, R. Rosman, J. C. Solem, C. K. Rhodes, "Corresponding Aspects of Strong-Field Multiquantum Processes and Ion-Atom Collisions," IEEE Trans. Plasma Science 16, 541 (1988).
 143. K.-H. Scharfner, "Highly Charged Recoil Ions," in Fundamental Processes in Energetic Atomic Collisions, edited by H. O. Lutz, J. S. Briggs, and H. Kleinpoppen, Series B, Vol. 103 (Plenum Press, New York, 1983) p. 637.
 144. A. S. Schlachter, W. Groh, A. Müller, H. F. Beyer, R. Mann, and R. E. Olson, "Production of Highly Charged Rare-Gas Recoil Ions by 1.4 MeV/amu U^{92+} ," Phys. Rev. A 26, 1373 (1982).
 145. T.W.B. Kibble, "Refraction of Electron Beams by Intense Electromagnetic Waves," Phys. Rev. Lett. 16, 1054 (1966).
 146. A. Szöke, "Interpretation of Electron Spectra Obtained from Multiphoton Ionization of Atoms in Strong Fields," J. Phys. B 18, L427 (1985).
 147. "Charge-Displacement Self-Channeling as a Method for Energy Concentration," K. Boyer, T. S. Luk, J. C. Solem and C. K. Rhodes, OSA Proceedings on Short Wavelength Coherent Radiation: Generation and Application, R. W. Falcone and J. Kirz, editors, (Optical Society of America, Washington, D. C., 1988), p. 233.
 148. P. Sprangle, Cha-Mei Tang, and E. Esarey, "Relativistic Self-Focusing of Short-Pulse Radiation Beams in Plasmas," IEEE Trans. Plasma Science 15, 145 (1987).
 149. J. C. Solem, T. S. Luk, K. Boyer, and C. K. Rhodes, "Prospects for X-Ray Amplification with Charge-Displacement Self-Channeling," IEEE J. Quantum Electron. QE-25, 2423 (1989).
 150. P. Sprangle, E. Esarey, and A. Ting, "Nonlinear Interaction of Intense Laser Pulses in Plasmas," Phys. Rev. A 41, 4463 (1990).
 151. P. Sprangle, E. Esarey, and A. Ting, "Nonlinear Theory of Intense Laser-Plasma Interaction," Phys. Rev. Lett. 64, 2011 (1990).
 152. T. Kurki-Suonio, P. J. Morrison, and T. Tajima, "Self-Focusing of an Optical Beam in a Plasma," Phys. Rev. A 40, 3230 (1989).
 153. A. B. Borisov, A. V. Borovskiy, V. V. Korobkin, A. M. Prokhorov, C. K. Rhodes, O. B. Shiryayev, "Stabilization of Relativistic Self-Focusing of Intense Subpicosecond Ultraviolet Pulses in Plasmas," Phys. Rev. Lett. 65, 1753 (1990).

VI. APPENDICES

Appendix A: "Measurement of Energy Penetration Depth of Subpicosecond Laser
Energy into Solid Density Matter"

Measurement of energy penetration depth of subpicosecond laser energy into solid density matter

A. Zigler,^{a)} P. G. Burkhalter, and D. J. Nagel
Naval Research Laboratory, Washington, DC 20375

M. D. Rosen
Lawrence Livermore Laboratory, Livermore, California 94550

K. Boyer, G. Gibson, T. S. Luk, A. McPherson, and C. K. Rhodes
University of Illinois at Chicago, P. O. Box 4348, Chicago, Illinois 60680

(Received 21 January 1991; accepted for publication May 1991)

The energy penetration depth characteristic of the interaction of intense subpicosecond (~ 600 fs) ultraviolet (248 nm) laser radiation with solid density material has been experimentally determined. This was accomplished by using a series of ultraviolet transmitting targets consisting of a fused silica (SiO_2) substrate coated with an 80–600 nm layer of MgF_2 . The measurement of He-like and H-like Si and Mg lines, as a function of MgF_2 thickness, enabled the determination of the energy penetration depth. It was found that this depth falls in the range of 250–300 nm for a laser intensity of $\sim 3 \times 10^{16}$ W/cm². Based on numerical simulations, it is estimated that solid density material to a depth of ~ 250 nm is heated to an electron temperature of ~ 500 eV.

Recently developed subpicosecond high intensity lasers are enabling the generation of high-energy density plasmas which can be used both to test our understanding of the dynamics of highly excited solids and for the development of ultrafast x-ray sources.^{1–3} The use of subpicosecond laser pulses to produce such dense plasmas significantly simplifies the analysis of the laser-plasma interaction, since hydrodynamic expansion of the plasma during the laser pulse is relatively small. It is crucial to understand the electron thermal conduction process under these conditions, since it governs both the peak temperature achieved during the laser pulse and the subsequent cooling rate, thus controlling the intensity and duration of the x-ray pulse produced.

The theoretical uncertainties involving electron heat transport arise mainly due to the presence of a steep thermal gradient ($\sim \text{eV}/\text{\AA}$). The classical treatment of thermal conduction is a local analysis,⁴ wherein the scale length of the temperature gradient is assumed to be much larger than the electron mean free path. For subpicosecond laser plasmas, this condition does not necessarily hold, so a non-local treatment,⁵ in which hot electrons stream into cooler regions, may become necessary. In the absence of a sophisticated nonlocal description, hydrodynamic simulation codes, when treating gradients with a scale length as short as a mean free path, simply preserve causality by limiting the heat flux to be less than $f n v T$, where n is the electron density, v the electron thermal velocity, and T the electron temperature. In this expression f is the "flux limiter," a free parameter,⁶ usually with a magnitude of ~ 0.1 .

In this letter we report on the experimental determination of the heat penetration depth of the laser-plasma interaction. This is accomplished by monitoring the absolute intensities of the characteristic line radiation emitted from a series of ultraviolet transmitting targets consisting

of a fused silica (SiO_2) substrate coated with MgF_2 layers of known thickness. Measurements of the relative emissions radiated by highly ionized Si and Mg atoms are then used to establish the depth of energy penetration. Since a subpicosecond KrF^* laser was used to irradiate the targets in this study, it is important that both constituents of the layered targets are sufficiently transparent to low levels of the ultraviolet (248 nm) radiation that no prepulse plasma is formed.⁷

The laser system⁸ used in the present study ($\text{KrF}^*/248$ nm) delivered a subpicosecond pulse (~ 600 fs) having an energy of 135 ± 15 mJ. An accompanying prepulse (ASE) had a duration of ~ 20 ns, an energy of 8–30 mJ, and was focusable to a spot with an area of $\sim 8 \times 10^{-2}$ cm². The effect of the prepulse has been carefully considered. Substrates exposed to the ASE show no evidence, under microscopic examination, of a tightly focusable (~ 10 μm diameter) component. Only the larger ($\sim 8 \times 10^{-2}$ cm²) pattern can be made visible on suitably absorbing materials. Also, theoretical estimates of the maximum focusable intensity arising from the ASE are found to be well below damage thresholds for the target materials used. All the available experimental evidence⁷ and analysis indicate that no prepulse plasma was formed in these experiments.

The subpicosecond radiation was focused onto a flat rotation target using an $f/10$ CaF_2 lens. The peak laser intensity achievable on target arising from the subpicosecond pulse was estimated to be $\sim 10^{17}$ W/cm². This estimated intensity is based on direct imaging of the ultraviolet focal zone with a microscope and CCD camera, a measurement which indicated a focal spot diameter of ~ 10 μm . In order to perform this measurement, the seed beam was focused onto a surrogate target composed of a 250- μm -thick planar pyrex substrate. This target, which completely absorbs the ultraviolet radiation in a scale length less than a micrometer, produces fluorescence from the irradiated region which is subsequently imaged with an optical mi-

^{a)}Also associated with F. M. Technologies, Fairfax, VA 22032.

croscope having a resolution of $\sim 0.5 \mu\text{m}$.

X-ray pinhole camera measurements⁹ were used to examine the focal region at full beam power. For these measurements a pinhole camera used DEF film and a filter composed of two 1000 Å layers of Al on a 2- μm -thick polycarbonate substrate. The camera had a 5 μm pinhole and yielded a magnification of 8.2 ± 0.2 on the recording film. The x-ray emission was measured by viewing at an angle of 45° with respect to the target normal. The target used for this examination of the focal spot was SiO_2 coated with 250 nm of MgF_2 . The pinhole camera recorded a radiating plasma with a diameter in the range of 8–9 μm for radiation in the kilovolt spectral region. Furthermore, subsequent microscopic examination of the SiO_2 target surface revealed 6–7- μm -diam craters. These findings are in reasonable correspondence with the measurement of the focusability of the laser seed beam described above.

In these experiments, the emissions of H-like ($1s-2p$) La and He-like ($1s^2-1s3p$) $\text{He}\beta$ lines, from both Si and Mg, were monitored as a function of both incident laser intensity and target MgF_2 layer thickness. Using the imaging technique described above to monitor the focal dimensions, several positions of the focusing lens were selected in order to vary the incident peak laser intensity. The x-ray emission from the targets was collected by flat KAP ($2d = 26.6 \text{ \AA}$) and ADP ($2d = 10.64 \text{ \AA}$) crystal spectrometers using DEF film. The spectrometers contained filters composed of two 1000 Å layers of Al on a 2- μm -thick polycarbonate substrate for shielding the DEF film from unwanted radiation. Each spectrum was produced by 25 laser shots and the absolute line intensities were deduced from published data on the spectrograph-crystal efficiency,¹⁰ the filter transmission, and the film calibration.¹¹

The experiments discussed below were modeled using the LASNEX simulation code. This analysis involves the solution of a system of nonlocal thermodynamic equilibrium rate equations, which incorporates a hydrogenic atomic model for each of the elements ($\text{Mg}, \text{Si}, \text{O}, \text{F}$), along with flux-limited thermal conduction ($f = 0.1$) and Lagrangian hydrodynamics.¹² In particular, the process of thermal conduction was treated in the manner described by Lee and More.¹³

The measured absolute line intensities of the Si and Mg La and $\text{He}\beta$ lines from bare (uncoated) SiO_2 and MgF_2 targets, as a function of incident laser intensity, are shown in Fig. 1 along with the corresponding LASNEX simulations. These measurements were performed in order to test how well the LASNEX code represented the interaction. Assuming that 30% of the incident laser energy is absorbed by the target, the LASNEX calculation agrees well with the experimental data up to an irradiance of $\sim 2\text{--}3 \times 10^{16} \text{ W/cm}^2$. A deviation between the theoretical results and the experimental data, however, is indicated at the highest laser intensity of $\sim 10^{17} \text{ W/cm}^2$. For comparison, an absorption of 10% was assumed for laser intensities above $\sim 1.5 \times 10^{16} \text{ W/cm}^2$. Support for the use of this value comes from the recent work at high intensity by Murnane *et al.*³ These calculations produce a reasonable match of the data corresponding to the maximum intensity

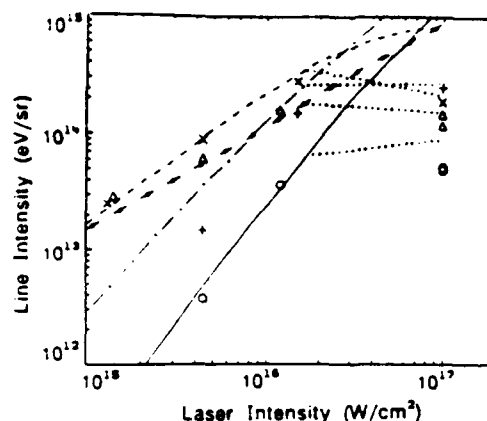


FIG. 1. Absolute line intensities of Si (La \circ and $\text{He}\beta$ Δ) and Mg (La \square and $\text{He}\beta$ \times) radiation measured as a function of incident laser intensity using bare SiO_2 and MgF_2 targets. The curves represent LASNEX calculations assuming an energy absorption of 30% [— (solid) Si La , —•— (closed dash-dot) Si $\text{He}\beta$, - - - (open dash-dot) Mg La , - - - (dash) Mg $\text{He}\beta$] and, beginning at an intensity of $1.5 \times 10^{16} \text{ W/cm}^2$, an energy absorption of 10%, shown by the corresponding extensions with dotted lines.

($\sim 10^{17} \text{ W/cm}^2$) used in these studies. Therefore, for the range of intensity examined, an absorption of laser energy in the 10–30% range is indicated. A variation of this magnitude could arise from an absorption dynamically dependent on the incident laser intensity. Further studies over a larger range of intensity will be needed to more fully understand the nature of this dependence. Nevertheless, the LASNEX simulation is found to give a reasonable representation of the experimental results for the conditions of this work.

The energy penetration depth was determined by monitoring the change of the absolute intensity of the La line emitted by H-like Si as a function of MgF_2 coating thickness. Figure 2 presents the absolute line intensities of both Si and Mg La and $\text{He}\beta$ lines as a function of MgF_2 coating thickness. The measurements were carried out for a peak incident laser intensity of $\sim 3 \times 10^{16} \text{ W/cm}^2$, an intensity for which the LASNEX simulation seems adequate. As seen, the Si La line intensity decreases rather sharply, by a factor of approximately e from the bare target interaction, for a coating thickness in the range of 250–300 nm, indicating that the energy penetrates to a depth of this scale. Qualitatively similar behavior is exhibited by the Si $\text{He}\beta$ transition. Moreover, both the Mg La and $\text{He}\beta$ lines show the expected corresponding increase in the same range of thickness.

The results stemming from the LASNEX simulations for these four lines are also shown in Fig. 2. For the Si La and $\text{He}\beta$ transitions, it is seen that the slope representing the rate of decrease of the line intensities is roughly within a factor of 2 of the experimentally observed behavior in the region where most of the energy is deposited (MgF_2 thickness $< 200 \text{ nm}$). A larger deviation occurs in the region in which the signal is relatively small (thickness $> 200 \text{ nm}$). This difference at the larger depths indicates that some corrections in the energy transport including the possibility of nonlocal heat conduction, are indicated, but that these

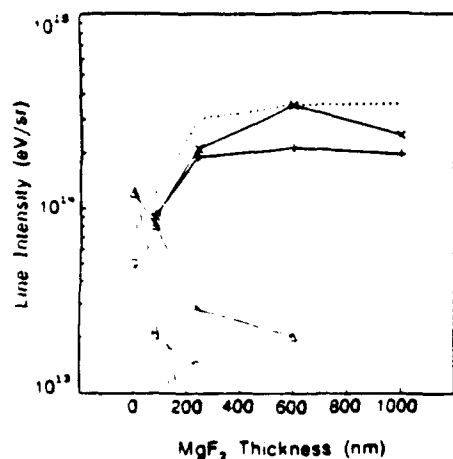


FIG. 2. Absolute line intensities of Si and Mg $L\alpha$ and He β radiation as a function of MgF_2 thickness on SiO_2 substrates. The measured data are represented as (○) Si $L\alpha$; (Δ) Si He β ; (+) Mg $L\alpha$; (\times) Mg He β . Solid curves are drawn through the data to guide the eye. The data points indicated at 1000 nm of MgF_2 are for bare MgF_2 targets. The corresponding LASNEX calculations assuming 30% absorption and an incident laser intensity of $\sim 3 \times 10^{16}$ W/cm 2 , are also shown with designations given by -- (dash-dot) Si $L\alpha$, --- (dash) Si He β , ... (small dot) Mg $L\alpha$, (large dot) Mg He β .

effects are relatively small and do not involve a substantial fraction of the energy. For the Mg $L\alpha$ and He β lines, the LASNEX simulations are seen to agree quite well with the measured data over the full range of conditions studied.

While the data presented in Fig. 2 indicate that the heat wave penetrates to a depth of ~ 250 nm, these data do not directly reveal the electron temperature to which the material is heated. In order to estimate the peak temperature achieved during the excitation, the electron temperature was calculated as a function of the incident laser intensity by the LASNEX code. The results of these calculations are shown in Fig. 3. For the laser intensity used in the determination of the energy penetration depth $\sim 3 \times 10^{16}$ W/cm 2 , the results of this analysis indicate that the electron temperature reaches a value of ~ 500 eV to a depth of ~ 250 nm inside the solid target material.

Spectral studies of layered SiO_2/MgF_2 targets reveal that an energy penetration depth of 250–300 nm is produced with subpicosecond excitation at 248 nm with an intensity of $\sim 3 \times 10^{16}$ W/cm 2 . This value is considerably in excess of the skin depth associated with the plasma being produced. LASNEX modeling of the interaction was found to be in good agreement over the range of conditions studied. An estimate of the electron temperature of the heated material, as indicated by the LASNEX simulation, gives a value of ~ 500 eV at a depth of ~ 250 nm inside the solid material.

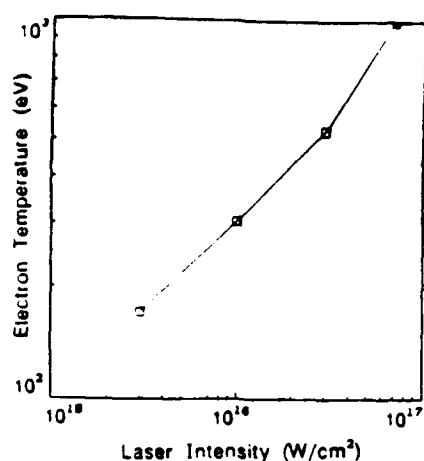


FIG. 3. LASNEX calculations of electron temperature as a function of peak laser irradiance. Calculations are for a peak electron density of 6×10^{21} cm $^{-3}$ at the time of peak laser irradiance, with the assumption of 30% absorption for all irradiances.

The authors gratefully acknowledge technical contributions from K. Hudson, and D. Newman of Sachs-Freeman Associates, Inc., and P. Noel and J. Wright of the University of Illinois at Chicago. Support for this research was provided by the U.S. Air Force Office of Scientific Research, the U.S. Office of Naval Research, and the Strategic Defense Initiative Organization. Part of this work (MDR) was performed under the auspices of the U.S. Department of Energy by the Lawrence Livermore National Laboratory under contract No. W-7405-ENG-48.

¹M. M. Murnane, H. C. Kapteyn, and R. W. Falcone, *Phys. Rev. Lett.* **62**, 155 (1989).

²H. M. Milchberg, R. R. Freeman, S. C. Davey, and R. M. More, *Phys. Rev. Lett.* **61**, 2364 (1989).

³M. M. Murnane, H. C. Kapteyn, M. D. Rosen, and R. W. Falcone, *Science* **251**, 531 (1991).

⁴J. H. Rogers, J. S. DeGroot, E. Abou-Assaleh, J. P. Matte, T. W. Johnson, and M. D. Rosen, *Phys. Fluids B* **1**, 741 (1989).

⁵M. K. Prasad, R. A. Sacks, M. D. Rosen, and B. F. Lasinski, *Bull. Am. Phys. Soc.* **33**, 1994 (1988).

⁶M. D. Rosen, *Comm. Plasma Phys. Controlled Fusion* **8**, 165 (1984).

⁷A. Zigler, P. G. Burkhalter, D. J. Nagel, M. D. Rosen, K. Boyer, T. S. Luk, A. McPherson, and C. K. Rhodes, *Opt. Lett.* **16**, 1 August (to be published, 1991).

⁸T. S. Luk, A. McPherson, G. N. Gibson, K. Boyer, and C. L. Rhodes, *Opt. Lett.* **14**, 1113 (1989).

⁹A. Zigler, P. E. Burkhalter, D. J. Nagel, B. Boyer, T. S. Luk, A. McPherson, J. C. Solem, and C. K. Rhodes, *Appl. Phys. Lett.* **59**, August (to be published, 1991).

¹⁰D. B. Brown and M. Fatemi, *J. Appl. Phys.* **51**, 2540 (1980); *J. Appl. Cryst. Appl. Spectrosc.* **33**, 19 (1979); J. V. Gilfrich, D. B. Brown, P. G. Burkhalter, *Appl. Spectrosc.* **29**, 322 (1975).

¹¹P. D. Rockett, C. R. Bird, C. J. Hailey, D. Sullivan, D. B. Brown, P. G. Burkhalter, *Appl. Opt.* **24**, 2536 (1985).

¹²G. B. Zimmerman and W. L. Kruer, *Comm. Plasma Phys.* **11**, (1975).

¹³Y. Lee and R. M. More, *Phys. Fluids* **27**, 1273 (1984).

Appendix B: "High Intensity Generation of 9–13 Å X-Rays from BaF₂ Targets"

High intensity generation of 9–13 Å x rays from BaF₂ targets

A. Zigler,^{a)} P. G. Burkhalter, and D. J. Nagel
Naval Research Laboratory, Washington, DC 20375

K. Boyer, T. S. Luk, A. McPherson, J. C. Solem, and C. K. Rhodes
University of Illinois at Chicago, P. O. Box 4348, Chicago, Illinois 60680

(Received 2 January 1991; accepted for publication 7 June 1991)

Studies of the interaction of condensed matter with short pulse (~ 600 fs) high intensity ($\sim 10^{17}$ W/cm²) ultraviolet (248 nm) radiation show that intense spatially compact sources for x-ray emission in the kilovolt range ($0.5\text{--}1.0 \times 10^{15}$ W/cm²) can be generated from solid targets at close to the maximum volume specific rate allowed.

Solid materials offer the possibility of combining a high particle density with a very high level of electronic excitation, provided that the deposition of energy in the solid can be made to occur sufficiently rapidly. Ultraviolet high-brightness subpicosecond light sources^{1–7} enable such rapid deposition of energy to be achieved.

The laser system⁵ used in the present study (KrF⁺/248 nm) delivered a subpicosecond pulse (~ 600 fs) having an energy of 135 ± 15 mJ. An accompanying prepulse had a duration of ~ 20 ns, an energy of 8–30 mJ, and was focusable to a spot with an area of $\sim 8 \times 10^{-2}$ cm². The subpicosecond radiation was focused onto a flat rotating BaF₂ target using an f/10 CaF₂ lens. The peak laser intensity achievable on target arising from the subpicosecond pulse was estimated to be $\sim 10^{17}$ W/cm². This estimated intensity is based on direct imaging of the ultraviolet focal zone with a microscope and a charge coupled device (CCD) camera, a measurement which indicated a focal spot diameter of 6–7 μ m.

Independent x-ray pinhole camera measurements were also used to examine the focal region. For these measurements a pinhole camera using Kodak DEF film and a filter of 2000-Å-thick Al on a 2- μ m-thick polycarbonate substrate was used. The camera had a 5 μ m pinhole and yielded a magnification of 8.2 ± 0.2 on the recording film. Viewing at an angle of 45° with respect to the target normal, the x-ray emission from two types of solid targets was measured. The targets were SiO₂ coated with 250 nm of MgF₂ and bare BaF₂. The former indicated a radiating plasma with a diameter in the range of 8–9 μ m for radiation in the kilovolt spectral region. Microscopic examination of the SiO₂ target surface revealed 6–7 μ m diameter craters, a finding in reasonable correspondence with the measurement of the focusability of the laser beam described above. The measurements with the BaF₂ targets indicated a radiating plasma with a diameter of $\sim 20 \pm 4$ μ m and corresponding craters with diameters in the 8–10 μ m range were observed in the target substrate.

For spectral studies of BaF₂, the x-ray emission from the targets was collected by a flat KAP ($2d = 26.6$ Å) crystal spectrometer which produced a recording on DEF film. The absolute line intensities were deduced from extant data on the crystal efficiency,⁸ the filter transmission,

and the DEF film calibration.⁹ To insure the reproducibility of the data, the spectra were collected several times over a period of six months. The film was developed according to established procedures for the calibration of the film and the optical density was digitized at the facility at the Naval Research Laboratory. Each spectrum was produced by an exposure accumulated over 25 laser shots.

An experimental concern in studies of the interaction of intense radiation with solid matter is the effect of any low intensity prepulse on the true state of the target material. If a sufficient intensity is present in the prepulse, a plasma can be formed which will shield the solid target from the high intensity subpicosecond energy. Experimental studies, however, have demonstrated that the effect of the prepulse can be eliminated at 248 nm by using a target composed of ultraviolet transmitting materials.¹⁰ For example, MgF₂ and BaF₂ exhibit essentially no absorption¹¹ up to a relatively high intensity ($\approx 10^{11}$ W/cm²). Therefore, if the prepulse intensity is appreciably less than 10^{11} W/cm², negligible absorption is present and no interfering plasma is generated. In this case, the threshold intensity for nonlinear absorption is sufficiently high to prevent any significant influence by the prepulse in these studies, since the maximum prepulse intensity occurring was only $\sim 2.5 \times 10^7$ W/cm².

The spectrum observed from BaF₂ targets exhibited very strong emission in the 9–13 Å range, as shown in Fig. 1. The radiation in the broad band centered at ~ 12 Å arises from *M*-shell transitions of barium ions and the observed structure can be put in reasonable correspondence with the previously measured¹² $3d^n - 3d^{n-1}4f$ sequence in that material. With consideration of the response of the DEF film, the crystal response, and the filter calibrations, these measurements indicated that $\sim 2\text{--}4$ mJ of x rays were produced in this spectral region on each shot, the greater production corresponding to the higher range of the incident laser energy. The isotropy of the emission was established experimentally by recording the spectra at two widely different angles (45° and 80°) with respect to the target normal. In both cases, the properties of the recorded spectra were similar. Although the duration of the emission was not directly measured, an upper bound of 1–2 ps is consistent with (1) the size of the radiating region measured with the pinhole camera for a velocity of expansion of a few Ångströms per femtosecond, (2) with LASNEX calculations for our experimental conditions,¹³ (3) with

^{a)} Also of FM Technologies, Fairfax, VA 22032

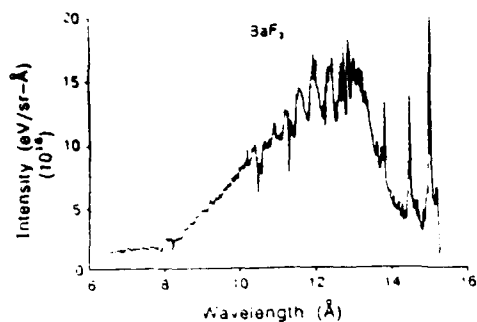


FIG. 1. Spectrum of x-ray emission observed from BaF_2 at a laser intensity of $\sim 10^{17} \text{ W/cm}^2$.

the time resolved studies of laser-produced plasmas reported by Murnane *et al.*,¹⁴ and (4) recent measurements of Cobble *et al.* with solid aluminum targets.^{15,16} The latter explicitly indicates rapid cooling that would cause the emission of kilovolt radiation to be of short duration. It follows, assuming isotropic emission from the radiating zone determined by the pinhole camera, that for BaF_2 , an x-ray intensity in the range of $5 \times 10^{14} < I_x < 10^{15} \text{ W/cm}^2$ was produced on each laser shot.

An upper bound on the x-ray intensity achievable from this type of source can be estimated by considering a slab of unit area with density ρ and thickness δ which, upon excitation with intense subpicosecond radiation, produces radiation in the kilovolt spectral range. Since the time of excitation is short, in first approximation we will ignore the hydrodynamical expansion, a process which will occur roughly at a rate of $\sim 1\text{--}10 \text{ Å/fs}$. An upper limit on the x-ray intensity I_{xm} can then be written as

$$I_{xm} \approx \hbar \omega_x \rho \delta / 2\tau_x \quad (1)$$

in which $\hbar \omega_x$ represents a kilovolt quantum and τ_x is the effective radiative rate of the excited material. For the present discussion, we will take ρ as BaF_2 solid density ($\sim 1.7 \times 10^{22} \text{ cm}^{-3}$) and use for τ_x a typical radiative rate for kilovolt transitions in atoms or ions. The latter parameter will be taken in the range¹⁷ of $2 \times 10^{-14} < \tau_x < 10^{-13} \text{ s}$.

It remains to estimate the thickness of the radiating zone denoted by δ . Using a series of $\text{MgF}_2/\text{SiO}_2$ targets coated with a range of thicknesses of MgF_2 , the measured¹⁸ depth of energy penetration, for plasmas generated at an incident laser intensity of $\sim 3 \times 10^{16} \text{ W/cm}^2$, was found to be in the range of 250–300 nm. The depth δ was deduced from the observed relative strengths of the Mg and Si H-like and He-like transitions as a function of the thickness of the MgF_2 layer. Taking this energy penetration depth for δ , the approximate upper bound represented by Eq. (1) can be evaluated. From the given ranges on τ_x and δ , and assuming that the radiating material is thin to the x rays, we find $3 \times 10^{14} < I_{xm} < 2 \times 10^{15} \text{ W/cm}^2$. The available information on opacities¹⁹ indicates that the assumption of a thin plasma is consistent with the range of δ given.

Comparison of this upper limit on I_{xm} with the experimental value I_x indicates that the observed intensity falls within the estimated range for maximum possible emission.

Although such a source is incoherent, a radiation rate of this magnitude, coupled with the relatively narrow spectrum over which it occurs, constitutes a source of extremely high spectral brightness that can produce unusually high excitation rates in absorbing material to which it can be coupled. We note that since the simple model used to estimate the upper radiative bound is far from an equilibrium picture and since the experimental result is quite close to that limit, the implication is that the plasma state may deviate significantly from equilibrium for this type of intense and rapid excitation.

In conclusion it is found that the use of high brightness ultraviolet subpicosecond light source for the study of the interaction of condensed matter with strong electromagnetic fields is leading to the development of (1) the ability to couple a strong laser field directly to solid target material, without the production of a prepulse plasma, and (2) the generation of powerful x-ray sources associated with spatially compact high density plasmas.

We acknowledge the technical assistance of P. Noel and J. Wright of UIC and Dan Newman of NRL along with helpful discussions with M. D. Rosen of LLNL, and G. N. Gibson. Support for this research was provided by the U. S. Air Office of Scientific Research, the U. S. Office of Naval Research, and the Strategic Defense Initiative Organization.

¹S. Szatmari, F. P. Schäfer, E. Müller-Horsche, and W. Mückenheim, *Opt. Commun.* **63**, 305 (1987).

²A. Endoh, M. Watanabe, N. Sarukura, and S. Watanabe, *Opt. Lett.* **7**, 353 (1989).

³J. R. M. Barr, N. J. Everall, C. J. Hooker, I. N. Ross, M. J. Shaw, and W. T. Toner, *Opt. Commun.* **56**, 127 (1988).

⁴J. G. Glowia, J. Misevich, and P. P. Sorokin, *J. Opt. Soc. Am. B* **4**, 1061 (1987).

⁵T. S. Luk, A. McPherson, G. Gibson, K. Boyer, and C. K. Rhodes, *Opt. Lett.* **14**, 1113 (1989).

⁶A. J. Taylor, C. R. Tallman, J. P. Roberts, C. S. Lester, T. R. Gosnell, P. H. Lee, and G. A. Kyrila, *Opt. Lett.* **15**, 39 (1990).

⁷A. J. Taylor, T. R. Gosnell, and J. P. Roberts, *Opt. Lett.* **15**, 118 (1990).

⁸D. B. Brown and M. Fatemi, *J. Appl. Phys.* **51**, 2540 (1980); *J. W. Criss, Appl. Spectrosc.* **33**, 19 (1979).

⁹P. D. Rockett, C. R. Bird, C. J. Hatley, D. Sullivan, D. B. Brown, and P. G. Burkhalter, *Appl. Opt.* **24**, 2536 (1985).

¹⁰A. Zigler, P. G. Burkhalter, D. J. Nagel, T. S. Luk, A. McPherson, C. K. Rhodes, and M. D. Rosen, *Opt. Lett.* (to be published).

¹¹P. Simon, H. Gerhardt, and S. Szatmari, *Opt. Lett.* **14**, 1207 (1989).

¹²G. Mehlman, P. G. Burkhalter, D. A. Newman, and B. H. Ripin, *J. Quant. Spectrosc. Radiat. Transfer* **45**, 225 (1991).

¹³M. D. Rosen (private communication).

¹⁴M. M. Murnane, H. C. Kapteyn, and R. W. Falcone, *Phys. Rev. Lett.* **62**, 155 (1989).

¹⁵J. A. Cobble, G. A. Kyrila, A. A. Hauer, A. J. Taylor, C. C. Gomez, N. D. Delameter, and G. T. Schappert, *Phys. Rev. A* **39**, 454 (1989).

¹⁶J. A. Cobble, G. T. Schappert, L. A. Jones, A. J. Taylor, G. A. Kyrila, and R. D. Fulton, *J. Appl. Phys.* **69**, 3379 (1991).

¹⁷J. H. Scofield, in *Atomic Inner-Shell Processes* edited by Bernd Crasemann (Academic, New York, 1975), Vol. I, p. 265.

¹⁸A. Zigler, P. G. Burkhalter, D. J. Nagel, T. S. Luk, A. McPherson, C. K. Rhodes, and M. D. Rosen, *Appl. Phys. Lett.* (to be published).

¹⁹E. Saloman, J. Hubbell, and J. Scofield, *At. Nucl. Data Tables* **38**, 1 (1988).

Appendix C: "Plasma Production from Ultraviolet Transmitting Targets Using Sub-picosecond Ultraviolet Radiation"

Plasma production from ultraviolet-transmitting targets using subpicosecond ultraviolet radiation

A. Zigler

F.M. Technologies, Fairfax, Virginia 22032

P. G. Burkhalter and D. J. Nagel

Naval Research Laboratory, Washington, D.C. 20375

M. D. Rosen

Lawrence Livermore National Laboratory, Livermore, California 94550

K. Boyer, T. S. Luk, A. McPherson, and C. K. Rhodes

University of Illinois at Chicago, P.O. Box 4348, Chicago, Illinois 60680

Received December 7, 1990

Plasma produced from ultraviolet-transmitting solid targets undergoing intense ($>10^{16}$ W/cm²) subpicosecond (~ 600 fs) ultraviolet (248 nm) irradiation have been studied under conditions for which no interfering prepulse plasma is generated. Time and spatially integrated measurements of the x-ray emission for H-like and He-like Mg and Si were found to be consistent with LASNEX calculations that model the laser-target interaction.

Subpicosecond high-peak-brightness lasers capable of delivering focal intensities of greater than 10^{16} W/cm² permit the generation of high-temperature plasmas from solid targets. These plasmas can produce short pulses of x rays, of the order of a picosecond or less, owing to the rapid cooling of the plasma on the solid target surface.

Numerous experiments involving plasma production with picosecond and subpicosecond lasers at different wavelengths and intensities have been reported.¹⁻⁶ An important experimental concern in subpicosecond studies involving the coupling of laser energy to solid targets is the potential influence on the target of any relatively low-intensity, but long-time-scale prepulse that may be present, since such prepulses are generally associated with amplified spontaneous emission (ASE) in high-power laser systems. Moreover, since the ablation threshold for most solid materials is less than $\sim 10^8$ W/cm², even a relatively low level of ASE originating from the laser amplifier may be sufficient to ablate and ionize the target material, creating a long-scale-length plasma and thus altering the dynamics of interaction of the intense subpicosecond pulse with the solid target. Consequently, the relatively low-density plasma that may be generated by the prepulse can severely alter the interaction of the subpicosecond energy with the solid matter.

In this Letter we report experimental findings showing that the effect of the prepulse can be eliminated when a KrF* laser system is used at 248 nm to irradiate optically polished ultraviolet-transmitting targets such as CaF₂, MgF₂, BaF₂, and SiO₂. In

addition, we report on the results of spectrally resolved x-ray emission from CaF₂, MgF₂, and SiO₂ targets irradiated at the peak intensity of $\approx 3 \times 10^{16}$ W/cm². Based on the properties of the observed line emissions, the characteristics of the plasmas generated in these studies were compared with LASNEX⁷ simulations.

The KrF* laser system used for these experiments has been described elsewhere.⁸ It operated with a pulse duration of ≈ 600 fs, had a subpicosecond pulse energy of ~ 90 mJ accompanied with ≈ 20 mJ of ASE that had a duration of ~ 20 ns, and was focused onto a rotating planar target with an $f/10$ CaF₂ lens. The accompanying prepulse (ASE) was focusable to a spot with an area of $\sim 8 \times 10^{-2}$ cm² owing to the relatively large divergence.

The effect of the prepulse has been carefully considered. Substrates exposed to the ASE show no evidence, under microscopic examination, of a tightly focusable (~ 10 - μ m-diameter) component. Only the larger ($\sim 8 \times 10^{-2}$ cm²) pattern can be made visible on suitably absorbing materials. These tests were performed with the beam blocked at the input to the amplifier chain. Also, theoretical estimates of the maximum focusable intensity that arises from the ASE are found to be well below damage thresholds^{9,10} for the target materials used. Since the mechanisms of absorption in these materials at 248 nm are a multiphoton process, the minimum intensity required to induce significant absorption^{9,10} is in the range of 10^{10} – 10^{11} W/cm². All the available experimental evidence and analysis indicate that no prepulse plasma was formed in these

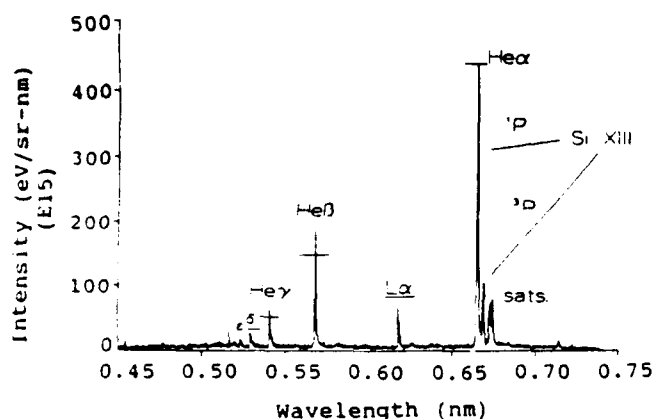


Fig. 1. X-ray spectrum from a SiO_2 target showing transitions from highly ionized Si ions. The main features originating from He-like Si XIII and H-like Si XIV ions are identified. Sats. indicates the position of satellite lines identified with Si XII ions. The horizontal bars indicated on the spectrum corresponding to the He- α , L- α , He- β , He- γ , and He- δ transitions designate the LASNEX calculated intensities of these lines. These calculated results are shown normalized to the He- α feature.

experiments. Therefore these materials and the plasmas produced therefrom should not be affected by the laser prepulse present in these studies.

The expected absence of a prepulse plasma was experimentally verified. This was achieved by using only the ASE to irradiate comparatively a MgF_2 target and a multilayer target (100-nm Ni on a 5-mm-thick MgF_2 substrate). When the ASE was focused onto the bare MgF_2 target, no visible breakdown was observed, and no surface damage was evident. When the multilayer Ni target, with the Ni side facing the laser, was irradiated with the ASE, breakdown was observed as well as surface damage on the Ni. After reversal of the target so that the uncoated MgF_2 surface faced the laser, a plasma was again observed on the Ni side of the target, with no observable plasma formed on or damage to the front MgF_2 surface. In this latter configuration the energy was freely transmitted to the rear surface. Therefore it is concluded that the use of properly selected ultraviolet-transmitting materials was effective in eliminating the unwanted influence of the nanosecond prepulse present in this research.

The x-ray emission from all targets was collected by flat potassium hydrogen phthalate ($2d = 2.66$ nm) and pentaerythritol ($2d = 0.87$ nm) crystal spectrometers and recorded on DEF film. The spectrometers contained filters composed of two 100-nm layers of Al on a 2- μm -thick polycarbonate substrate for shielding the DEF film from unwanted radiation. Approximately 25 shots were accumulated for each spectrum. Portions of the spectra obtained from a SiO_2 target are shown in Fig. 1. Also shown in Fig. 1 are the calculated line intensities for the He- α , L- α , He- β , He- γ , and He- δ transitions from ionized Si. The ratio of line strengths, normalized to the He- α feature, are seen to agree within approximately 20%. For MgF_2 and SiO_2 targets, both He-like and H-like emissions were identified from Mg and Si ions. For the CaF_2

target, only the $1s^2$ - $1s2p$ line emitted by He-like Ca ions was found. The absolute line intensities were deduced from known data for the film calibration,¹¹ the filter, and the response of the crystal spectrometer.¹²

The LASNEX code was used to simulate the experiment at $3 \times 10^{16} \text{ W/cm}^2$, assuming a 30% absorption by the target material, a value that is comparable with the absorption measured in Ref. 4. The treatment incorporates flux-limited thermal conduction (with the thermal flux limited to its free-streaming value times a coefficient f , taken to be 0.1), hydrodynamic expansion, and a nonlocal thermodynamic equilibrium solution⁷ to the atomic rate equations in the context of a hydrogenic atomic model. The choice of $f = 0.1$ is based on previous findings of its suitability for Fokker-Planck heat transport simulations.¹³ Furthermore, the results are not sensitive to the magnitude of the flux limiter (f); the use of $f = 0.2$ in the calculations changes the outcome by less than 20%. Figure 2 exhibits the calculated development of both the electron temperature T_e and the electron density n_e for a Mg plasma produced by a KrF* laser intensity of $3 \times 10^{16} \text{ W/cm}^2$ at the time of peak laser irradiation [Fig. 2(a)] and 1 ps after the peak laser intensity [Fig. 2(b)]. As shown, a high-density hot plasma is formed initially at the surface. After rapid expansion, a hot subcritical corona is produced. Thermal conduction inward creates a fairly hot, solid-density region of nearly fully ionized Mg and F. Based on the simulated density and temperature profile, the absolute line intensities were calculated for $1s^2$ - $1s3p$, $1s^2$ - $1s2p$ He-like, and $1s$ - $2p$ H-like transitions of Mg and Si ions. These calculations were compared with the experimental values obtained from the DEF film and found to be in agreement to better than a factor of 2. Furthermore, for MgF_2 targets subjected to an intensity of $\approx 3 \times 10^{16} \text{ W/cm}^2$, the simulation indicates that a plasma with an electron temperature of the order of 500 eV at a solid density is produced.

In conclusion, when a subpicosecond KrF* laser system is used to irradiate a high-damage-threshold ultraviolet-transmitting target, the formation of a prepulse plasma is prevented. This allows the high-intensity laser energy to create solid-density hot material. It should be noted that this technique substantially relaxes the requirement for the contrast ratio of the ASE and pulse intensities for high-power short-pulse laser systems.

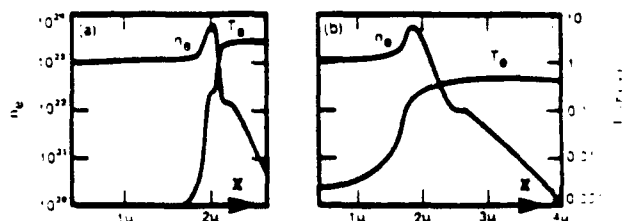


Fig. 2. LASNEX simulation indicating the electron temperature and density established (a) at the time of peak intensity of irradiation and (b) 1 ps after the peak value of irradiation.

The authors gratefully acknowledge discussions with G. Gibson and the technical contributions of K. Hudson and D. Newman of Sachs-Freeman Associates, Inc., and of P. Noel and J. Wright. Support for this research was provided by the U.S. Air Force Office of Scientific Research, the U.S. Office of Naval Research, and the Strategic Defense Initiative Organization. The research of M. D. Rosen was performed under the auspices of the U.S. Department of Energy by the Lawrence Livermore National Laboratory under contract W-7405-ENG-48.

References

1. M. M. Murnane, H. C. Kapteyn, and R. W. Falcone, *Phys. Rev. Lett.* **62**, 155 (1989).
2. H. M. Milchberg, R. R. Freeman, S. C. Davey, and R. M. More, *Phys. Rev. Lett.* **61**, 2364 (1988).
3. J. C. Kieffer, P. Audebert, M. Chaker, J. P. Matte, H. Pèpin, T. W. Johnston, P. Maine, D. Meyerhofer, J. Delettrez, D. Strickland, P. Bado, and G. Mourou, *Phys. Rev. Lett.* **62**, 760 (1989).
4. R. Fedosejevs, R. Ottmann, R. Sigel, G. Kühnle, S. Szatmári, and F. P. Schäfer, *Phys. Rev. Lett.* **64**, 1250 (1990).
5. J. A. Cobble, G. A. Kyrala, A. A. Hauer, A. J. Taylor, C. C. Gomez, N. D. Delamater, and G. T. Schappert, *Phys. Rev.* **39**, 454 (1989).
6. C. H. Nam, W. Tighe, E. Valeo, and S. Suckewer, *Appl. Phys. B* **50**, 275 (1990).
7. G. B. Zimmerman and W. L. Kruer, *Commun. Plasma Phys.* **11**, 51 (1975), and references therein.
8. T. S. Luk, A. McPherson, G. Gibson, K. Boyer, and C. K. Rhodes, *Opt. Lett.* **14**, 1113 (1989).
9. A. J. Taylor, R. B. Gibson, and J. P. Roberts, *Opt. Lett.* **13**, 814 (1988).
10. P. Simon, H. Gerhardt, and S. Szatmári, *Opt. Lett.* **14**, 1207 (1989).
11. P. D. Rockett, C. R. Bird, C. J. Hailey, D. Sullivan, D. B. Brown, and P. G. Burkhalter, *Appl. Opt.* **24**, 2536 (1985).
12. D. B. Brown and M. Fatemi, *J. Appl. Phys.* **51**, 2540 (1980); J. W. Criss, *Appl. Spectrosc.* **33**, 19 (1979).
13. A. R. Bell, R. G. Evans, and D. J. Nicholas, *Phys. Rev. Lett.* **46**, 243 (1981).

Appendix D: "Studies of the Interaction of Molecules and Solids with Intense Sub-picosecond 248 nm Radiation"

STUDIES OF THE INTERACTION OF MOLECULES AND SOLIDS WITH INTENSE SUBPICOSECOND 248 nm RADIATION*

T. S. Luk, A. McPherson, B. E. Bouma, K. Boyer, and C. K. Rhodes

Laboratory for Atomic, Molecular, and Radiation Physics
Department of Physics, University of Illinois at Chicago
P. O. Box 4348, Chicago, Illinois 60680

ABSTRACT

Studies of the interaction of matter with high intensity radiation ($\geq 10^{16}$ W/cm²) are leading to the observation of coulomb explosions from highly excited molecules and intense x-ray emission from solid targets.

I. INTRODUCTION

Advances in femtosecond lasers are extending the exploration of multiphoton interactions well into the strong-field regime, the physical situation in which the external field is greater than an atomic unit (e/a_0). The performance projected for ultraviolet rare gas halogen technology is currently being realized¹⁻¹⁰ and new near-infrared solid state systems, such as Ti:Al₂O₃, are under vigorous development. Both technologies¹¹ should reach a field strength of $\sim 100 e/a_0$ with instruments that produce an output energy of ~ 1 J.

There is a growing body of evidence that fundamentally new forms of highly excited matter can be produced with strong-field interactions. Specifically, there is considerable interest in (1) mechanisms leading to high levels of electronic excitation, particularly those involving ionization and the excitation of inner-shell states, and (2) the properties of matter which govern the generation of intense short wavelength radiation.¹

II. EXPERIMENTAL CONSIDERATIONS

The KrF* (248 nm) source used for the studies discussed herein has been described elsewhere.^{8,10} This instrument currently has an output pulse width of =

* ~~To be~~ published in the Proceedings of the International Conference on Multiphoton Processes (ICOMP V, Saclay, 1991).

600 fs, a typical pulse energy in the 300–400 mJ range, and focusability nominally within a factor of two of the diffraction limit.⁸ For example, with a simple $f/10$ CaF_2 lens, peak intensities of $\sim 3 \times 10^{16} \text{ W/cm}^2$ are produced even though such a lens exhibits appreciable spherical aberration. The application of more sophisticated focusing systems can clearly generate substantially greater field strengths.^{8,9}

A recent modification has incorporated a $\text{Ti:Al}_2\text{O}_3$ amplifier into the system for amplification of the radiation at 745 nm. This change has resulted in approximately a 40-fold increase in the 248 nm output energy from the mixing crystal to a value of $\sim 40 \mu\text{J}$. This enables the generation of a significantly more intense seed beam to drive the power amplifier and a reduction of the intensity of the amplified spontaneous emission.

A more detailed characterization of the pulse shape¹² for this system is becoming available with the use of a technique involving a third order intensity correlation¹³. One of the properties is a clearly observed asymmetry in the profile of the pulses, in our case, a waveform rising more rapidly than it falls. The current seed beam generates pulses with a width as short as ~ 260 fs.

The ability to concentrate the pulse energy in a small focal zone is another crucial property necessary for the generation of high field strengths. With an $f/7$ focusing system, focal zones with a diameter of $\sim 6.6 \mu\text{m}$ have been measured, a dimension which corresponds to a value of ~ 1.5 -fold the diffraction limit.

III. STUDIES OF MOLECULAR ION PRODUCTION

Studies of collision-free ionization have been a valuable source of information on multiphoton processes.^{14–17} Although most studies have been conducted with atoms, recent work has begun to examine molecules, including certain polyatomic systems. Indeed, studies of molecular ionization have produced valuable new insights into the dynamics of multiphoton processes.^{18–26} Energetic coulomb explosions have been studied in which (1) the fragments have kinetic energies of several tens of eV per particle. (2) evidence for molecular inner-shell excitation has been

observed,²⁶ and (3) molecular atomic site-dependent energy deposition has been detected.²⁷

A. N_2

It is possible to measure the kinetic energy distributions of the products arising from a molecular coulomb explosion with an appropriately arranged time-of-flight apparatus.²² N^{q+} ionic fragments produced with a peak intensity of $\sim 3 \times 10^{16} \text{ W/cm}^2$ are observed with charges in the range $1 \leq q \leq 5$. The fragment distributions generally fall off at sufficiently high ion energy and commonly exhibit observable structure. If we take the energy at which the distribution falls to one half its maximum value as an approximate measure of the characteristic kinetic energy of a fragment, we can summarize the findings on N_2 as shown in Fig. (1).

The coulomb energy associated with the production of N^{3+} fragments at $\sim 38 \text{ eV}$ implies, given the equilibrium internuclear²⁸ separation of N_2 as $r_0 = 1.1 \text{ \AA}$, the generation of a nascent ionized molecule of the form N_2^{q+} with $q \geq 5$. This

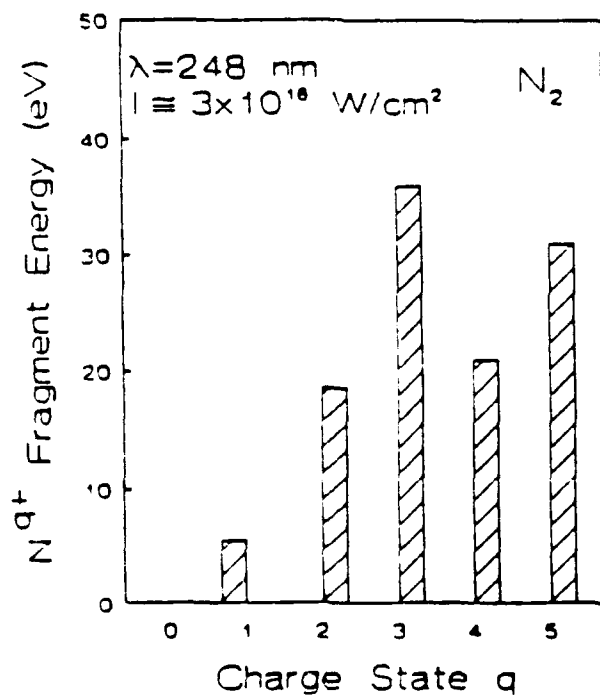


Fig. (1): Summary of fragment energies observed in N_2 .

indicates that during the course of the interaction the ionization must proceed quite rapidly to at least this stage. This finding is in general concurrence with conclusions on the rate of energy transfer stemming from earlier studies.²² The minimum energy required to produce N_2^{5+} , assuming an initial internuclear separation of $\sim r_0$, is ~ 224 eV.

B. Comparison of CO and CO₂

The comparison of the carbon and oxygen fragments observed from CO and CO₂ are providing further information on strong-field coupling to molecules. In considering the data shown below for C⁴⁺ fragments in Fig. (2), it should be understood that the shapes of the time-of-flight ion signals are determined by both the instrumental response and the kinetic energies of the fragments. The individual ion signals are actually composed of two components which become resolved at sufficiently high particle energy. One component arises from ions initially formed with velocities parallel to the time-of-flight direction while the

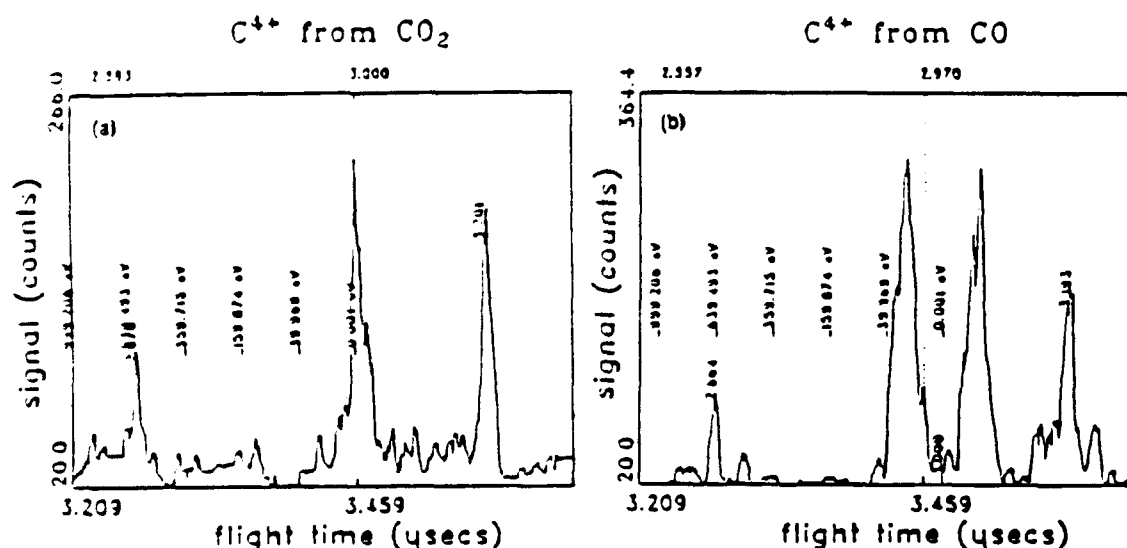


Fig. (2): Ion time-of-flight spectra for C⁴⁺: (a) Ions produced from CO₂ appear at low energy; (b) Ions produced from CO show two well resolved peaks with a maximum kinetic energy ~ 40 eV.

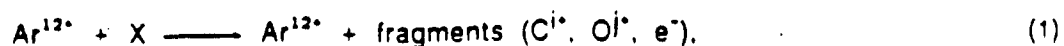
other arises from ions whose initial velocity is anti-parallel to that vector. The greater the separation of these two peaks, the greater is the energy associated with the kinetic energy of the fragments. The two peaks are of comparable height and width for appropriate settings of the extraction and acceleration voltages used in the time-of-flight apparatus.^{20,22}

The time-of-flight data for C⁺⁺ observed from CO₂ are shown in Fig. (2a). In this case, only one peak is seen, a clear sign that the particles are slow. This conforms to the expectation that the carbon atom in the center of the molecule would develop, in the process of fragmentation, a relatively small kinetic energy as a result of the opposing forces from the oxygen atoms on either side.^{25,29}

The corresponding data for C⁺⁺ fragments produced from CO are illustrated in Fig. (2b). These data clearly exhibit two well resolved peaks indicating that a substantial kinetic energy is present. The maximum kinetic energy observed in this case is approximately 40 eV. Basically, in the comparison of CO₂ and CO, the carbon ions are produced with a low kinetic energy from the former and a high kinetic energy from the latter.

The characteristics of the oxygen ions produced represent a rather different pattern. The situation can be illustrated by consideration of the observed kinetic energy spectra for O³⁺ which are shown in Fig. (3). In this case both molecules produce energetic ions, but those arising from CO₂ are significantly more energetic. Comparison of Fig. (2b) and Fig. (3b) indicates that the maximum energies of the C⁺⁺ and O³⁺ ions are roughly comparable when produced from CO. This is not surprising, since the molecule is nearly symmetric and the two charge states differ modestly.

Comparison of these results for the C⁺⁺ and O³⁺ ions with extant data on ion-molecule collisions is informative. The collisional process that was studied²⁹ involved



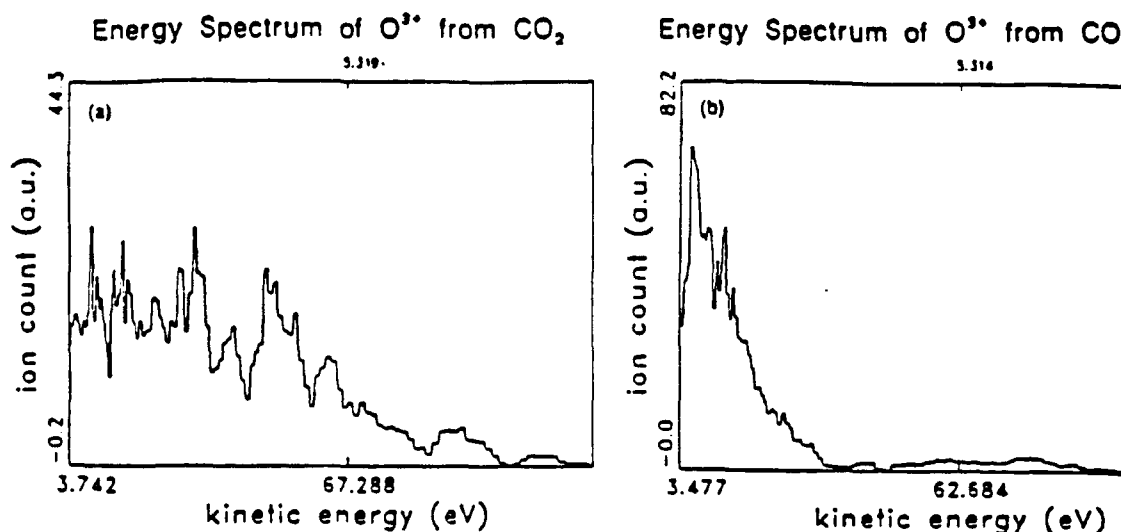


Fig. (3): Kinetic energy spectra for O^{3+} : (a) Ions produced from CO_2 show a maximum energy ~ 70 eV; (b) Ions produced from CO exhibit a maximum energy of ~ 30 eV.

with X denoting CO and CO_2 . The collision energy corresponded to ~ 1 MeV/au so that the time of interaction is sufficiently small that negligible nuclear motion will occur in the molecular frame. The resulting coulomb explosion commences from an intact ionized molecule in a spatial configuration determined by the neutral target molecule.

The collisional data²⁹ of Matsuo et al. for carbon and oxygen ions produced from CO and CO_2 are shown in Fig. (4). Also indicated for comparison with their data are the maximum kinetic energies of the C^{2+} and O^{3+} ions observed in the multiphoton studies. In all cases, the multiphoton results correspond rather closely to the values produced by the ion-molecule interaction. This similarity in outcome leads to the conclusion that the nature of the molecular ion which undergoes the coulomb explosion is essentially the same in both cases. Specifically, we conclude that the strong-field interaction has many features in common with ion-atom and ion-molecule collisions. The nature of this analogy has been explored previously in other work.^{30,31}

IV. X-RAY GENERATION FROM SOLID TARGETS

Solid materials offer the possibility of combining a high particle density with a very high level of electronic excitation, if the deposition of energy in the solid can be made to occur sufficiently rapidly. High brightness subpicosecond light sources²⁻¹⁰ now enable such rapid excitation to be achieved.

Consider a slab of unit area with density ρ and thickness δ which, upon excitation with intense subpicosecond radiation, produces radiation in the kilovolt spectral range. In order to set the scale, we want to obtain a simple upper bound on the x-ray intensity. Since the time of excitation is short, as a first approximation, we will ignore the hydrodynamical expansion, a process which will occur roughly at a rate of $\sim 1-10 \text{ \AA/fs}$. An upper limit on the x-ray intensity I_{xm} can then be simply written as

$$I_{xm} \sim \frac{\hbar\omega_x \rho \delta}{2\tau_x} \quad (2)$$

in which $\hbar\omega_x$ represents a kilovolt quantum and τ_x is the effective radiative rate of the excited material. For the present discussion, we will set ρ as solid density ($\sim 5 \times 10^{22} \text{ cm}^{-3}$) and take as the lower limit for τ_x a typical radiative rate for kilovolt transitions. For the latter will use the range³² $2 \times 10^{-14} \leq \tau_x \leq 10^{-13} \text{ s}$ as a rough measure. If we take for δ the recently measured value³³ of the depth of energy penetration of $\sim 250 \text{ nm}$ for $\text{MgF}_2/\text{SiO}_2$ targets irradiated with 248 nm at an intensity of $\sim 3 \times 10^{16} \text{ W/cm}^2$, Eq. (2) can be evaluated. With these parameters we find $10^{15} \leq I_{xm} \leq 5 \times 10^{15} \text{ W/cm}^2$. This simple upper limit on I_{xm} can now be compared to the experimental result.³⁴

An experimental concern in studies of the interaction of intense radiation with solid matter is the influence of any low intensity prepulse on the true state of the irradiated system. It has been experimentally found³³ that the interference of the prepulse can be entirely eliminated at 248 nm by the use of a target composed of ultraviolet transmitting materials. For example, MgF_2 and BaF_2

exhibit essentially no absorption up to relatively high intensities and studies have demonstrated that these values are sufficiently high to prevent any significant influence by the prepulse. This enables the intense subpicosecond energy to couple directly to virgin solid matter.^{33,34}

The KrF^* system used in this experiment delivered a subpicosecond pulse energy of ~ 150 mJ. The prepulse had a duration of ~ 20 ns, an energy of ~ 10 mJ, and is known to be very poorly focusable.⁸ The radiation was focused onto a flat rotating BaF_2 target with a $f/10$ CaF_2 lens. The peak laser intensity achievable on target was estimated to be $\sim 3 \times 10^{16}$ W/cm², based on previous threshold ionization intensity measurements at low density³⁵ as well as recent direct imaging of the focal zone. The x-ray emission from the target was collected by flat KAP ($2d=26.6\text{\AA}$) and PET ($2d=8.7\text{\AA}$) crystal spectrometers and recorded on DEF film. For higher resolution, a convex KAP crystal spectrometer was used. Approximately 10 shots were accumulated for each spectrum.

The spectrum observed from BaF_2 exhibited strong emission in the 9–13 \AA range. In addition to the spectrum, calibration of the film revealed that ~ 6 mJ of x-rays were produced on each shot. Subsequent pinhole camera measurements of the x-ray emission from solid targets ($\text{MgF}_2/\text{SiO}_2$) indicated a radiating spot size with a diameter in the range of 8–9 μm . This value is quite close to the independently measured focal diameter of the optical system. Finally, calculations³⁴ estimate that the radiation occurs over a time of ~ 1 ps, a value that is consistent with the x-ray pinhole camera measurements. Therefore, assuming isotropic emission from a volume of these dimensions, the experimentally radiated intensity I_r was approximately $I_r \sim 2\text{--}3 \times 10^{15}$ W/cm². We see immediately that this value falls in the range given by the estimate of the upper bound I_{xm} . The measured performance, therefore, appears close to the maximum possible. Although such a source is incoherent, a radiation rate of this magnitude, coupled with the relatively narrow spectrum over which it occurs, constitutes a source of extremely high

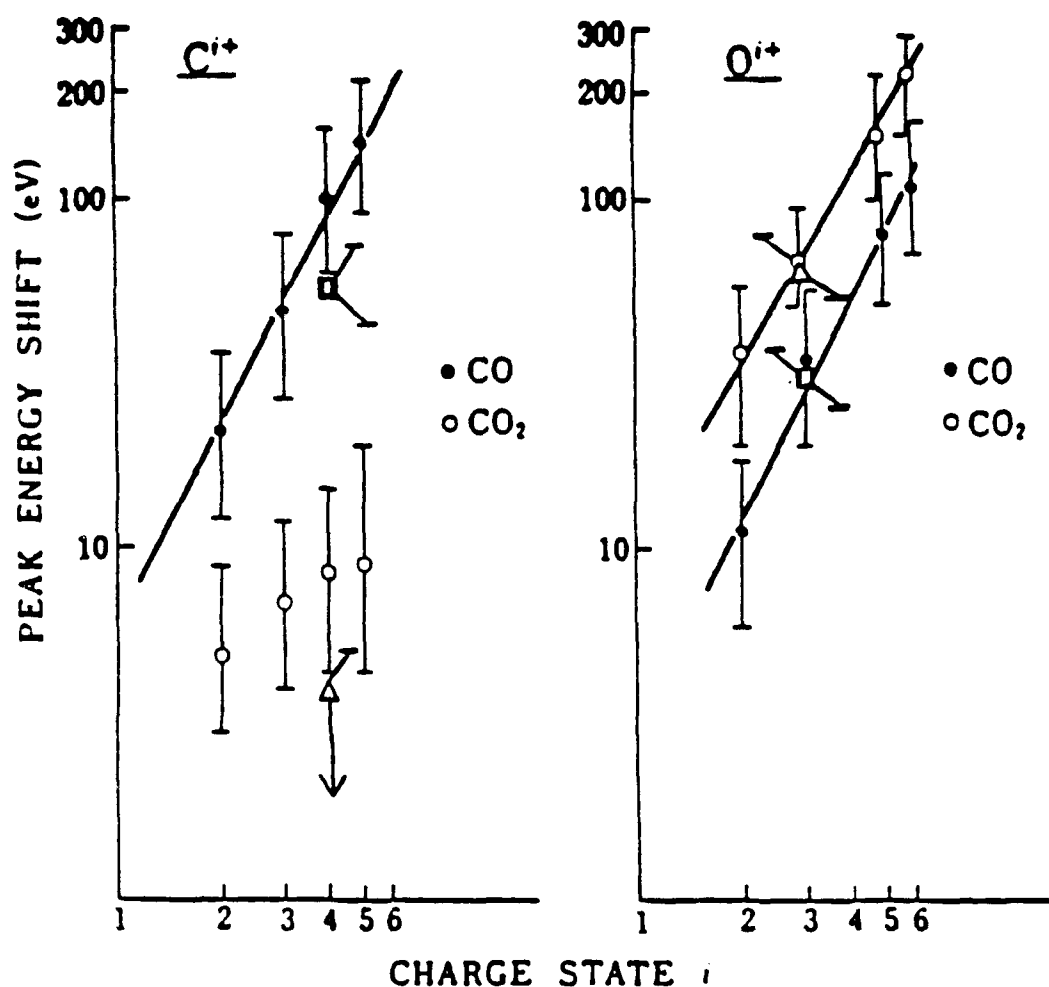


Fig. (4): The data of Ref. (29) on carbon and oxygen ions produced in Ar^{12+} ion-molecule collisions in the reaction $Ar^{12+} + X \rightarrow Ar^{12+} + \text{fragments}$ (C^{i+} , O^{i+} , e^-) at a collision energy of ~ 1 MeV/au. The multiphoton data for C^{2+} and O^{3+} are also shown for comparison for CO₂ (Δ) and CO (\square). Rather close agreement of the collisional and multiphoton data is seen. Figure reproduced with permission.

spectral brightness that can produce unusually high excitation rates in absorbing material.

IV. SUMMARY AND CONCLUSIONS

The use of recently developed high brightness subpicosecond light sources for the study of the interaction of matter with strong electromagnetic fields is leading to the observation of new phenomena and new classes of excited states of matter. Two important consequences of these developments are the production of new forms of ionized molecular matter and the generation of powerful x-ray sources associated with high density plasma environments.

V. ACKNOWLEDGEMENTS

The technical assistance of P. Noel and J. Wright and helpful discussions with J. C. Solem, and G. N. Gibson are acknowledged. The fruitful and congenial participation of A. Zigler, P. G. Burkhalter, D. J. Nagel, and M. D. Rosen in the studies of solid materials is warmly acknowledged. Support for this research was provided by the U. S. Air Office of Scientific Research, the U. S. Office of Naval Research, and the Strategic Defense Initiative Organization.

VI. REFERENCES

1. C. K. Rhodes, *Science* **229**, 1345 (1985).
2. S. Szatmári, F. P. Schäfer, E. Müller-Horsche, and W. Mückenheim, *Opt. Comm.* **63**, 305 (1987).
3. A. Endoh, M. Watanabe, N. Sarukura, and S. Watanabe, *Opt. Lett.* **7**, 353 (1989).
4. J. R. M. Barr, N. J. Overall, C. J. Hooker, I. N. Ross, M. J. Shaw, W. T. Toner, *Opt. Comm.* **66**, 127 (1988).
5. J. G. Glowina, J. Misevich, and P. P. Sorokin, *J. Opt. Soc. Am.* **B4**, 1061 (1987).
6. A. P. Schwarzenbach, T. S. Luk, I. A. McIntyre, U. Johann, A. McPherson, K. Boyer, and C. K. Rhodes, *Opt. Lett.* **11**, 499 (1986).
7. J. P. Roberts, A. I. Taylor, P. H. Y. Lee, and R. B. Gibson, *Opt. Lett.* **13**, 734 (1988).
8. T. S. Luk, A. McPherson, G. Gibson, K. Boyer, and C. K. Rhodes, *Opt. Lett.* **14**, 1113 (1989).
9. A. J. Taylor, C. R. Tallman, J. P. Roberts, C. S. Lester, T. R. Gosnell, P. H. Lee, and G. A. Kyrala, *Opt. Lett.* **15**, 39 (1990); A. J. Taylor, T. R. Gosnell, and J. P. Roberts, *Opt. Lett.* **15**, 118 (1990).
10. I. A. McIntyre, and C. K. Rhodes, *J. Appl. Phys.*, to be published.
11. T. S. Luk, private communication.
12. B. Bouma, private communication.
13. H. Schulz, H. Schüler, T. Engers, and D. von der Linde, *IEEE J. Quantum Electron.* **25**, 2580 (1990).
14. A. L'Huillier, L.-A. Lompré, G. Mainfray, and C. Manus, *Phys. Rev. Lett.* **48**, 1814 (1982).
15. A. L'Huillier, L.-A. Lompré, G. Mainfray, and C. Manus, *Phys. Rev. A* **27**, 2503 (1983).

16. T. S. Luk, H. Pummer, K. Boyer, M. Shahidi, H. Egger, and C. K. Rhodes, *Phys. Rev. Lett.* 51, 110 (1983).
17. T. S. Luk, U. Johann, H. Egger, H. Pummer, and C. K. Rhodes, *Phys. Rev. A* 32, 214 (1985).
18. J. Frasinski, K. Codling, P. Hatherly, J. Barr, I. N. Ross, and W. T. Toner, *Phys. Rev. Lett.* 58, 2424 (1987).
19. K. Codling, L. J. Frasinski, P. Hatherly, and J. R. M. Barr, *J. Phys. B* 20, L525 (1987).
20. T. S. Luk and C. K. Rhodes, *Phys. Rev. A* 38, 6180 (1988).
21. K. Codling, L. J. Frasinski, and P. A. Hatherly, *J. Phys. B* 22, L321 (1989).
22. K. Boyer, T. S. Luk, J. C. Solem, and C. K. Rhodes, *Phys. Rev. A* 39, 1186 (1989).
23. P. A. Hatherly, L. J. Frasinski, K. Codling, A. J. Langley, and W. Shaikh, *J. Phys. B* 23, L291 (1990).
24. P. H. Bucksbaum, A. Zavriyev, H. G. Muller, and D. W. Schumacher, *Phys. Rev. Lett.* 64, 1883 (1990).
25. L. J. Frasinski, K. Codling, and P. A. Hatherly, *Science* 246, 1029 (1989).
26. G. Gibson, T. S. Luk, A. McPherson, K. Boyer, and C. K. Rhodes, *Phys. Rev. A* 40, 2378 (1989).
27. T. S. Luk, A. McPherson, G. N. Gibson, K. Boyer, and C. K. Rhodes, to be published in the Proceedings of SWLA - 90 International Symposium, "Short Wavelength Lasers and Their Applications," Samarcand, USSR, May 14-18, 1990.
28. K. P. Huber and G. Herzberg, Molecular Spectra and Molecular Structure. IV, Constants of Diatomic Molecules (Van Nostrand Reinhold, Co., New York, 1979).
29. T. Matsuo, T. Tonuma, M. Kase, T. Kambara, H. Kumagai, and H. Tawara, *Chem. Phys.* 121, 93 (1988).
30. K. Boyer and C. K. Rhodes, *Phys. Rev. Lett.* 54, 1490 (1985).
31. K. Boyer, G. Gibson, H. Jara, T. S. Luk, I. A. McIntyre, A. McPherson, R. Rosman, J. C. Solem, and C. K. Rhodes, *IEEE Trans. Plasma Sci.* PS-16, 541 (1988).
32. J. H. Scofield, in Atomic Inner-Shell Processes, Vol. I, edited by Bernd Crasemann (Academic Press, New York, 1975), p. 265.
33. A. Ziegler, P. G. Burkhalter, D. J. Nagel, G. N. Gibson, T. S. Luk, A. McPherson, C. K. Rhodes, and M. D. Rosen, manuscript in preparation.
34. A. Ziegler, P. G. Burkhalter, D. J. Nagel, T. S. Luk, A. McPherson, C. K. Rhodes, and M. D. Rosen, manuscript in preparation.
35. G. Gibson, T. S. Luk, and C. K. Rhodes, *Phys. Rev. A* 41, 5049 (1990).

Appendix E: "Stable Channeled Propagation of Intense Radiation in Plasma Arising from Relativistic and Charge-Displacement Mechanisms"

**STABLE CHANNELED PROPAGATION OF INTENSE OPTICAL PULSES
IN PLASMAS ARISING FROM
RELATIVISTIC AND CHARGE-DISPLACEMENT MECHANISMS**

A. B. Borisov[†], A. V. Borovskiy^{*}, V. V. Korobkin[^],
A. M. Prokhorov^{*}, O. B. Shiryayev[†], J. C. Solem^{††},
K. Boyer^{††}, and C. K. Rhodes^{††}

[†] Laboratory for Computer Simulation, Research Computer Center, Moscow State University, Moscow, 119899, Russia

^{*} General Physics Institute, Academy of Sciences of Russia, Moscow, 117942, Russia

^{††} Department of Physics, University of Illinois at Chicago, Chicago, IL 60680, USA. [(312) 996-4868, FAX# (312) 996-8824]

[^] Theoretical Division, Los Alamos National Laboratory, Los Alamos, NM 87545, USA.

ABSTRACT

Dynamical calculations of propagating intense axisymmetric circularly polarized laser pulses in collisionless plasmas, incorporating relativistic and charge-displacement mechanisms, show that their combined action can lead to stabilized confined modes of propagation. The effect of the charge-displacement is large and cavitation of the electron distribution is a general feature. An example shows that ~ 50% of the incident power (~ 4 TW) can be trapped in a channel which, for a wavelength of 248 nm, an electron density of ~ $7.5 \times 10^{20} \text{ cm}^{-3}$, and an initial beam radius of ~ 3 μm , develops propagating intensities of ~ 10^{21} W/cm^2 .

The dynamics of propagation of intense subpicosecond laser pulses in plasmas in the strongly relativistic regime is currently undergoing vigorous theoretical analysis¹⁻¹⁰. Of primary significance is the possible formation of quasistable self-channeled modes of propagation. In this Letter we examine theoretically the consequences of the combined action of relativistic and charge-displacement mechanisms with particular attention to the development and character of highly stable confined modes of propagation. It is assumed that the pulse duration τ considered in this treatment satisfies the inequality $\tau_i \gg \tau \gg \tau_e$, with τ_i and τ_e designating the response times of the ions and electrons, respectively, so that ion displacement can be neglected. For radiation with a wavelength of 248 nm, the range of intensity of principal interest is $I \gtrsim 10^{19}$ W/cm², since both relativistic and charge-displacement mechanisms are very significant in that region. Additional experimental studies concerning this matter are presented in Ref. (11).

The basic formalism and procedures describing calculations have been described previously.⁶ Assuming collisionless and lossless propagation, the slowly varying complex field amplitude $E(t,z,r)$ is governed by the nonlinear Schrödinger equation [3, 6-8]

$$\left(\frac{1}{c_1} \frac{\partial}{\partial t} + \frac{\partial}{\partial z} \right) E + \frac{i}{2k} [\Delta_{\perp} E + k_p^2 (1 - \gamma^{-1} N_e) E] = 0, \quad (1)$$

$$N_e = \max(0, f(r) + k_p^{-2} \Delta_{\perp} \gamma), \quad \gamma = (1 + I/I_r)^{1/2}. \quad (2)$$

Here $\Delta_{\perp} = \partial^2/\partial r^2 + r^{-1}\partial/\partial r$ (r is the transverse coordinate), c_1 is the group velocity in the plasma, k is the wave number, $k^2 = k_0^2 - k_p^2$, $k_0 = \omega/c$, $k_p = \omega_{p,0}/c$, ω is the laser angular frequency, $\omega_{p,0}$ is the plasma frequency, c is the vacuum speed of light. N_e denotes the electron density N normalized by the peak value of the initial (unperturbed) electron density distribution N_0 ; $f(r)$ denotes the initial transverse distribution of N_e . $I = (c/4\pi) |E|^2$ is the intensity of laser

beam, $I_r = m_{e,0}^2 \omega^2 c^3 / 4\pi e^2$ is the parameter called the relativistic intensity. The term $k_p^{-2} \Delta_\perp Y$ in (2) describes the charge-displacement process.

The ponderomotive force is capable of completely expelling electrons from certain spatial regions, a condition described as "electronic cavitation".³ The calculations show that the charge-displacement plays a strong role in determining the spatial character of the propagating energy and, particularly, in stabilizing the confined high-intensity modes.

The essential finding of these calculations is insight into the formation and stabilization of spatially confined modes of propagation arising from the coöperative action of the relativistic and charge-displacement processes. The numerical simulations were performed with model pulses having Gaussian or hyper-Gaussian incident transverse intensity distributions interacting with initially homogeneous plasmas or plasma columns having a hyper-Gaussian radial profiles.

The results of computations presented in this work are given in the frame (q,z,r), $q = t - (z/c_1)$, connected with the wave front of the beam. The graphical data represented below illustrate the propagation of the radiation along the z-axis for $q = \text{constant}$. We present the results of simulations of dynamics of initially Gaussian beams for the following values of the parameters: $\lambda = 248 \text{ nm}$, $I_r = 1.34 \times 10^{20} \text{ W/cm}^2$, peak value of incident transverse intensity distribution $I_0 = 3 \times 10^{19} \text{ W/cm}^2$, initial beam radius $r_0 = 3 \text{ }\mu\text{m}$, $N_0 = 7.5 \times 10^{20} \text{ cm}^{-3}$, and $f(r) \equiv 1$ (initially uniform plasma). In this case, the ratio of the beam power P_0 to the critical power (P_{cr}) of relativistic and charge-displacement self-focusing⁸

$$P_{cr} = (m_{e,0}^2 c^3 / e^2) \left(\int_0^\infty g_0^2(\rho) \rho d\rho \right) (\omega / \omega_{p,0})^2$$

is 22.252. In the above expression, $g_0(\rho)$ is the so-called Townes mode.¹²

The solutions for the spatial profiles of the laser intensity [Fig. (1)] and the corresponding electron density [Fig. (2)] exhibit several important characteristics. Among them are (1) the generation of intense focal regions, (2) the development of a stable confined channel of high-intensity propagation, (3) the trapping of a substantial fraction of the incident power in the channel, and (4) strong cavitation of the electron density.

On the basis of the dynamical picture, the combined effect of the relativistic nonlinearity and the charge-displacement can be, in reasonable approximation, summarized in the following simple way. The relativistic effect leads to the initial concentration of the radiation and the resulting displacement of electronic charge reinforces this tendency and stabilizes the confinement. The coöperative nature of this action appears to lead to highly stable conditions of propagation.

The behavior of the computed solutions for large z can be compared with the z -independent eigenmodes⁸ of the nonlinear Schrödinger equation (1). The main result of this work is that the field amplitude tends asymptotically to the lowest eigenmode $V_s(r)$ of this equation. We call this phenomenon relativistic and charge-displacement self-channeling. $V_s(r)$ is a real-valued positive monotonic function of r , carries a real dimensionless index s , vanishes as $r \rightarrow \infty$, and is related to the electric field amplitude by the statement^{3,8}

$$E(r, z) = V_s(r) \exp[iz(s - 1)k_p^2(2k)^{-1}]. \quad (3)$$

Computations have shown, for the case studied, that the field distribution for large z tends to the amplitude $V_s(r)$ for the index $s \approx 0.554$. The appropriate intensity distribution is then given by $I_s(r) \approx V_s^2(r)$. Figure 3 exhibits the normalized asymptotic field amplitude $(I_s(r)/I_0)^{1/2}$ and the corresponding asymptotic electron density distribution $N_s(r)/N_0$. In the asymptotic distribution of intensity, 46% of the initial power of the beam is retained.

Several other cases have also been considered. In particular, calculations examining the dynamics of propagation have been studied for hyper-Gaussian initial intensity distributions for both homogeneous plasmas [$f(r) = 1$] and simulated plasma columns [$f(r) = \exp [-(r/r_0)^4]$]. The behavior was found to be qualitatively the same as that shown in Fig. (1) – Fig. (3) with asymptotically trapped fractions of the initial laser power ranging from 34% to 77%. Generally, studies of the relativistic/charge-displacement self-channeling thresholds showed that the only condition required for initially flat waveforms to propagate in this regime is $P_0 > P_{cr}$. Self-channeled propagation also develops in the cases involving initially focused and defocused beams. We note that the relativistic and charge-displacement self-channeling, characterized by the asymptotic evolution to the distributions given by the lowest stationary eigenmodes, described above, differs essentially from the previously known oscillatory regime arising from relativistic and charge-displacement mechanisms³ and the stabilization seen in purely relativistic propagation in plasma columns.⁶

In summary, the dynamical behavior of channeled propagation arising from both relativistic and charge-displacement mechanisms has been studied theoretically. Two principal findings have been established. (1) These two processes can coöperatively reinforce one another and lead to stable confined high-intensity modes of propagation in plasmas which are capable of trapping a substantial fraction ($\sim 50\%$) of the incident power. (2) The spatial profiles of both the intensities and electron density distributions tend asymptotically to those derived as lowest eigenmodes of a z -independent analysis.

The authors acknowledge fruitful conversations with A. R. Hinds, R. R. Goldstein, T. S. Luk, and A. McPherson. Support for this research was partially provided under contracts AFOSR-89-0159, (ONR) N00014-91-J-1106, (SDI/NRL) N00014-91-K-2013, (ARO) DAAL 3-91-G-0174, (DoE) DE-FG02-91ER12108, and (NSF) PHY-9021265.

REFERENCES

1. P. Sprangle, E. Esarey, and A. Ting, Phys. Rev. Lett. **64**, 2011 (1990); P. Sprangle, C. M. Tang, and E. Esarey, Phys. Rev. A **41**, 4663 (1990); A. Ting, E. Esarey, and P. Sprangle, Phys. Fluids **B2**, 1390 (1990).
2. G. Schmidt and W. Horton, Comments Plasma Phys. Controlled Fusion **9**, 85 (1985).
3. Gou-Zheng Sun, E. Ott, Y. C. Lee, and P. Guzdar, Phys. Fluids **30**, 526 (1987).
4. J. C. Solem, T. S. Luk, K. Boyer, and C. K. Rhodes, IEEE J. Quant. Electron. **25**, 2423 (1989).
5. T. Kurki-Suonio, P. J. Morrison, and T. Tajima, Phys. Rev. A **40**, 3230 (1989).
6. A. B. Borisov, A. V. Borovskiy, V. V. Korobkin, A. M. Prokhorov, C. K. Rhodes, and O. B. Shiryayev, Phys. Rev. Lett. **65**, 1753 (1990).
7. P. Sprangle, A. Zigler, and E. Esarey, Appl. Phys. Lett. **58**, 345 (1991).
8. A. B. Borisov, A. V. Borovskiy, V. V. Korobkin, A. M. Prokhorov, O. B. Shiryayev, and C. K. Rhodes, Laser Physics **1**, 103 (1991).
9. J. W. Bardsley, B. M. Penetrante, and M. H. Mittleman, Phys. Rev. A **40**, 3823 (1989).
10. A. B. Borisov, A. V. Borovskiy, O. B. Shiryayev, V. V. Korobkin, A. M. Prokhorov, J. C. Solem, T. S. Luk, K. Boyer, and C. K. Rhodes, Phys. Rev. A, to be published.
11. A. B. Borisov, A. V. Borovskiy, V. V. Korobkin, A. M. Prokhorov, O. B. Shiryayev, X. M. Shi, T. S. Luk, A. McPherson, J. C. Solem, K. Boyer, and C. K. Rhodes, Phys. Rev. Lett (submitted).
12. R. Y. Chiao, E. Garmire, and C. H. Townes, Phys. Rev. Lett. **13**, 479 (1964).

FIGURE CAPTIONS

- Fig. 1: The normalized intensity distribution $I(r,z)/I_0$. $I_0 = 3 \times 10^{19}$ W/cm², $r_0 = 3$ μ m, $\lambda = 248$ nm, and $N_0 = 7.5 \times 10^{20}$ cm⁻³.
- Fig. 2: The normalized electron density distribution $N(r,z)/N_0$ corresponding to the data shown in Fig. (1). $N_0 = 7.5 \times 10^{20}$ cm⁻³.
- Fig. 3: Radial dependence of the asymptotic solutions for the normalized amplitude $[I_S(r)/I_0]^{1/2}$ and the normalized electron density $N_S(r)/N_0$ for the index $s = 0.554$.

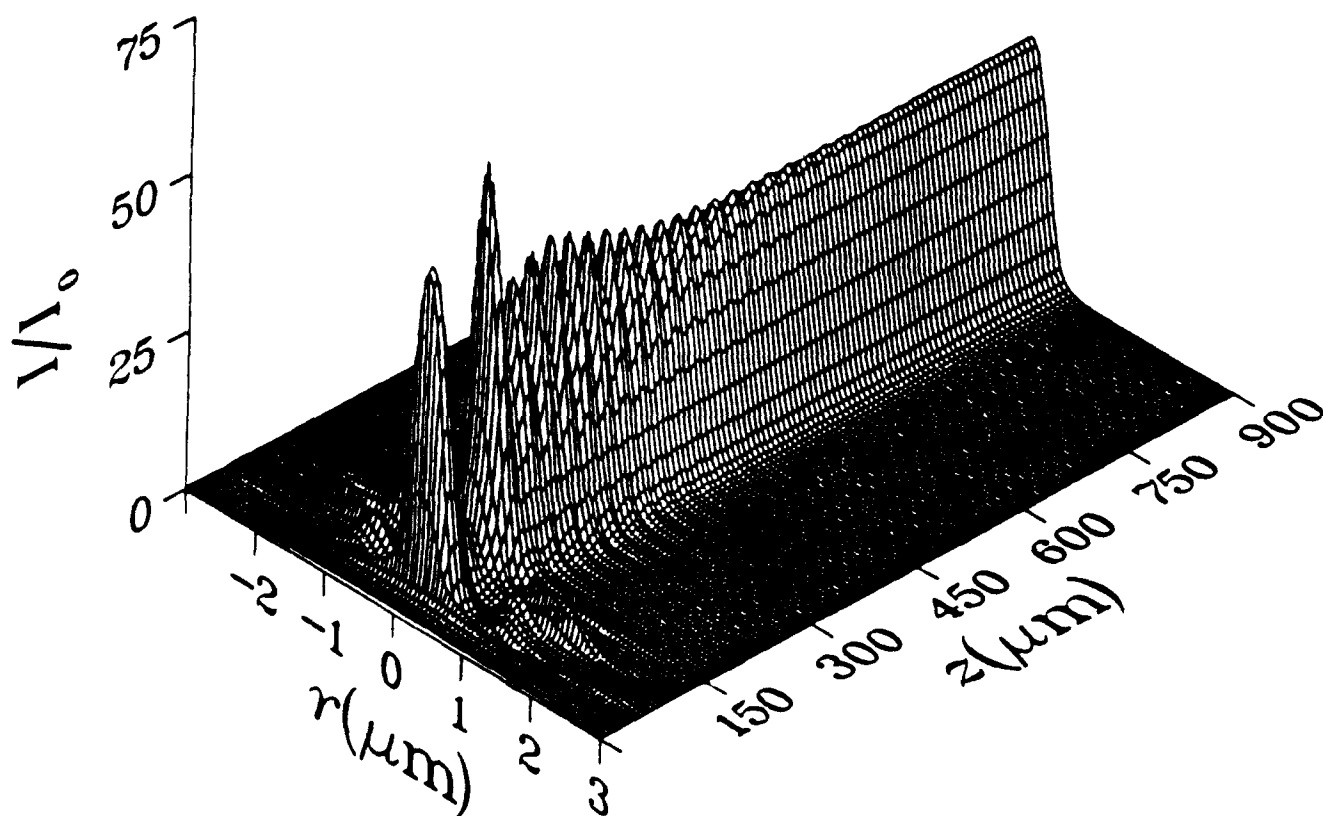


Figure 1

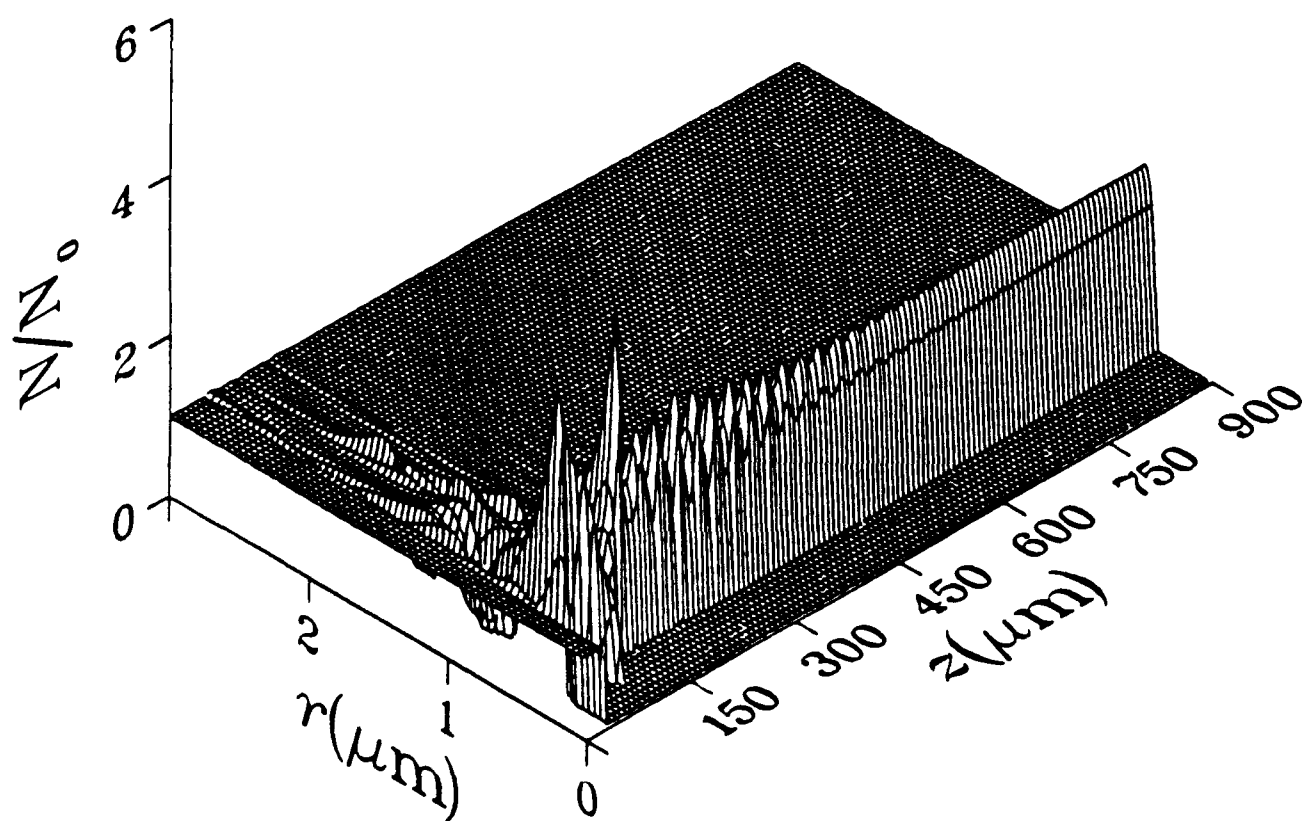


Figure 2

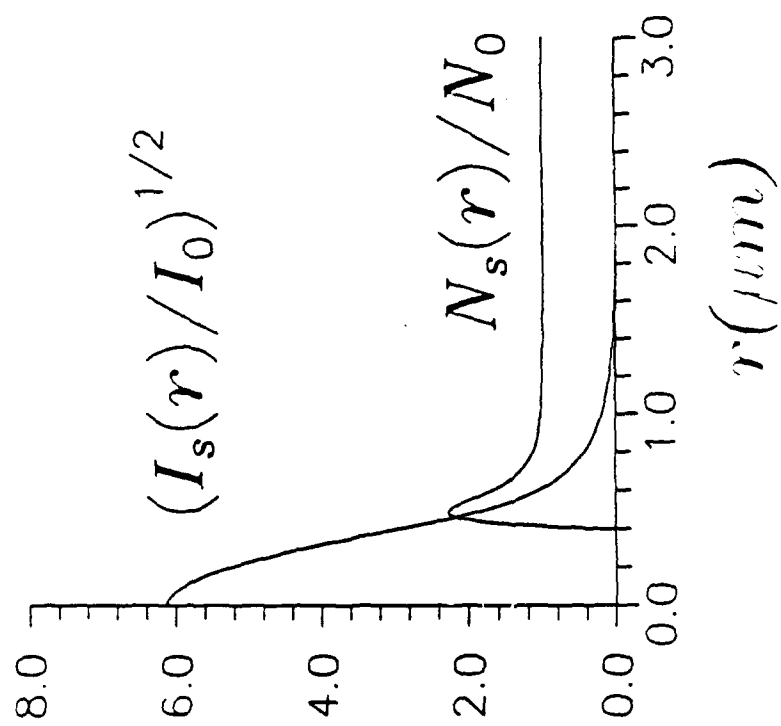


Figure 3

**Appendix F: "Observation of Relativistic and Charge-Displacement Self-Channeling
of Intense Subpicosecond Ultraviolet (248 nm) Radiation in Plasmas"**

Observation of Relativistic and Charge-Displacement Self-Channeling of Intense Subpicosecond Ultraviolet (248 nm) Radiation in Plasmas

A. B. Borisov,⁽¹⁾ A. V. Borovskiy,⁽²⁾ V. V. Korobkin,⁽²⁾ A. M. Prokhorov,⁽²⁾ O. B. Shiryaev,⁽¹⁾
X. M. Shi,⁽³⁾ T. S. Luk,⁽³⁾ A. McPherson,⁽³⁾ J. C. Solem,⁽⁴⁾ K. Boyer,⁽³⁾ and C. K. Rhodes⁽³⁾

⁽¹⁾Laboratory for Computer Simulation, Research Computer Center, Moscow State University, Moscow, 119899, Russia

⁽²⁾General Physics Institute, Academy of Sciences of Russia, Moscow, 117942, Russia

⁽³⁾Department of Physics, University of Illinois at Chicago, Chicago, Illinois 60680

⁽⁴⁾Theoretical Division, Los Alamos National Laboratory, Los Alamos, New Mexico 87545

(Received 13 November 1991)

Experimental studies examining a new relativistic regime of high-intensity short-pulse propagation in plasmas have been performed which present evidence for the formation of a stable mode of spatially confined (channeled) propagation. For an electron density of $\sim 1.35 \times 10^{21} \text{ cm}^{-3}$ and a power of $\sim 3 \times 10^{11} \text{ W}$, the results indicate a channel radius $< 1 \mu\text{m}$ and a peak intensity $\sim 10^{19} \text{ W/cm}^2$. Comparison of these findings with a dynamical theory yields agreement for both the longitudinal structure and the radial extent of the propagation observed.

PACS numbers: 52.40.Db, 42.25.-p, 42.65.Jx

A fundamentally new regime of electromagnetic propagation is expected to arise in plasmas for short-pulse radiation at sufficiently high intensity. Calculations of the propagation in plasmas, incorporating both relativistic [1,2] and charge-displacement mechanisms [3-7], indicate that the combined action of these processes can lead to a new stable form of spatially confined (channeled) propagation. This Letter (1) reports the results of the first experimental study probing the physical regime relevant to the observation of relativistic and charge-displacement self-channeling and (2) presents the initial comparison of these experimental findings with matching theoretical calculations performed with the computational procedures described in Ref. [7].

The experimental arrangement used in these studies is illustrated in Fig. 1(a). The source of radiation was a subpicosecond KrF* ($\lambda = 248 \text{ nm}$) laser that has been described elsewhere [8]. It delivered a linearly polarized power of $\sim 3 \times 10^{11} \text{ W}$ ($\sim 150 \text{ mJ}$, pulse duration $\sim 500 \text{ fs}$) in a beam with a diameter of $\sim 42 \text{ mm}$. When this radiation was focused into the chamber with lens $L1$ ($f/7$), a focal radius $r_0 \sim 3.5 \mu\text{m}$ was measured, giving a maximum intensity $I_0 \sim 8.6 \times 10^{17} \text{ W/cm}^2$. The medium was provided by filling the chamber statically with gas [He, Ne, Ar, Kr, Xe, N_2 , CO_2 , or a mixture of Xe (4%) and N_2 (96%)] up to a maximum density of $\sim 1.89 \times 10^{20} \text{ cm}^{-3}$.

The diffracted 248-nm radiation was measured as a function of the angle (Θ) with respect to the direction of the incident radiation. The incident laser beam was blocked by a metal disk on the output window of the chamber and lens $L2$ imaged the region near the focal zone on a fluorescent screen S . The diaphragm D in front of lens $L2$ restricted the collection of the diffracted light to a solid angle of $\sim 5^\circ$ while simultaneously increasing the depth of field. The angle between the axis of the lens $L2$ and the axis of the incoming laser radiation could be readily varied up to a maximum angle of $\Theta \sim 15^\circ$. Two flat mirrors coated for high reflection ($\sim 99\%$) at 248 nm, both having a spectral bandwidth of $\sim 10 \text{ nm}$, served

in reflection as spectral filters (F) for the diffracted laser radiation so that only the scattered 248-nm radiation could illuminate the screen. An attenuator A was employed to adjust the intensity on the screen and the images formed were recorded through the visible fluores-

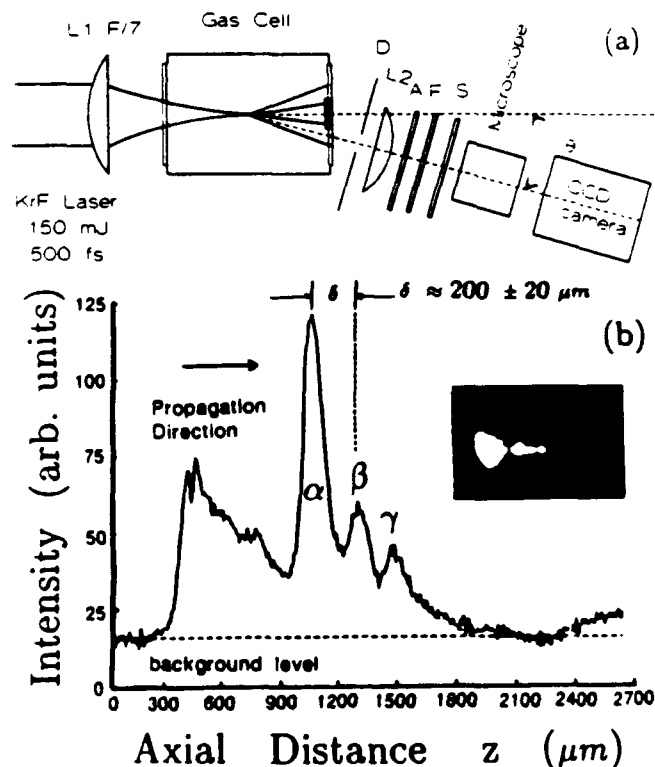


FIG. 1. (a) Experimental apparatus used in studies of propagation. See text for description. (b) Data concerning the pattern of propagation observed with a single pulse in N_2 at a density of $\sim 1.35 \times 10^{20} \text{ cm}^{-3}$. The maximum intensity is half the detector (CCD) saturation. The radiation is incident from the left. Inset: Photographic data with a vertical spatial resolution of $\sim 10 \mu\text{m}$. The graph illustrates the one-dimensional axial profile taken along the direction of propagation (z) of the photographic data (inset). The spacing of the maxima, $\delta \approx 200 \pm 20 \mu\text{m}$, is indicated.

cence produced with a microscope and a charge-coupled-device (CCD) camera.

The characteristic behavior observed is well illustrated by the data recorded with N_2 . The measured result, shown in Fig. 1(b), corresponds to a density $\rho_{N_2} \sim 1.35 \times 10^{20} \text{ cm}^{-3}$. To the left, in the photographic inset, a relatively large cone of light Rayleigh scattered from the plasma is visible at all angles as the energy propagates toward the focal point of the lens, while, in the region to the right of the conical apex, a narrow filament developed. The diameter of this filament is not greater than $10 \mu\text{m}$, the measured spatial resolution of the imaging system. The distribution of intensity observed along the filament exhibited several bright features attributed to diffraction because they could not be seen for $\Theta > 20^\circ$. Since the axis of the imaging lens corresponded to an angle $\Theta = 7.5^\circ$, the scale along the abscissa of the photographic data is reduced by almost eightfold, giving the maximum length of the filament as $\sim 1 \text{ mm}$. The graph in Fig. 1(b) represents a one-dimensional axial profile, taken along the direction of propagation (z), of the observed intensity pattern (inset). Three peaks (α, β, γ) are visible with a spatial separation of $\delta = 200 \pm 20 \mu\text{m}$. The normal Rayleigh range for the focal geometry used was $\sim 200 \mu\text{m}$.

The diameter of the filamentary channel is an important dynamical variable, which we estimated by measuring the maximum angular deviation of the diffracted light. The experimental value ϕ of this diffracted cone was $\phi \sim 20^\circ$, a magnitude indicating a radius $r_0 \sim 0.9 \mu\text{m}$ though the relation $\phi = 1.22\lambda/r_0$. Filaments of this general nature were observed at densities above $\sim 1.35 \times 10^{20} \text{ cm}^{-3}$ in N_2 , Ne, Ar, Kr, CO_2 , and a mixture of Xe (4%) and N_2 (96%), but not in He and Xe, two materials discussed further below.

Two mechanisms exist that could modify the refractive index of the medium and lead to the observed behavior. They are (1) the Kerr effect stemming from the ions and (2) the relativistic and charge-displacement process [7]. Since the pulse duration is very short ($\sim 500 \text{ fs}$), the motion of the ions is negligible [3], and no contribution can arise from expulsion of the plasma from the high-intensity zone. An implication of the estimate of the channel radius ($r_0 \sim 0.9 \mu\text{m}$) is that the observed propagation is associated with intensities in the 10^{18} – 10^{19} W/cm^2 range. Under these conditions, available experimental evidence [9,10] on multiphoton ionization indicates that He should be fully ionized and the C, N, and O atoms constituting the molecular materials would retain, at most, only 1s electrons.

Consider explicitly the case of N_2 , which has estimated [9,10] threshold intensities for the production of N^{5+} , N^{6+} , and N^{7+} of 1.6×10^{16} , 6.4×10^{18} , and $1.3 \times 10^{19} \text{ W/cm}^2$, respectively. Hence, the volume of the channel would be largely ionized to N^{5+} , with certain localized high-intensity regions contributing some N^{6+} . Two consequences of this pattern of ionization follow, namely, (i) the Kerr effect arising from the ions is small, since the

polarizabilities of the remaining 1s electrons are low, and (ii) the electron density (n_e) initially produced in the focal region is nearly uniform. Therefore, $n_e \approx 1.35 \times 10^{21} \text{ cm}^{-3}$ for the data on N_2 shown in Fig. 1(b).

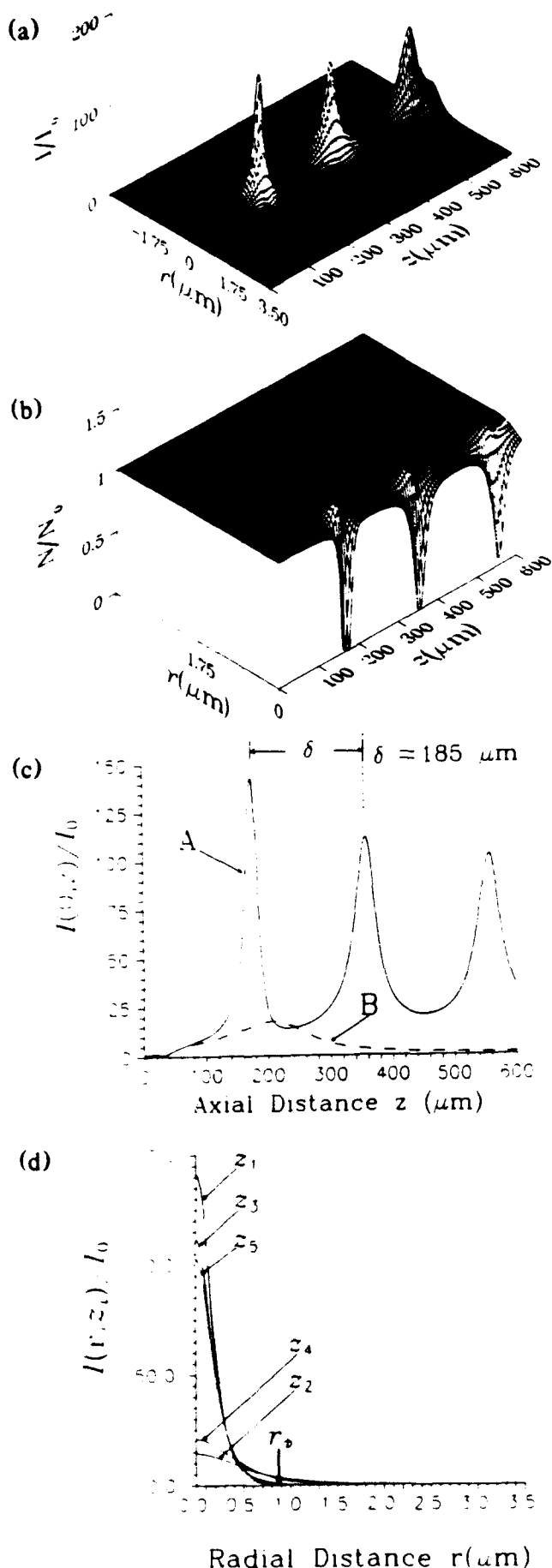
A critical power P_{cr} for self-channeling, arising from the relativistic and charge-displacement mechanism, can be defined [11] as

$$P_{cr} = (m_e^2 c^5 / e^2) \int_0^\infty g_0^2(r) r dr (\omega / \omega_{p,0})^2 \\ \approx 1.62 \times 10^{10} (n_{cr} / n_e) \text{ W}, \quad (1)$$

where m_e , e , and c have their customary identifications, ω is the laser angular frequency, $\omega_{p,0}$ is the plasma frequency for the uniform unperturbed plasma with electron density n_e , n_{cr} is the critical electron density (for $\lambda = 248 \text{ nm}$, $n_{cr} = 1.82 \times 10^{22} \text{ cm}^{-3}$), and $g_0(r)$ is the Townes mode [12].

The critical powers associated with the experimental conditions, for He and N_2 at a medium density $\rho = 1.35 \times 10^{20} \text{ cm}^{-3}$, are 1.08×10^{12} and $2.19 \times 10^{11} \text{ W}$, respectively. Therefore, since the incident power was $P \approx 3 \times 10^{11} \text{ W}$, no filament was expected in He, a prediction conforming with the observation of none. Moreover, the diffracted cone of radiation was also absent with He. In contrast, $P/P_{cr} \approx 1.37$ for N_2 , a condition that held generally ($P/P_{cr} > 1$) for all materials which exhibited evidence for channel formation. We note, however, that some contribution from the Kerr effect may be present, even for the light materials (Ne, N_2 , and CO_2), in the early stage of channel formation prior to the development of a substantial level of ionization, and that the heavier gases (Ar, Kr, and Xe) may involve a more significant influence from the Kerr process. A specific estimate of the nonlinear index change arising from both N^{5+} and N^{6+} at an intensity of $\sim 10^{19} \text{ W/cm}^2$ indicates that their contribution is less than 10^{-3} that of the free electrons; hence the ionic contribution can be neglected in N_2 for the conditions studied.

A direct comparison will now be made between the theoretical analysis, fully described in Ref. [7], and the experimental findings for N_2 . This comparison can be accomplished for both the longitudinal intensity profile and the radial extent of the channel. Figure 2(a) illustrates the intensity profile $I(r, z)/I_0$ calculated with physical parameters corresponding to those of the experiment (i.e., $P \approx 3 \times 10^{11} \text{ W}$, $r_0 = 3.5 \mu\text{m}$, $n_e = 1.35 \times 10^{21} \text{ cm}^{-3}$, and $P/P_{cr} = 1.37$). Importantly, *all* of these parameters are based on *independent* measurements of (1) the laser pulse involving determinations of the energy and power (P), (2) the focal radius (r_0) of the incident radiation, and (3) the characteristics of the multiphoton ionization [10] generating the electron density (n_e). Therefore, this comparison does *not* involve a fit with a free parameter. The normalized electron density calculated is presented in Fig. 2(b), from which it is seen that electronic cavitation occurs only near the positions of the maxima in the intensity profile [Fig. 2(a)]. Curve A in Fig. 2(c) represents



the one-dimensional axial intensity profile $I(0,z)/I_0$ corresponding to the calculated distribution shown in Fig. 2(a). The spacing (δ) of the maxima is seen to be $\delta \sim 185 \mu\text{m}$, a value in close agreement with the experimental figure ($\delta = 200 \pm 20 \mu\text{m}$) illustrated in Fig. 1(b). Furthermore, analysis has shown that the spacing δ is quite sensitive to the power P_0 and electron density n_e , particularly in the region close to the threshold [see Eq. (1)]. With respect to the results illustrated in Fig. 2(c), an increase in n_e by less than 5% causes a reduction in the spacing δ by approximately 25%. Therefore, substantial changes in the physical parameters would grossly alter the comparison of the experimental and theoretical results.

Theoretical studies [3-7,11] indicate that the charge displacement plays a very important dynamical role. In order to test this hypothesis, identical calculations were made for N_2 for the purely relativistic case [2] which explicitly neglects the charge-displacement term, namely, elimination of the term $(c^2/\omega_p^2 \sigma \delta^2) \Delta_\perp (1 + 1/I_e)^{1/2}$ in Eq. (24) of Ref. [7]. Significantly, the resulting axial profile [curve B in Fig. 2(c)] exhibits only a *single* relatively weak maximum, for $0 \leq z \leq 600 \mu\text{m}$, an outcome sharply at variance with both the full theoretical analysis and the experimental observation. Although the expected charge displacement is highly localized [Fig. 2(b)], this comparison reveals the strong influence it has on the propagation [3,7,11]. At a greater incident power ($P/P_{cr} \sim 10$), a continuous channel in the electron distribution is expected to develop [7].

The measurements indicated an approximate value of $r_0 \approx 0.9 \mu\text{m}$ for the radial extent of the channel, a result that can be compared with the corresponding theoretical figure. Figure 2(d) illustrates five radial intensity profiles $I(r,z_i)/I_0$ of the distribution pictured in Fig. 2(a). Since the measurement of this angularly scattered radiation did not correspond to a known longitudinal position, this comparison can only be qualitative, but the radial distributions shown indicate that the expected value lies in the interval $0.5 \leq r \leq 1.0 \mu\text{m}$, a range that comfortably includes the experimental value r_0 .

The results observed with Xe deserve additional discussion, since those experiments did not give evidence for the formation of a channel. In significant contrast to the case involving N_2 , the electron density n_e produced by the multiphoton ionization [10] in Xe is expected to be very

FIG. 2. Calculations for N_2 with $P = 3 \times 10^{11} \text{ W}$, $r_0 = 3.5 \mu\text{m}$, $n_e = 1.35 \times 10^{21} \text{ cm}^{-3}$, and $I_0 = 8.6 \times 10^{17} \text{ W/cm}^2$. (a) Normalized intensity $I(r,z)/I_0$. (b) Normalized electron density $N(r,z)/N_0$ for $N_0 = n_e$. (c) Normalized one-dimensional axial intensity profiles $I(0,z)/I_0$. Curve A, full theory for data in panel (a), $\delta = 185 \mu\text{m}$. Curve B, calculation with charge-displacement term neglected. (d) Normalized radial intensity profiles $I(r,z_i)/I_0$ corresponding to panel (a). Longitudinal positions $z_1 = 172 \mu\text{m}$, $z_2 = 245 \mu\text{m}$, $z_3 = 358 \mu\text{m}$, $z_4 = 441 \mu\text{m}$, and $z_5 = 559 \mu\text{m}$ and $r_0 = 0.9 \mu\text{m}$.

nonuniform spatially. For intensities spanning 10^{16} – 10^{18} W/cm², the corresponding density n_e would vary by over a factor of 2. Since this nonuniformity would tend to reduce the refractive index locally in the central high-intensity region, a significant defocusing action is expected which could suppress the channel formation.

Finally, we note (1) that the intensity distribution is not expected to depend strongly on the state of polarization [13,14] and (2) that losses to the plasma may be significant, particularly at electron densities close to n_{cr} .

The first experiments examining a new relativistic regime of high-intensity pulse propagation in plasmas have been performed and the findings indicate the formation of a channeled mode of propagation over a length considerably greater than the Rayleigh range. Specific comparisons of the experimental observations with a dynamical theory, which explicitly includes both the influence of the relativistic mass shift and the displacement of the electronic component of the plasma, produce excellent agreement for both the longitudinal structure of the intensity profile and the radial extent of the channel. While the present channel contains several foci, a continuous channel is predicted to develop at higher power. Finally, the intrinsically very high concentration of power associated with this mechanism of channeled propagation provides an efficient and general method for the production of conditions necessary for x-ray amplification [15].

The authors acknowledge the expert technical assistance of J. Wright and P. Noel in addition to fruitful conversations with A. R. Hinds, R. R. Goldstein, and B. Bouma. Support for this research was partially provided under Contracts No. AFOSR-89-0159, (ONR) No. N00014-91-J-1106, (SDI/NRL) No. N00014-91-K-2013, (ARG) No. DAAL 3-91-G-0174, (DOE) No. DE-FG02-91ER12108, and (NSF) No. PHY-9021265.

- [1] C. Max, J. Arons, and A. B. Langdon, *Phys. Rev. Lett.* **33**, 209 (1974).
- [2] A. B. Borisov, A. B. Borovskiy, V. V. Korobkin, A. M. Prokhorov, C. K. Rhodes, and O. B. Shiryayev, *Phys. Rev. Lett.* **65**, 1753 (1990).
- [3] J. C. Solem, T. S. Luk, K. Boyer, and C. K. Rhodes, *IEEE J. Quantum Electron.* **25**, 2423 (1989).
- [4] P. Sprangle, E. Esarey, and A. Ting, *Phys. Rev. Lett.* **64**, 2011 (1990); P. Sprangle, C. M. Tang, and E. Esarey, *Phys. Rev. A* **41**, 4463 (1990); A. Ting, E. Esarey, and P. Sprangle, *Phys. Fluids B* **2**, 1390 (1990).
- [5] G. Z. Sun, E. Ott, Y. C. Lee, and P. Guzdar, *Phys. Fluids* **20**, 526 (1987).
- [6] T. Kurki-Suonio, P. J. Morrison, and T. Tajima, *Phys. Rev. A* **40**, 3230 (1989).
- [7] A. B. Borisov, A. V. Borovskiy, O. B. Shiryayev, V. V. Korobkin, A. M. Prokhorov, J. C. Solem, T. S. Luk, K. Boyer, and C. K. Rhodes, *Phys. Rev. A* (to be published).
- [8] T. S. Luk, A. McPherson, G. Gibson, K. Boyer, and C. K. Rhodes, *Opt. Lett.* **14**, 1113 (1989).
- [9] S. Augst, D. Strickland, P. D. Meyerhofer, S. L. Chin, and J. H. Eberly, *Phys. Rev. Lett.* **63**, 2212 (1989).
- [10] G. Gibson, T. S. Luk, and C. K. Rhodes, *Phys. Rev. A* **41**, 5049 (1990).
- [11] A. B. Borisov, A. V. Borovskiy, V. V. Korobkin, A. M. Prokhorov, O. B. Shiryayev, and C. K. Rhodes, *J. Laser Phys.* **1**, 103 (1991).
- [12] R. Y. Chiao, E. Garmire, and C. H. Townes, *Phys. Rev. Lett.* **13**, 479 (1964).
- [13] P. Avan, C. Cohen-Tannoudji, J. Dupont-Roc, and C. Fabre, *J. Phys. (Paris)* **37**, 993 (1976).
- [14] S. V. Bulanov, V. I. Kirsanov, and A. S. Sakharov, *Fiz. Plazmy* **16**, 935 (1990) [*Sov. J. Plasma Phys.* **16**, 543 (1990)].
- [15] K. Boyer, A. B. Borisov, A. V. Borovskiy, O. B. Shiryayev, D. A. Tate, B. E. Bouma, X. M. Shi, A. McPherson, T. S. Luk, and C. K. Rhodes, "Method of Concentration of Power in Materials for X-Ray Amplification" (to be published).

Appendix G: "Relativistic and Charge-Displacement Self-Channeling of Intense Ultrashort Laser Pulses in Plasmas"

Relativistic and charge-displacement self-channeling of intense ultrashort laser pulses in plasmas

A. B. Borisov*

Laboratory for Computer Simulation, Research Computer Center, Moscow State University, 119 899 Moscow, Russia

A. V. Borovskiy

General Physics Institute, Academy of Sciences of Russia, 117 942 Moscow, Russia

O. B. Shiryayev*

Laboratory for Computer Simulation, Research Computer Center, Moscow State University, 119 899 Moscow, Russia

V. V. Korobkin and A. M. Prokhorov

General Physics Institute, Academy of Sciences of Russia, 117 942 Moscow, Russia

J. C. Solem

Theoretical Division, Los Alamos National Laboratory, Los Alamos, New Mexico 87545

T. S. Luk, K. Boyer, and C. K. Rhodes

Department of Physics, University of Illinois at Chicago, Chicago, Illinois 60680

(Received 25 June 1991; revised manuscript received 20 November 1991)

A simple derivation in the Coulomb gauge of the nonlinear Schrödinger equation describing propagation of powerful ultrashort circularly polarized laser pulses in underdense cold inhomogeneous plasmas is presented. Numerical solutions are given for the two-dimensional axisymmetric case for both initially homogeneous plasmas and static preformed plasma columns. These solutions account for (i) diffraction, (ii) refraction arising from variations in the refractive index due to the spatial profile of the electron density distribution, (iii) the relativistic electronic mass shift, and (iv) the charge displacement resulting from the transverse ponderomotive force. The most important spatial modes of propagation corresponding to (1) purely relativistic focusing and (2) the combined action of both the relativistic and charge-displacement mechanisms are described. The latter leads to the formation of stable confined modes of propagation having paraxially localized regions of high intensity and corresponding paraxially situated cavitating channels in the electron density. It is further demonstrated that the dynamical solutions of the propagation tend asymptotically to the lowest eigenmodes of the governing nonlinear Schrödinger equation. Finally, the calculations illustrate the dynamics of the propagation and show that the relativistic mechanism promotes the initial concentration of the radiative energy and that the subsequent charge displacement stabilizes this confinement and produces waveguidelike channels.

PACS number(s): 52.40.Nk, 42.65.Jx, 52.35.Mw, 52.40.Db

I. INTRODUCTION

The interaction of relativistically intense subpicosecond laser pulses with gaseous media has been an area of vigorous research for the past several years. For ultraviolet wavelengths on the order of 200–300 nm, the intensity region of interest, in which relativistic effects become important, lies above $\sim 10^{18}$ W/cm². The propagation of radiation in such media, for intensities greater than $\sim 10^{16}$ W/cm², naturally causes strong nonlinear ionization in all matter. Hence, the pulse itself, even in regions where the intensity is relatively low compared to the peak value, removes many electrons [1,2] from the atomic or molecular constituents creating a plasma column in which the main high-intensity component of the pulse propagates. Therefore, in a reasonable first approximation, the investigation of the resulting propagation can be divided into two separate and distinct areas. They are (1) the atomic and plasma physics occurring in

the field of the intense electromagnetic wave leading to the ionization and (2) the subsequent nonlinear propagation of the radiation in the plasma that is generated. The work described below concerns the latter issue.

To our knowledge, Akhiezer and Polovin published the first treatment of high-intensity electromagnetic waves in a cold plasma [3]. They derived the equations describing the propagation as a function of the single canonical argument ($\omega t - kz$) appropriate for one-dimensional wave motion, reduced the problem to Lagrangian form with two integrals of motion, and presented either exact or approximate solutions corresponding to particular simplified special cases.

Several subsequent treatments have been devoted to the acceleration of charged particles in either relativistic beat waves or in the tail of a single relativistic pulse. Specifically, Noble [4] applied the equations derived by Akhiezer and Polovin to the study of single- and double-wave propagation. In other work [5] beat waves in hot

plasmas are described kinetically. The excitation of particles in cold plasmas occurring in the tail of a single intense laser pulse has also been investigated [6].

Importantly, this previous work [6], which considered the case of linear polarization, established that harmonics of the fundamental frequency are not produced at a significant power, if the plasma is underdense and the group velocity of light is close to the speed of light.

Utilizing the quasistatic approximation for the fluid equations of cold underdense plasmas, Sprangle, Esarey, and Ting [7] derived the first nonlinear, fully self-consistent set of equations describing the propagation of relativistic laser pulses into plasmas for a one-dimensional geometry. This formulation was used to obtain insight into relativistic self-focusing, including the self-consistent electron-density profiles, wake-field generation, optical guiding, and second-harmonic generation. However, since this treatment was one-dimensional, the multidimensional case remained unsolved.

An important finding of Sprangle, Esarey, and Ting [7] concerned the diffractive erosion of the leading edge of a pulse propagating in the plasma. However, in the work described below, we concentrate on the evolution of the central portion of the pulse as it propagates in the plasma and neglect the associated erosion of the leading edge.

Extensive literature exists on the motion of electrons in radiation fields of certain explicitly given forms. The solution for the case of plane monochromatic waves is known [8], and this result has been considerably extended in subsequent work [9,10]. Of course, the well-established Volkov solution for the Dirac equation also exists [11]. In particular, Bardsley, Penetrante, and Mittleman [12] have numerically simulated the relativistic dynamics of electrons in a one-electron picture that includes the effects of space charge and the spatial distribution of the radiation field.

The first treatment of the relativistic self-focusing in plasmas was developed by Max, Arons, and Langdon [13]. In addition, the general character of the electromagnetic propagation in plasmas has undergone considerable analysis. Schmidt and Horton [14], Hora [15], and Sprangle *et al.* [16,17] have evaluated the thresholds for relativistic self-focusing using analytic methods. Especially germane is the work of Sun *et al.* [18], who, for initially homogeneous plasmas, derived the two-dimensional (r, z) nonlinear Schrödinger equation governing propagation, including consideration of the combined effect of the relativistic nonlinearity and charge displacement. This work presented the lowest eigenmode of the nonlinear Schrödinger equation and included numerical evaluation of the threshold of relativistic self-focusing, the value of which has been approximately estimated in earlier work [14–17]. Finally, this analysis [18] presented the (r, z) dynamics of the propagation for the perturbed lowest eigenmode of the nonlinear Schrödinger equation for cases not involving spatial cavitation of the electron density. We note that Kurki-Suonio, Morrison, and Tajima [19] have also developed the stationary analytic solutions to this equation for a one-dimensional geometry.

Additional related works can be cited in this context. Relativistic self-focusing and beat-wave phase-velocity

control in plasma accelerators are kindred subjects [20]. Computations involving particle simulations revealing the initial process of self-focusing and subsequent ponderomotively driven electron motions have been performed [21]. Other calculations analyzing the plasma dynamics and self-focusing in heat-wave accelerators [22], as well as the consideration of the nonlinear focusing of coupled waves [23], have also appeared.

In prior publications, we have (1) investigated the general behavior of two-dimensional (r, z) axisymmetric relativistic self-focusing, (2) presented results on the process of stabilization of laser pulses in plasma columns [24], (3) described, with the use of an analytical model [25], the steady-state characteristics in cavitated channels having overdense walls, (4) reported preliminary results of calculations that evaluated the combined action of the relativistic and charge-displacement mechanisms and indicated the formation of stable confined cavitated modes of propagation [26], and (5) presented the experimental evidence of relativistic and charge-displacement self-channeling of intense subpicosecond ultraviolet radiation in plasmas [27], including specific comparison with the results of this computational model [27].

The current work presents a full description of the theory of nonlinear propagation of intense axisymmetric ultrashort laser pulses in cold underdense plasmas. In this analysis we use the term ultrashort to indicate that the duration of the pulses τ satisfies the inequality $\tau_i \gg \tau \gg \tau_e$, with τ_i and τ_e designating the response times of the ions and electrons, respectively. We consider both homogeneous plasmas and preformed plasma columns. In this study, no attempt is made to establish consistency between the local ionization state and the local laser intensity, the issue outlined in Sec. I. For sufficiently-low- Z materials, such as hydrogen (H_2), this calculation would be unimportant, since full (maximal) ionization would be achieved even in rather low intensity ($\sim 10^{15}$ – 10^{16} W/cm²) regions [28]. Since the main regime of interest for this work involves intensities greater than $\sim 10^{18}$ W/cm², we believe that the plasma conditions we have chosen for analysis are sufficiently close to the true self-consistent state to be adequate for the intended scope of this study.

The calculations discussed below have been performed with the specific goal of exploring the characteristic dynamics and stability of the propagation, including particularly, the interplay of the relativistic and charge-displacement processes. Therefore, in order to illustrate this behavior, numerical results are presented that portray the propagation and self-focusing action as a consequence of (1) the purely relativistic nonlinearity and (2) the combined action of the relativistic and charge-displacement mechanisms. Although the relativistic influence cannot be truly physically separated from the charge-displacement process, it has been examined separately because this comparison provides insight on the dynamics of the focusing action, specifically the process by which the charge-displacement and the confined propagation in the electronically cavitated channel develop. Since both the relativistic effect and the charge displace-

ment tend to locally produce a reduction in the plasma frequency (ω_p) that is more significant in the high-intensity regions, both of these effects perturb the wave fronts in a manner that encourages convergence of the wave and the formation of localized high-intensity zones. Furthermore, for both the purely relativistic and the combined cases, we have calculated the stationary eigenmodes of the nonlinear Schrödinger equation and show their relationship to the modes of propagation dynamically developed in the plasmas. In particular, it is shown that the charge displacement, especially that resulting in dynamical cavitation, has a very strong effect on the spatial character of the propagation [26].

The calculations indicate that the efficiency of confinement of the propagating energy is potentially high, namely, that a large fraction of the incident power can be trapped in a channeled mode by the combined action of the relativistic and charge-displacement processes. Furthermore, in the asymptotic regime, it is found that the channel is characterized spatially by an intensity profile and electron-density distribution corresponding to the lowest z -independent eigenstate of the nonlinear Schrödinger equation. Overall, the principal conclusion of this work is that, under appropriate conditions, a new dynamical mode of *stable highly confined propagation* naturally evolves for the propagation of sufficiently short ($\tau_i \gg \tau \gg \tau_p$) pulses of coherent radiation in plasmas. By new dynamical modes, we mean the self-channeling of the radiation through the formation of stabilized electronically cavitated paraxial modes, which result from the combined action of the relativistic and charge-displacement mechanisms. Interestingly, for ultraviolet wavelengths in the (200–300)-nm range, the power densities naturally associated with these environments can approach thermonuclear values.

In Sec. II the underlying physical concepts are presented and the governing nonlinear Schrödinger equation is derived. Section III presents the analysis of the eigenmodes of this equation. Representative results of numerical simulations of the two-dimensional axisymmetric propagation are given in Sec. IV. Section IV also contains a comparison with the purely relativistic case. Finally, the conclusions are summarized in Sec. V.

II. GENERAL CONSIDERATIONS

A. Physical model

Several physical phenomena [1–7, 14–19, 24–26, 29] play a role in the nonlinear dynamics governing the propagation of intense coherent radiation under the conditions being examined in this study. They are the following.

- (a) The creation of a plasma column by ionization in the temporally early region of the laser pulse.
- (b) The influence of the spatial variation of the refractive index arising from the nonlinear response of the dielectric properties of the medium. Two mechanisms are related to the electronic component; specifically, the relativistic shift in electron mass and the ponderomotive-driven electron motion which tends to displace elec-

trons from the high-intensity zone. For sufficiently short pulses, only the electrons are expelled from the laser beam and the more massive ions, due to their substantially greater inertia, are regarded as motionless [17, 18, 25]. A third mechanism is the nonlinear response arising from the induced dipoles of the ions, but this is generally small and negligible [25].

- (c) Defocusing mechanisms, caused by diffraction from the finite aperture and refraction by the transverse inhomogeneities in the electron density.

- (d) Dissipation of laser-beam energy by (i) motion of the electrons, (ii) ionization of the gas atoms, (iii) generation of harmonic radiation, (iv) production of inverse bremsstrahlung, (v) Compton scattering, and (vi) other amplitudes of nonlinear scattering.

The present work incorporates four phenomena: (1) the nonlinear response of the refractive index of the plasma due to the relativistic increase in the mass of the free electrons, (2) the refractive index variation due to the perturbation of the electron density by the ponderomotive force, (3) the diffraction caused by the finite aperture of the propagating energy, and (4) the refraction generated by the transversely inhomogeneous plasma density associated with the formation of a plasma column. In these calculations, preformed static plasma columns were used in order to approximate the radial distribution of ionization that is expected, if the incident laser pulses were producing the ionization on their temporally leading edge. Finally, the calculations were performed for a length of propagation that is much shorter than the characteristic length for dissipation of the energy of the pulse through ionization or other modes of energy loss.

It should be noted that the relativistic intensities characteristic of the phenomena examined in this work can be currently obtained experimentally [30–32]. In particular, the experimental parameters characteristic of the ranges that would apply to the study of these phenomena are presented in Table I. With the wavelength and range of electron densities shown in Table I, the plasma is always underdense, namely, $(\omega_p/\omega)^2 \ll 1$, where $\omega = 2\pi c/\lambda$ is the angular frequency of the laser radiation and $\omega_p = (4\pi e^2 N_e/m_e)^{1/2}$ is the customary plasma frequency.

B. The propagation equation

Consider the propagation of an intense ultrashort laser pulse in a plasma with an initially radially inhomogeneous electron density, described by the function $f(r)$, so

TABLE I. Experimental parameters characteristic of the ranges that would apply for the study of relativistic and charge-displacement self-focusing of laser pulses in plasmas.

Peak intensity	$I \approx 10^{18} - 10^{20} \text{ W/cm}^2$
Pulse length	$\tau \approx 100 - 1000 \text{ fs}$
Initial focal spot radius	$r_0 \approx 1 - 3 \text{ } \mu\text{m}$
Wavelength	$\lambda \approx 0.248 \text{ } \mu\text{m}$ (KrF* laser light)
Target gas densities	$\rho \approx 10^{16} - 10^{20} \text{ cm}^{-3}$
Initial unperturbed electron density	$N_e \approx 10^{17} - 10^{21} \text{ cm}^{-3}$

that $N_e^{(0)} = N_e f(r)$, $\max f(r) = 1$. We denote the vector and the scalar potentials of the electromagnetic fields as \mathbf{A} and ϕ , respectively, and the corresponding electric field as \mathbf{E} . Let the momentum of the electrons, the current density, and the charge density be denoted as \mathbf{p}_e , \mathbf{j} , and ρ , respectively. We assume, for the short timescale of interest, that the ions are inertially frozen in space [17,18,24,25]. Then,

$$\square \mathbf{A} = c^{-1} \nabla \frac{\partial \phi}{\partial t} - (4\pi/c) \mathbf{j}, \quad (1)$$

$$\nabla^2 \phi = -4\pi \rho, \quad (2)$$

$$(\nabla \cdot \mathbf{A}) = 0, \quad (3)$$

$$\left[\frac{\partial}{\partial t} + (\mathbf{v}_e \cdot \nabla) \right] \mathbf{p}_e = -e \left[-c^{-1} \frac{\partial \mathbf{A}}{\partial t} - \nabla \phi + c^{-1} [\mathbf{v}_e \times (\nabla \times \mathbf{A})] \right], \quad (4)$$

$$\mathbf{j} = -e N_e \mathbf{v}_e, \quad \rho = e(N_e^{(0)} - N_e), \quad (5)$$

$$\mathbf{v}_e = \mathbf{p}_e / m_e, \quad m_e = m_{e,0} \gamma, \quad (6)$$

$$\gamma = [1 + \mathbf{p}_e^2 / (m_{e,0} c)^2]^{1/2}.$$

In the set of statements above, Eqs. (1) and (2), are the Maxwell equations, Eq. (3) is the Coulomb gauge condition, Eq. (4) is the equation of motion of the electrons, Eqs. (5) are the definition of the current density and the charge density ($N_e^{(0)}$ is the initial charge density, while N_e is the dynamical charge density), and Eqs. (6) represent the relativistic relation between the velocity \mathbf{v}_e and the momentum of the electrons. In Eqs. (6), $m_{e,0}$ is the rest electron mass, $\square = \nabla^2 - c^{-2} \partial^2 / \partial t^2$.

It is convenient to normalize the values in the equations presented above as follows:

$$\begin{aligned} \tilde{\mathbf{A}} &= (e/m_{e,0} c^2) \mathbf{A}, \quad \tilde{\phi} = (e/m_{e,0} c^2) \phi, \\ \tilde{\mathbf{E}} &= (e/m_{e,0} c^2) \mathbf{E}, \quad \tilde{\mathbf{p}}_e = \mathbf{p}_e / m_{e,0} c, \\ \tilde{\mathbf{v}}_e &= \mathbf{v}_e / c, \quad \tilde{N}_e = N_e / N_{e,0}, \end{aligned} \quad (7)$$

with the understanding that, henceforth, the tilde sign will be suppressed. Using the relations $(\mathbf{p}_e \cdot \nabla) \mathbf{p}_e = \nabla (\mathbf{p}_e^2 / 2 - \mathbf{p}_e \times (\nabla \times \mathbf{p}_e))$ and $\nabla \gamma = \nabla (\mathbf{p}_e^2 / 2\gamma)$, Eq. (4) becomes

$$\frac{\partial}{\partial t} (\mathbf{p}_e - \mathbf{A}) - \mathbf{v}_e \times [\nabla \times (\mathbf{p}_e - \mathbf{A})] = \nabla (\phi - \gamma). \quad (8)$$

In the limit $\tau \gg 2\pi/\omega_p$, the expression $\mathbf{p}_e = \mathbf{A}$ is approximately valid. As we shall see below, this condition means that the electron response can be regarded as adiabatic. Furthermore, assuming the vector potential to be circularly polarized, we write

$$\mathbf{A}(r, z, t) = \frac{1}{2} [(\mathbf{e}_x + i\mathbf{e}_y) a(r, z, t) \exp[i(\omega t - kz)] + \text{c.c.}] \quad (9)$$

Consistent with the statements made above, we emphasize the use of the assumption that the pulse length in

both space and time is much greater than both the plasma ($2\pi c/\omega_{p,0}$) and electromagnetic (λ) wavelengths. This leads to the validity of the inequalities

$$\left| c^{-1} \frac{\partial a}{\partial t} \right|, \left| \frac{\partial a}{\partial z} \right| \ll |ka|, |k_p a|,$$

where $k^2 = k_0^2 - k_p^2$, $k_0 = \omega/c$, and $k_p = \omega_{p,0}/c$. We use the notation $\omega_{p,0}^2 = 4\pi e^2 N_{e,0}/m_{e,0}$ specifically to denote the unperturbed plasma frequency. With the assumptions and approximations stated above, Eqs. (1)–(8) become

$$\square \mathbf{A} = k_p^2 N_e \gamma^{-1} \mathbf{A}, \quad (10)$$

$$\nabla^2 \phi = k_p^2 [N_e - f(r)], \quad (11)$$

$$\nabla(\phi - \gamma) = 0, \quad (12)$$

$$\gamma = (1 + \mathbf{p}_e^2)^{1/2}, \quad \mathbf{p}_e = \mathbf{A}. \quad (13)$$

The term $c^{-1} \partial \nabla \phi / \partial t$ is omitted in Eq. (10), since γ and ϕ , according to Eqs. (9), (12), and (13), do not have a high-frequency dependence. Equations (11) and (12) result in the expression for the electron density,

$$N_e = \max[0, f(r) + k_p^{-2} \nabla^2 \gamma]. \quad (14)$$

The logical function $\max(0, \cdot)$ provides for the physically obvious and necessary condition $N_e \geq 0$. The analogous expression for the electron density has been previously derived by Sun *et al.* [18] for the case $f(r) \equiv 1$. It should be noted that Eq. (12) states the condition for the balance of the ponderomotive and the electrostatic forces for the relativistic case. Through combining Eqs. (9), (10), and (14), we establish the equation for the slowly varying complex amplitude of the vector potential $a(r, z, t)$ as

$$\begin{aligned} & \left[\frac{1}{v_g} \frac{\partial}{\partial t} + \frac{\partial}{\partial z} \right] a \\ & + \frac{i}{2k} (\nabla^2 a + k_p^2 [1 - \gamma^{-1} \max[0, f(r) + k_p^{-2} \nabla^2 \gamma]] a) \\ & = 0. \end{aligned} \quad (15)$$

In accord with the previous assumptions used in deriving Eq. (15), we have neglected the second z and t derivatives in this expression. In Eq. (15), $v_g = c\epsilon_0^{1/2}$ is the group velocity of light in unperturbed plasma, $\epsilon_0 = 1 - (\omega_{p,0}/\omega)^2$ is its corresponding dielectric constant, and $\gamma = (1 + a^2)^{1/2}$. It should also be noted that the electric field vector \mathbf{E} and the vector potential \mathbf{A} are related through the approximate relation

$$\mathbf{E}(r, z, t) \approx -ik_0 \mathbf{A}(r, z, t).$$

The calculation of the propagating wave form for the central high-intensity region of the pulse is accomplished by considering the solutions of Eqs. (15) along its characteristics. Changing the variable t to $q \equiv t - z/v_g$, Eq. (15) becomes

$$\frac{\partial}{\partial z} a + \frac{i}{2k} (\nabla_{\perp}^2 a + k_p^2 \{1 - \gamma^{-1} \max[0, f(r) + k_p^{-2} \nabla_{\perp}^2 \gamma]\} a) = 0, \quad (16)$$

for which we seek solutions of the form $q \equiv \text{const}$. We recall that certain solutions of Eq. (16) for the special case $f(r) \equiv 1$ have already been presented [18,19,33].

The results of the computations presented in this work are given with respect to the variables (q, r, z) . Specifically, the data presented in the figures below illustrate the propagation of the radiation along the z axis for $q \equiv \text{const}$. Equation (16) describes the two-dimensional (r, z) dynamics of propagation for coherent circularly polarized radiation in plasmas having an inhomogeneous transverse (r -dependent) distribution of electron density. The basic physical phenomena explicitly embodied in these equations have been outlined in Sec. II A.

III. STATIONARY SELF-LOCALIZED MODES OF PROPAGATION

Equation (16), in the case of homogeneous plasmas [$f(r) \equiv 1$], has axisymmetric partial solutions of the form

$$a(r, z) = U_{s,n}(k_p r) \exp[i(k_p^2/2k)(s-1)z], \quad (17)$$

where s is a real-valued dimensionless parameter and the real-valued function $U_{s,n}$ obeys the ordinary differential equation [18]

$$\nabla_{\perp}^2 U_{s,n} + [s + F(U_{s,n}^2)] U_{s,n} = 0. \quad (18)$$

In this discussion the dimensionless argument $\rho = k_p r$ is used and ∇_{\perp}^2 in Eq. (18) denotes the Laplacian with the derivatives designated with respect to this variable (ρ).

The nonlinear term in Eq. (18) is

$$\begin{aligned} F(U_{s,n}^2) &= -N_{s,n}/\gamma_{s,n}, \\ N_{s,n} &= \max(0, 1 + \nabla_{\perp}^2 \gamma_{s,n}), \\ \gamma_{s,n} &= (1 + U_{s,n}^2)^{1/2}. \end{aligned} \quad (19)$$

The natural boundary conditions for Eq. (18) are

$$\frac{dU_{s,n}(0)}{d\rho} = 0, \quad U_{s,n}(\infty) = 0. \quad (20)$$

The first condition assures axial symmetry of the solutions, while the second is necessary for the property of finite energy for the solutions. We designate these solutions as "eigenmodes" and their significance is explored below.

Consider initially, however, the eigenmodes corresponding to the purely relativistic case, functions which are obtained from Eqs. (18) and (19) by neglecting the term $\nabla_{\perp}^2 \gamma_{s,n}$. Since, we are explicitly eliminating the ponderomotive potential and its influence on the motion of the electrons, in this situation the electron density will not be self-consistent. In this restricted case, Eq. (18) can be rewritten in the form

$$\frac{d}{d\rho} \left[\frac{1}{\gamma} \frac{dU_{s,n}}{d\rho} \right]^2 + V(U_{s,n}, s) = -\rho^{-1} \left[\frac{dU_{s,n}}{d\rho} \right]^2,$$

where $V(U_{s,n}, s) = (s/2)U_{s,n}^2 - (1 + U_{s,n}^2)^{1/2} + 1$.

The second boundary condition, stated in Eq. (20), ensures finiteness of energy only in the situation where the dynamical system defined by the last two expressions has three rest points, one of them being zero, that is for the case $0 < s < 1$. Exactly as in the classic theory of cubic media [34,35] for values of the parameter s belonging to this interval, the localized eigenmodes constitute a countable set that is ordered by the number of zeros— n in each of its members for finite values of ρ . Figure 1 illustrates the first four eigenmodes for $s = 0.95$.

Consider now the eigenmode corresponding to the unrestricted situation that includes both the relativistic and charge-displacement mechanisms, a case which is found to be fully analogous. The eigenmodes of the equation describing the combined relativistic and charge-displacement processes for the interval $0 < s < 1$ also make a countable set that can be ordered in the same way as the one associated with the purely relativistic case. The zeroth (lowest) eigenmode $U_{s,0}(\rho)$ with $s = 0.95$, along with the corresponding electron density $N_{s,0}(\rho)$, given by the second formula in Eq. (19), are depicted in Fig. 2. These two functions have been developed in earlier work [18]. The first and second relativistic and charge-displacement eigenmodes for the value of the parameter $s = 0.95$ and the corresponding electron-density eigenmodes $N_{s,1}(\rho)$ and $N_{s,2}(\rho)$ are depicted in Figs. 3 and 4, respectively. These higher eigenmodes exhibit the important feature that cavitation may occur in the electronic component of plasma [see Fig. (4)], even if it does not occur in the case of the lower eigenmodes [see Figs. 2 and 3].

A prior study [18] treated the (r, z) dynamics of the evolution of the perturbed lowest eigenmodes for the case in which no cavitation of the electronic component of plasma occurs. The lowest eigenmodes were perturbed by multiplying them by constants in the neighborhood of unity. In this case, the known regime involving oscillatory propagation was observed. However, the instability of the numerical method applied in that work [18] prevented the performance of similar computations for cases involving cavitation. Our calculations show that the analogously perturbed lowest eigenmodes $V_{s,0}(\rho)$ also propagate in the same oscillatory fashion when electronic cavitation occurs, the corresponding density of which is given by $N_{s,0}(\rho)$. It is also found that the same behavior devel-



FIG. 1. Stationary axially symmetric eigenmodes $s = 0.95$ corresponding to purely relativistic self-focusing.

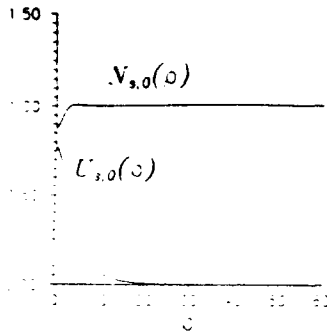


FIG. 2. The zeroth (lowest) axially symmetric stationary eigenmode with $s=0.95$ corresponding to relativistic and charge-displacement self-focusing: the normalized field amplitude distribution $U_{s,0}(\rho)$ and the normalized electron density distribution $N_{s,0}(\rho)$.

ops for the perturbed first eigenmodes, which have one or two cavitated channels in the electronic density described by $N_{s,1}(\rho)$. The results of these simulations can be regarded as evidence of the (r,z) stability of axially symmetric lowest and first eigenmodes against small perturbations in the amplitude. It should be noted, however, that these higher eigenmodes are presumably unstable against small *azimuthal* perturbations, the nature of which violates the assumed axial symmetry of the distributions.

The important consequence of the character of the solutions discussed above is the fact that the power

$$P_s = 2\pi \int_0^\infty U_{s,0}^2(\rho) \rho d\rho$$

contained in the intensity distribution corresponding to the lowest eigenmode $U_{s,0}(\rho)$, unlike the case of a cubic medium, depends on the parameter s . Namely, this power decreases as s increases.

The infimum of P_s by s , in the interval $0 < s < 1$, is called the critical power (P_{cr}) of the relativistic and charge-displacement self-focusing. This power equals the critical power of the purely relativistic self-focusing [18,36] and

$$P_{cr} = \inf_{0 < s < 1} P_s = \lim_{s \rightarrow 1-0} P_s.$$

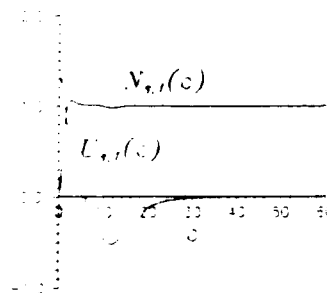


FIG. 3. The first axially symmetric stationary eigenmode with $s=0.95$ corresponding to relativistic and charge-displacement propagation: the normalized amplitude distribution $U_{s,1}(\rho)$ and the normalized electron density distribution $N_{s,1}(\rho)$.

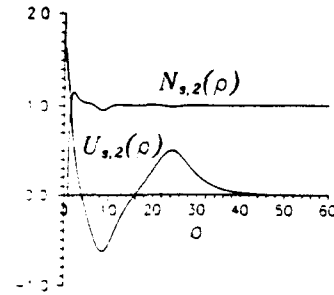


FIG. 4. The second axially symmetric stationary eigenmode with $s=0.95$ corresponding to relativistic and charge-displacement propagation: the normalized amplitude distribution $U_{s,2}(\rho)$ and the normalized electron density distribution $N_{s,2}(\rho)$.

The explicit evaluation of this critical value is presented below. As $U_{s,0}(\rho) \rightarrow 0$, $N_{s,0}(\rho) \rightarrow 1$ for $s \rightarrow 1-0$; we have [18] therefore,

$$\begin{aligned} \gamma_{s,0}^{-1} N_{s,0} - 1 &= N_{s,0} (1 + U_{s,0}^2)^{-1/2} - 1 \\ &\underset{s \rightarrow 1-0}{\approx} (1 + U_{s,0}^2/2)^{-1} - 1 \underset{s \rightarrow 1-0}{\approx} -U_{s,0}^2/2. \end{aligned}$$

Furthermore,

$$U_{s,0}(\rho) \underset{s \rightarrow 1-0}{\approx} U_0(\rho),$$

where $U_0(\rho)$ is the positive, monotonically decreasing (reaching zero for no finite value of ρ) solution to the boundary-value problem [18,36]

$$\nabla_1^2 U_0 - \epsilon U_0 + \frac{1}{2} U_0^3 = 0,$$

$$\frac{dU_0}{d\rho}(0) = 0, \quad U_0(\infty) = 0,$$

with $\epsilon = 1 - s$. A change of the variables, which is a standard procedure for treating the case of the cubic nonlinearity [37], shows that [36]

$$U_0(\rho) = (2\epsilon)^{1/2} g_0(\epsilon^{1/2} \rho),$$

where g_0 is the customary Townes mode, i.e., the positive, monotonically vanishing solution to the following boundary-value problem:

$$\nabla^2 g_0 - g_0 + g_0^3 = 0,$$

$$\frac{dg_0}{d\rho}(0) = 0, \quad g_0(\infty) = 0.$$

From the definition of P_{cr} and the relation between $U_0(\rho)$ and $g_0(\rho)$, it follows that

$$\begin{aligned} P_{cr} &= \inf_{0 < s < 1} P_s = \lim_{s \rightarrow 1-0} P_s \\ &= 2\pi \int_0^\infty U_0^2(\rho) \rho d\rho \\ &= 4\pi \int_0^\infty g_0^2(\rho) \rho d\rho = 2P_{cr,c}, \end{aligned}$$

where $P_{cr,c} \equiv 2\pi \int_0^\infty g_0^2(\rho) \rho d\rho$ is the critical power of the Kerr self-focusing in cubic media [34,37].

Using the resulting relation between the normalized values of the critical power of the relativistic and charge-

displacement self-focusing P_{cr} and the critical power of the Kerr self-focusing $P_{cr,c}$ we have the elementary result that

$$P_{cr} = 2P_{cr,c}.$$

Finally, by calculating $g_0(\rho)$ numerically, we find the normalized value of P_{cr} with high precision [36] to be

$$P_{cr} = 2P_{cr,c} = 4\pi \int_0^\infty g_0^2(\rho) \rho d\rho \approx 23.4018.$$

Hence, we establish the expression for the critical power [36] as

$$P_{cr,1} = (m_{e,0}^2 c^5 / e^2) \int_0^\infty g_0^2(\rho) \rho d\rho (\omega / \omega_{p,0})^2 \\ \approx 1.6198 \times 10^{10} (\omega / \omega_{p,0})^2 \text{ W}.$$

The constant factor involved in this statement improves on that given previously [18].

The relation between $U_0(\rho)$ and $g_0(\rho)$ enables the development of the asymptotic expressions (in the case $\epsilon \rightarrow 0$) for both the peak value of the amplitude of the stationary eigenmode and for the radius of the eigenmode by using the appropriate characteristics of the Townes mode. The results are

$$U_{s,0}(0) \approx (2\epsilon)^{1/2} g_0(0)$$

and

$$r_s \approx \epsilon^{-1/2} r_0,$$

for $\epsilon \rightarrow 0$.

Special computations were performed in order to determine how close the values for $U_{s,0}(0)$ and $U_0(0) = (2\epsilon)^{1/2} g_0(0)$ are in the case where $\epsilon \ll 1$. The calculations show that $U_{s,0}(0) - U_0(0) / U_0(0)$ is 2.026×10^{-5} and 2.096×10^{-6} for $\epsilon = 10^{-5}$ and 10^{-6} , respectively.

IV. THE TWO-DIMENSIONAL CASE

It is convenient to treat Eq. (16) numerically using the normalized coordinates

$$r_1 = r/r_0, \quad z_1 = z/(2kr_0^2),$$

$$u(r_1, z_1) = a_0^{-1} a(r, z),$$

where r_0 is a characteristic radius of the initial intensity profile and $a_0 = \max |a(r, 0)|$ for the selected value of q . For simplicity, we put $f_1(r_1) = f(r)$ and omit below the subscript 1 of r_1 and z_1 for brevity. Thus, the mathematical statements can be expressed in the following set of equations:

$$\frac{\partial u}{\partial z} + i \nabla^2 u + i F(f_1(r), |u|^2) u = 0, \quad z > 0 \quad (21)$$

$$u(r, 0) = u_0(r), \quad \max_r |u_0| = 1 \quad (22)$$

$$\frac{\partial u}{\partial r}(0, z) = 0, \quad u(\infty, z) = 0. \quad (23)$$

The nonlinear term F is the real-valued operator

$$F(f_1, \xi) = a_1 \{1 - (1 + a_2 \xi)^{-1/2}$$

$$\times \max[0, f_1(r) + a_1^{-1} \nabla^2 (1 + a_2 \xi)^{1/2}]\} \quad (24)$$

and the dimensionless parameters a_1, a_2 are defined as

$$a_1 \equiv (r_0 k_p)^2, \quad a_2 \equiv I_0 / I_r, \quad I_0 \equiv m_{e,0}^2 \omega^2 c^3 a_0^2 / (4\pi e^2), \quad (25)$$

where I_0 is the peak intensity at the entrance plane ($z=0$) of the medium. The parameter $I_r = m_{e,0}^2 \omega^2 c^3 / (4\pi e^2)$ is known as the relativistic intensity [15].

The ratio of the power of the beam P_0 and the critical power of the relativistic and charge-displacement self-focusing P_{cr} , defined in Sec. III, is an important parameter characterizing Eqs. (21)–(24). In the notations of the present section, the value of P_0/P_{cr} can be expressed in the following way [36]:

$$P_0/P_{cr} = (a_1 a_2 / B) \int_0^\infty |u_0(r)|^2 r dr,$$

with dimensionless constant B given by [36]

$$B = 2 \int_0^\infty g_0^2(\rho) \rho d\rho \approx 3.72451.$$

When the initial transverse-intensity distribution is Gaussian, namely, $|u_0(r)|^2 = \exp(-r^2)$, we have

$$P_0/P_{cr} = a_1 a_2 / (2B).$$

We note that in several other studies, the critical power of the relativistic self-focusing is defined alternatively, basically with $B=4.0$. In the present discussion, the expression for P_0/P_{cr} involves a value of $B < 4.0$, so that the corresponding ratio P_0/P_{cr} is raised. Therefore, a pulse having a Gaussian initial transverse-intensity distribution and a flat initial wave front with the parameters $a_1 = 248.6192$ and $a_2 = 0.031$, undergoes self-focusing. In this case, the ratio P_0/P_{cr} , as defined above, evaluates to 1.0347, namely, $P_0 > P_{cr}$. However, using the value $B=4.0$ would give $P_0 < P_{cr}$, a statement contradicting the results of the computations.

A. The initial conditions

In this section, we examine the self-focusing of coherent radiation for pulses having Gaussian or hyper-Gaussian transverse and longitudinal intensity distributions [24] of the form

$$I|_{z=0} = I_0(r, t) = I_m \exp[-(t/\tau)^{N_1} - (r/r_0)^{N_2}], \quad N_1 \geq 2, \quad N_2 \geq 2 \quad (26)$$

with r and t being dimensional. We assume [24] that $I_m \approx I_r \gg I^* = 10^{16} \text{ W cm}^{-2}$ with I^* designating the approximate value of the threshold for rapid nonlinear ionization [1,2]. The spatial amplitude distribution of the incident radiation, defined by Eq. (26) for the case of a flat incident phase front, is of the form

$$u_0(r) = \exp(-r^{N_2}/2), \quad N_2 \geq 2. \quad (27)$$

The dimensionless parameter a_2 in Eq. (25), corresponding to the incident pulse intensity on the axis ($r=0$) of the beam $I_0(t)$, is

$$a_2 = I_0(t)/I_r = (I_m/I_r) \exp[-(t/\tau)^{N_1}]. \quad (28)$$

The transverse profile of the plasma column, created by the temporally leading edge of the pulse, is simulated by the hyper-Gaussian function

$$f(r) = \exp[-(r/r_*)^{N_3}], \quad N_3 \geq 2, \quad (29)$$

where r is the radial coordinate. The aperture of the plasma column r_* can be estimated [24] with the use of the relation

$$I_0(r_*, t_0) \equiv I_0(t_0) \exp[-(r_*/r_0)^{N_2}] = I^*. \quad (30)$$

For example, in the case of the Gaussian transverse intensity distribution ($N_2=2$), the aperture of the plasma column for $I^* = 10^{16} \text{ W cm}^{-2}$, $I_r \approx 0.45 \times 10^{20} \text{ W cm}^{-2}$, and $I_0(t_0) = (0.1)I_r$, gives $r_* \approx 2.47r_0$. In this situation, the homogeneous plasma approximation $f(r) \equiv 1$ is valid [24]. In contrast, it follows from Eq. (30) for plateau-like incident-transverse-intensity distributions that the aperture r_* of the simulated plasma column tends to the value of the beam aperture r_0 . Therefore, in the example given above for $N_2=8$, we have $r_* \approx 1.25r_0$. Thus, defocusing of the beam, which is significant because of the near coincidence of the apertures of the laser beam and the plasma column, must be taken into account when the evolution of a beam with a plateau-like incident-transverse-intensity distribution is studied [24].

B. Relativistic self-focusing

Consider the two-dimensional (r, z) solutions of the system of equations embodied in Eqs. (21), (22), and (23) for the purely relativistic nonlinear term, the form of which can be obtained from Eq. (24) by disregarding the term involving ∇_z^2 . In this case, we find

$$F(f_1, \xi) = a_1 \{1 - f_1(r)(1 + a_2 \xi)^{-1/2}\}.$$

The relativistic self-focusing mechanism prevails over the charge-displacement mechanism outside of the focal spot under the conditions $a_1 \gg 1$, $a_2 \approx 1$. (Discussion of the conditions for the prevailing of the relativistic self-focusing can also be found in Ref. [33]). The situation represented by Eqs. (21), (22), and (23), with the above nonlinear term, describes self-focusing with a nondissipative saturation of the nonlinearity. The properties of the solutions for this case depend essentially on the values of two conserved integrals given specifically by

$$P_1 = \int_0^\infty u(r)^2 r dr \quad (31)$$

and

$$P_2 = \int_0^\infty \left[\frac{\partial u}{\partial r}^2 - \phi(r, u^2) \right] r dr. \quad (32)$$

where

$$\begin{aligned} \phi(r, \xi) &= \int_0^\xi F(r, \eta) d\eta \\ &= a_1 \{ \xi - (2/a_2) f_1(r) [(1 + a_2 \xi)^{1/2} - 1] \}. \end{aligned} \quad (33)$$

Figure 5 illustrates the nature of the calculated solutions corresponding to this purely relativistic case. The parameters of the incident radiation and plasma, for the examples presented in Fig. 5, are $\lambda = 0.248 \text{ } \mu\text{m}$, $I_r = 0.45 \times 10^{20} \text{ W cm}^{-2}$, $I_0 = \frac{1}{3}I_r = 3 \times 10^{19} \text{ W cm}^{-2}$, $r_0 = 3 \text{ } \mu\text{m}$, and $N_{e,0} = 7.5 \times 10^{20} \text{ cm}^{-3}$. The corresponding values of the associated dimensionless parameters are $a_1 \approx 2.486192 \times 10^2$ and $a_2 = \frac{2}{3}$.

Figure 5(a) presents the result for purely relativistic propagation in a homogeneous plasma along the z axis for a pulse having an incident Gaussian transverse intensity distribution and a flat wave front [$N_2=2$ in Eq. (27)] for the value of q defined in Sec. II B, corresponding to $I_0 = \frac{1}{3}I_r$. Figure 5(b) presents the analogous graph for a plateau like incident transverse intensity distribution [$N_2=8$ in Eq. (27)]. We conclude from these results that the solution is critically dependent upon the initial condition represented by the detailed character of the incident transverse intensity distribution.

The ratio of the beam power (P_0) to the critical power (P_{cr}) of the relativistic self-focusing for the given values of the parameters a_1 and a_2 yields $P_0/P_{cr} = 22.252$ in the case of the Gaussian initial transverse intensity distribution [$N_2=2$ in Eq. (27), Fig. 5(a)] and $P_0/P_{cr} = 20.168$ in the latter example of the plateau-like [$N_2=8$ in Eq. (27), Fig. 5(b)] initial transverse intensity distribution.

Note that for the values of the parameters a_1, a_2 and incident wave forms studied, we have from Eq. (32) $P_2 < 0$. In this situation, the following inequality is valid:

$$\max_r |u(r, z)|^2 > (4/a_1 a_2) |P_2| / P_1, \quad (34)$$

namely, with respect to the radial coordinate r , the maximum beam intensity has a positive lower bound independent of z . This conclusion can be established in the same way that Zakharov, Sobolev, and Synakh [37] demonstrated the analogous result in their earlier work on self-focusing. Therefore, a powerful relativistic beam, which self-focuses in a homogeneous nonabsorbing plasma ($\mu=0$, Ref. [24]), results in a field distribution representing a pulsing waveguide when $P_2 < 0$. Figures 5(a) and 5(b) explicitly illustrate the formation of such a regime. These pulsing waveguides consist of alternations of ring structures and focal spots on the axis of the beam. The power confined in these complex modes represents approximately 50% and 90% of the total incident power for the cases depicted in Figs. 5(a) and 5(b), respectively. It should be noted that oscillating periodic solutions of this type have also been presented by other workers [17].

In the case $P_2 \geq 0$, an inequality comparable to Eq. (34) cannot be obtained. Following the method of Zakharov, Sobolev, and Synakh [37], we simulate the case $P_2 \geq 0$ by considering a beam initially focused or defocused by a lens at the entrance plane ($z=0$) of the medium. Let the focusing (or defocusing) length of this lens be $R = kr^2/R$.

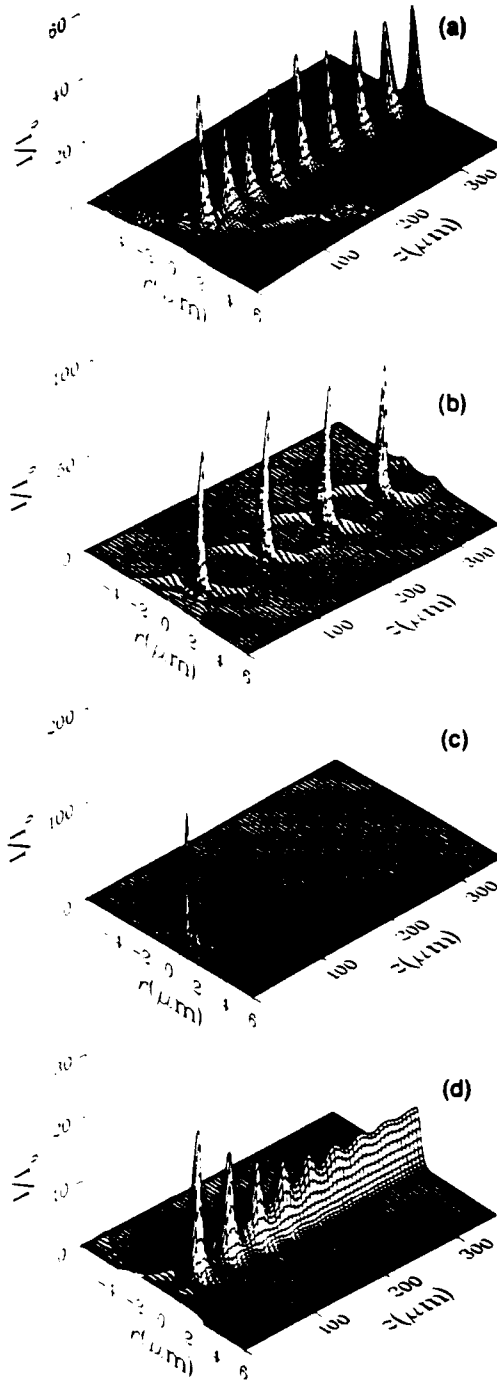


FIG. 5. Purely relativistic propagation with $I_0 = 3 \times 10^{13}$ W/cm², $r_0 = 3$ μm, $\lambda = 0.248$ μm, and $N_{e,0} = 7.5 \times 10^{20}$ cm⁻³. (a) The formation of the pulsing waveguide regime in the case of the relativistic self-focusing of a pulse with a flat incident wave front; Gaussian initial transverse-intensity distribution [$N_2 = 2$ in Eq. (27)], homogeneous plasma. (b) The formation of the pulsing waveguide regime in the case of the relativistic self-focusing of a pulse with a flat incident wave front; hyper-Gaussian initial transverse-intensity distribution [$N_2 = 8$ in Eq. (27)], homogeneous plasma. (c) The single-focus regime in the case of the relativistic self-focusing of an initially focused pulse [$R_f = R_{f,0}/2$ in Eq. (35)]; Gaussian incident-transverse-intensity distribution [$N_2 = 2$ in Eq. (35)], homogeneous plasma. (d) The formation of the quasistabilized regime in the case of the relativistic self-focusing of a pulse with a flat incident wave front in a plasma column [$N_2 = 8$, $r_0 = r_*$ in Eq. (29)]; hyper-Gaussian initial transverse-intensity distribution [$N_2 = 8$ in Eq. (27)].

(R_f dimensionless). The condition $R_f > 0$ signifies that the pulse is initially focused and $R_f < 0$ indicates that it is initially defocused. Then, the corresponding initial condition can be written as

$$u_0(r) = \exp[-r^2/2 + ir^2/(2R_f)], \quad N_2 \geq 2. \quad (35)$$

Furthermore, let $P_2 = 0$ for $R_f = R_{f,0}$. We note that the case $P_2 > 0$ corresponds physically to a high degree of the initial focusing or defocusing: $R_{f,0} > R_f > 0$. Moreover, when $R_{f,0} < R_f \leq \infty$, $P_2 < 0$.

Figures 5(a) and 5(c) display the calculated intensity distributions for the case of relativistic self-focusing in homogeneous plasma of beams with Gaussian incident-transverse-intensity distributions and values of R_f given by $R_f = \infty$ (flat wave front) and $R_{f,0}/2$, respectively. A more detailed study of the dynamics of the transition from the pulsing waveguide regime [see Fig. 5(a)], to the single-focus regime [see Fig. 5(c) representing the propagation of an initially sufficiently sharply focused beam] can be found in Ref. [38]. Importantly, the computations show that the value $P_2 = 0$ is *not* the threshold separating these two regimes of relativistic self-focusing. This transition occurs as the first focus gains power and is shifted closer to the entrance of the medium ($z = 0$), while the remaining foci are shifted in the opposite direction and, in the limit of large displacement, become diffused. Note that single-focus regimes of propagation have also been observed by Sprangle, Tang, and Esarey [17].

Defocused beams can evolve in a different fashion. Initially sufficiently sharply defocused pulses ($R_f < 0$, $R_f \leq R_{f,0}/2$, $P_2 > 0$) propagating in the relativistic regime monotonically diffuse on the radial periphery and do not exhibit the phenomenon of self-focusing.

The detailed spatial character of the plasma column can have a strong influence on the evolution of the propagation. Figure 5(d) illustrates the relativistic propagation in a plasma column along the z axis for a pulse corresponding to $N_2 = 8$ in Eq. (27). The transverse profile of the plasma column is given by $f(r)$ as defined by Eq. (29) with $N_2 = 8$ and $r_* = r_0$. The comparison between Figs. 5(b) and 5(d) demonstrates that the defocusing of a hyper-Gaussian beam in a plasma column, with an aperture close to the radius of the beam, fundamentally alters the spatial dynamics of the propagating energy [24]. If defocusing causes a fraction of the beam to spread away from the column, but the remaining energy of the beam resolves into a state that balances the relativistic self-focusing, defocusing, and diffraction. The power trapped in this quasistabilized state so formed is approximately 25% of the incident power.

Previous analytical estimates [38] have shown that the relativistic self-focusing length is minimal when the incident pulse intensity on the axis of the beam satisfies condition $I_0(t) = 2I_r$. Moreover, specific computations also show that this inference remains valid for the case of the relativistic self-focusing of pulses with flat phase fronts and Gaussian incident-transverse-intensity distributions in homogeneous plasmas.

The locus of the first focus for the case of the relativistic self-focusing has been presented previously [38].

that study, the beam initially had both a flat phase front and a Gaussian transverse-intensity distribution. The parameters were the same as those applying to Fig. 5(a), and the duration of the pulse corresponded to $\tau = 0.5 \times 10^{-13}$ s. The minimal z of the locus is reached when $I_0(t) = 2I_r$. If the maximum intensity on the axis of the beam is such that $I_m > 2I_r$, then the trajectory of the first focus executes a path that has three reversal points. Two of them, corresponding to an identical value of z , are due to the condition $I_0(t) = 2I_r$. The central one, corresponding to a greater value of z , arises when $I_0(t) = I_m$. In principle, this behavior makes it possible to distinguish the process of relativistic self-focusing from that associated with the Kerr nonlinearity, since the latter results in a locus of the first focus having only a single reversal point.

C. Relativistic and charge-displacement self-channeling

This section is devoted to the description of the self-channeling occurring when both the relativistic and charge-displacement mechanisms are included in the interaction. This situation is described by Eqs. (21)–(24) and includes the important nonlinear term involving $\nabla^2 \gamma$ appearing in Eq. (24). The numerical results show that sufficiently intense short duration ($\tau_i \gg \tau \gg \tau_e$) axisymmetric pulses readily undergo self-channeling in plasmas over a rather broad range of conditions. Moreover, it is found that a large fraction of the total incident power of the beam can be trapped in a stabilized mode confined to the axis of propagation.

A specific example is informative in representing the general behavior exhibited by the propagation in the regime in which the influence of relativity and charge displacement are both significant. These results are exhibited in Fig. 6. In the case of propagation of an initially Gaussian transverse wave form incident in a homogeneous plasma, with the parameters $\lambda = 0.248 \mu\text{m}$, $I_0 = \frac{1}{2}I_r = 3 \times 10^{19} \text{ W cm}^{-2}$, $r_0 = 3 \mu\text{m}$, and $N_{e,0} = 7.5 \times 10^{20} \text{ cm}^{-3}$ ($a_1 = 248.6192$, $a_2 = \frac{1}{2}$, $P_0/P_{cr} = 22.252$), the numerical computations show that, as soon as the first focus on the axis of propagation is formed, electronic cavitation occurs. Specifically, this leads to *complete expulsion* of the electronic component of plasma from the paraxial domain [Fig. 6(b)]. This process results in a quasistabilized cavitated channel in the electron distribution which extends along the entire axis of propagation past the location of the initial focus [26]. We note that some of the lowest stationary solutions corresponding to the relativistic and charge-displacement problem, including cavitation, were developed by Sun *et al.* [18]. The analysis shows that the first focus involves about 45% of the total incident power of the propagating energy. A fraction of the remaining power is dissipated through diffraction on the periphery, while another component is temporarily involved in the formation of a pulsing ring-shaped structure [Fig. 6(a)]. Subsequent energy exchange between the ringlike feature and the paraxial zone is observed, and as a consequence of this interaction, a certain part of the energy of the pulsing ring is diffracted away while the remaining power joins the paraxial domain.

In finer detail, the following aspects of the evolution of

the radiative energy are also revealed by the calculations. As described above, after the formation of the first focus, considerable power is transferred from the paraxial focal zone to the ring-shaped feature, which, at this stage in the evolution of the pulse, contains approximately 68% of its total initial power. This intense ring, which spreads away from the paraxial domain, produces a corresponding ring-shaped cavity in the electronic distribution [see Fig. 6(b)]. The refraction resulting from this strongly perturbed electron-density profile, together with the relativistic self-focusing mechanism, causes the wave to return energy to the core of the beam. Thus, the charge displacement produces a potent additional self-focusing action, which leads to the formation of a confined paraxial mode of high intensity stabilized along the axis of

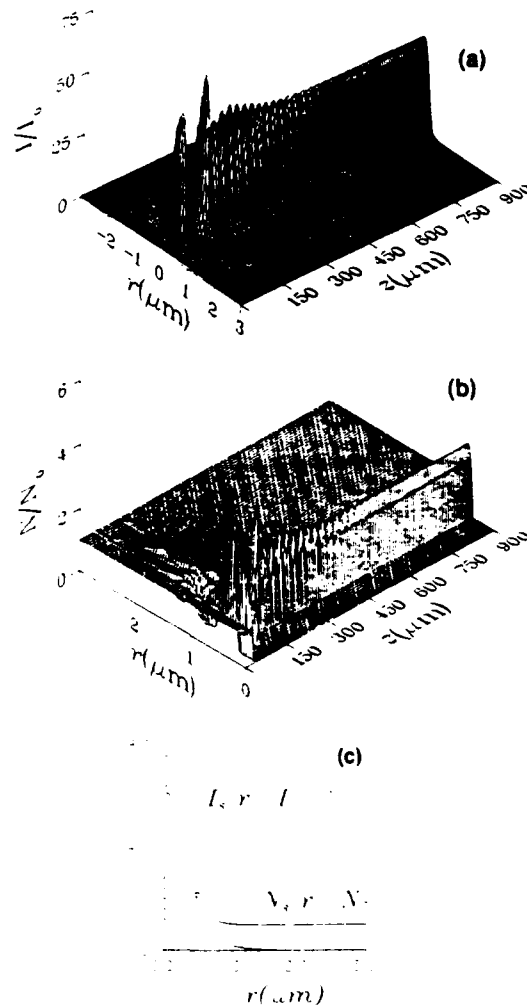


FIG. 6. The self-channeling of a pulse with a Gaussian initial transverse-intensity distribution [$N_2 = 2$ in Eq. (27)] and a flat incident wave front in initially homogeneous plasma in the case of the relativistic and charge-displacement propagation with $I_0 = 3 \times 10^{19} \text{ W/cm}^2$, $r_0 = 3 \mu\text{m}$, $\lambda = 0.248 \mu\text{m}$, and $N_0 = N_{e,0} = 7.5 \times 10^{20} \text{ cm}^{-3}$. (a) The distribution of the normalized intensity. (b) The distribution of the normalized electron density. (c) Radial dependence of the asymptotic solutions for the normalized amplitude $[I_s(r)/I_0]^{1/2}$ and the normalized electron density $N_e(r)/N_0$ for $s = 0.554$.

propagation. This phenomenon of confined propagation is designated as self-channeling. It should be noted that the calculations of the electrostatic energy associated with the charge displacement, which is given by the expression $W = 4^{-1} \int_0^{r_c} E_c^2 r dr$, with the electrostatic field E_c defined by the equation $\nabla E_c = -4\pi\rho$ and r_c designating the radial extent of the channel, show that this energy can be relatively small. Specifically, for the conditions represented in Fig. 6(b) [$z = 95.4 \mu\text{m}$], the electrostatic energy (W) accounts for only 0.18% of the total energy of the laser radiation per unit length.

The essential finding of these calculations is that the combined action of the relativistic and charge-displacement mechanisms produces a strong tendency for the generation of spatially highly confined modes of propagation which are *stabilized* along the axis of propagation. Furthermore, the study of a range of other cases indicates that these modes are exceptionally stable and that a considerable fraction of the incident power can be confined in them. The result is the controlled generation of a very high peak intensity in these channeled modes with values reaching $\sim 10^{21} \text{ W/cm}^2$ for the range of conditions studied.

Important characteristics of the asymptotic behavior of these confined modes have also been established. It has been shown that the distribution of the amplitude $u(r, z)$, for large values of z , tends asymptotically to the *lowest eigenmode* of the nonlinear Schrödinger equation (see Sec. III). Specifically, for the example discussed above, the computations have demonstrated that the asymptotic radial amplitude distribution corresponds to the lowest eigenmode with $s \approx 0.554$. In this case, the asymptotic intensity distribution $I_s(r) = U_{s,0}^2(r)$ contains 46% of the total incident power.

The normalized asymptotic field amplitude $[I_s(r)/I_0]^{1/2}$ and the corresponding normalized asymptotic plasma electron density $N_s(r)/N_0$ are depicted in Fig. 6(c). It should be noted that the profiles of the intensity $I(r, z)$ and the electron density $N(r, z)$, obtained as the results of the dynamical calculations of the propagation for $z \approx 900 \mu\text{m}$, differ from $I_s(r)$ and $N_s(r)$ for $s = 0.554$ by much less than 1%. In addition, we observe that the energy of charge displacement for $r_c = 2.5 \mu\text{m}$ in the asymptotic state accounts for a fraction of 9.45×10^{-4} of the total energy of the beam per unit length. We observe that this tendency for a solution of a nonlinear Schrödinger equation involving a saturable nonlinearity to converge to the lowest stationary solution was originally discovered by Zakharov, Sobolev, and Synakh [37].

For the range of parameters studied, the calculations clearly show that the charge displacement has a very strong influence on the character of the propagation after the first focus is formed. The pulsing intensity structure, consisting of alternating foci on the axis of propagation and peripheral focal rings, which is the usual behavior for the purely relativistic self-focusing (see Figs. 5(a) and 5(b)), is converted into a stabilized and uniform channel. Collaterally, a stabilized cavitated channel in the electron density is also formed. We remark that the periodic in-

tensity structure characteristic of the relativistic self-focusing occurs for great values of z and, therefore, may be regarded as the corresponding asymptotic solution of the purely relativistic case. The charge displacement leads to the formation of the asymptotic amplitude distribution represented by the corresponding lowest eigenmode $U_{s,0}(r)$ instead of this pulsing structure.

Computations have been also performed for the propagation of incident plateaulike wave forms with flat incident phase fronts in both homogeneous plasmas and plasma columns. Additional calculations, have also examined the behavior of focused Gaussian and plateaulike incident wave forms as well as defocused Gaussian incident wave forms in homogeneous plasmas (see Figs. 7–11). It is found that the main features described

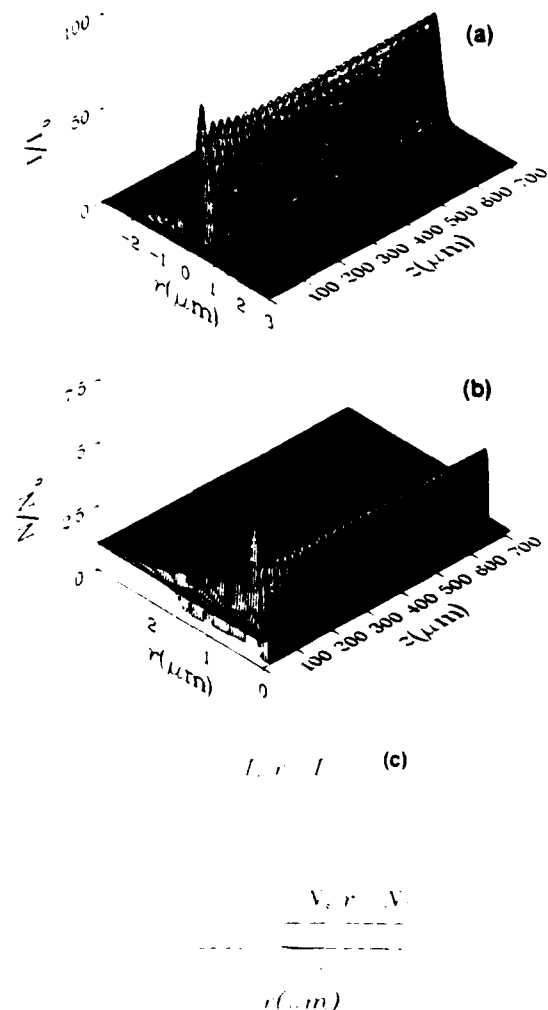


FIG. 7. The self-channeling of a pulse with a hyper-Gaussian incident-transverse-intensity distribution [$N_2 = 8$ in Eq. (27)] and a flat initial wave front in initially homogeneous plasma for the case of a relativistic and charge-displacement propagation with $I_0 = 3 \times 10^{19} \text{ W/cm}^2$, $r_0 = 3 \mu\text{m}$, $\lambda = 0.248 \mu\text{m}$, and $N_0 = N_{c,0} = 7.5 \times 10^{20} \text{ cm}^{-3}$. (a) The distribution of the normalized intensity. (b) The distribution of the normalized electron density. (c) Radial dependence of the asymptotic solutions for the normalized amplitude $[I_s(r)/I_0]^{1/2}$ and the normalized electron density $N_s(r)/N_0$ for $s = 0.515$.

above, namely (1) self-channeling, (2) stabilization of the mode of propagation, (3) the confinement of a substantial fraction of the incident power, and (4) the formation of paraxial cavitating channels in the electron distribution are common aspects of the dynamics over a wide range of conditions.

The character of these findings is now illustrated with five representative examples. For the propagation of a beam with an incident plateaulike transverse-intensity profile, given by Eq. (27) with $N_2 = 8$, which has a flat initial wave front incident on an initially homogeneous plasma (the values of the parameters have been adopted from above and $P_0/P_{cr} = 20.168$), the asymptotic radial profile of the intensity distribution contains approximately 77% of the incident power [Fig. 7(a)]. The corresponding asymptotic amplitude is the lowest eigenmode of the nonlinear Schrödinger equation with $s \approx 0.515$. The propagation of the same wave form in a plasma column, with the initial electron distribution defined by Eq. (29) with $N_3 = 8$ and $r_* = r_0$, results in a quasistabilized intensity distribution containing 34% of the incident power [Fig. 8(a)]. The purely relativistic propagation of incident plateaulike pulses [$N_2 = 8$ in Eq. (27)] in plasma columns [$N_3 = 8$ and $r_* = r_0$ in Eq. (29)] also results in the formation of quasistabilized regimes which, in this case, arise dynamically from the defocusing action of the refraction

generated by the transverse profiles of the electron density [24]. For this situation, approximately 25% of the total incident power is confined [Fig. 5(d)]. The comparison of these cases with the two examples discussed above involving the charge-displacement mechanism indicates that the increase in the value of the confined power stems principally from the substantial additional focusing action arising from the inhomogeneous electron distribution produced by the ponderomotive force.

Overall, the computations reveal that the charge displacement, which generally results in electronic cavitation, plays an important role in stabilizing the mode of confined propagation that develops dynamically. This stabilization naturally occurs by refraction of the radia-

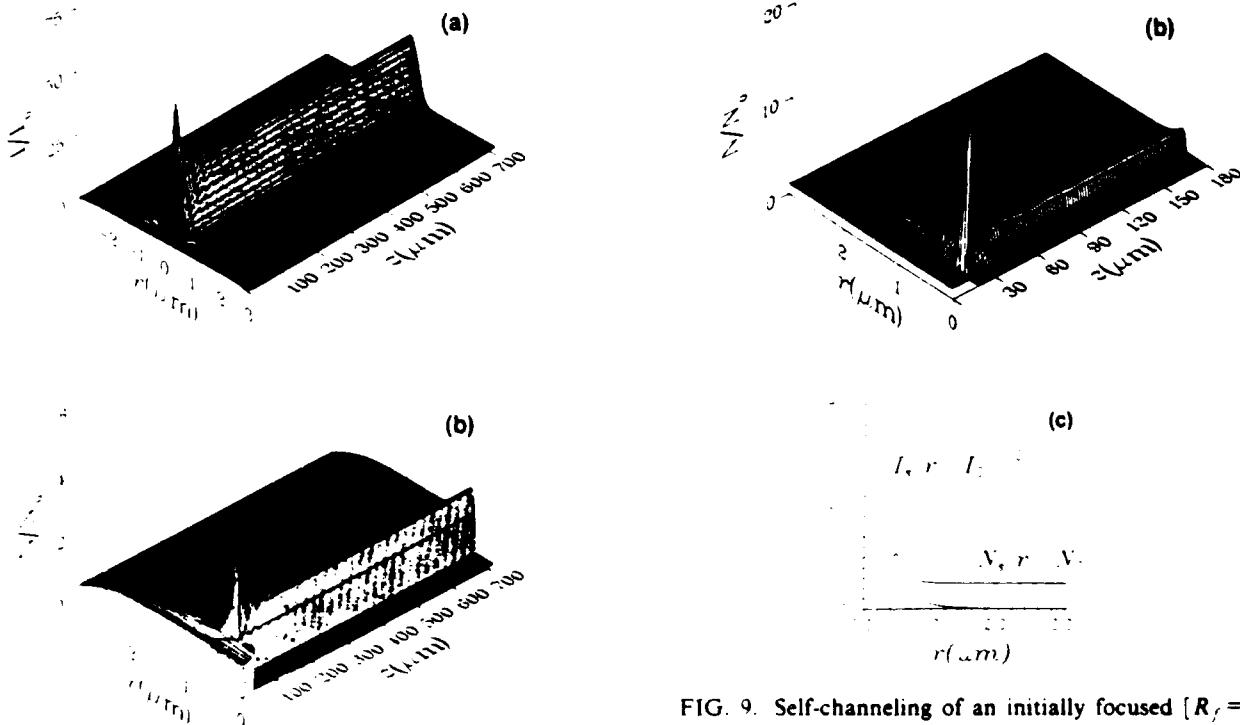


FIG. 8. The self-channeling of a pulse with a hyper-Gaussian incident-transverse-intensity distribution [$N_2 = 8$ in Eq. (27)] and a flat initial wave front in a preformed column-shaped plasma [$N_3 = 8$, $r_* = r_0$ in Eq. (29)] for the case of relativistic and charge-displacement propagation with $I_0 = 3 \times 10^{19}$ W/cm², $r_0 = 3$ μ m, $\lambda = 0.248$ μ m, and $N_0 = N_{cr} = 7.5 \times 10^{20}$ cm⁻³. (a) The distribution of the normalized intensity. (b) The distribution of the normalized electron density.

FIG. 9. Self-channeling of an initially focused [$R_f = R_{cr}/2$ in Eq. (35)] pulse with a Gaussian incident-transverse-intensity distribution [$N_2 = 2$ in Eq. (35)] in initially homogeneous plasma for the case of relativistic and charge-displacement propagation with $I_0 = 3 \times 10^{19}$ W/cm², $r_0 = 3$ μ m, $\lambda = 0.248$ μ m, and $N_0 = N_{cr} = 7.5 \times 10^{20}$ cm⁻³. (a) The distribution of the normalized intensity. (b) The distribution of the normalized electron density. (c) Radial dependence of the asymptotic solutions for the normalized amplitude $[I_e(r)/I_0]^{1/2}$ and the normalized electron density $N_e(r)/N_0$ for $s = 0.566$.

tion into the central paraxial region. Indeed, the influence of the charge displacement on the propagation is so strong that self-channeling occurs even in the cases of *extremely* focused and defocused incident wave forms. The results of the corresponding calculations for extremely focused incident wave forms, for $R_f = R_{f,0}/2$ [Eq. (35)], with both Gaussian [$N_2 = 2$ in Eq. (35)] and plateaulike [$N_2 = 8$ in Eq. (35)] incident-transverse-intensity distributions, are depicted in Figs. 9 and 10, respectively (the parameters of beam and plasma being the same as the other examples above). In these two cases, the asymptotic transverse profiles of the amplitude and the electron density are found to correspond to the lowest eigenmodes of the nonlinear Schrödinger equation with values of the parameter $s \approx 0.566$ (Fig. 9) and $s \approx 0.505$

(Fig. 10). Note, in strong contrast to the situation involving charge displacement, the analogously strongly focused incident wave forms for the purely relativistic case propagate in the single-focus regime [Fig. 5(c)], and stable confinement does not develop.

Figure 11 illustrates the relativistic and charge-displacement propagation of an initially strongly defocused wave form [$R_f = -R_{f,0}/2$ in Eq. (35)] having a Gaussian initial transverse-intensity distribution [$N_2 = 2$ in Eq. (35)]. After the initial stage of the defocusing, this pulse evolves into a paraxial structure that is analogous to those described above. Furthermore, in this example the asymptotic transverse profiles of the amplitude and the electron density are found to correspond to the lowest eigenmode of the nonlinear Schrödinger equation with

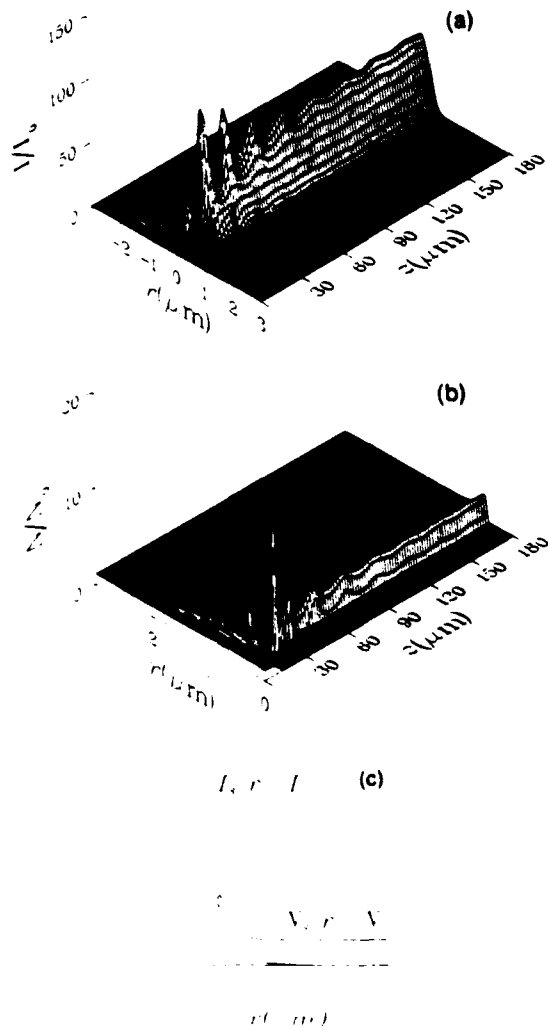


FIG. 10. The self-channeling of an initially focused [$R_f = R_{f,0}/2$ in Eq. (35)] pulse with a hyper-Gaussian incident-transverse-intensity distribution [$N_2 = 8$ in Eq. (35)] in initially homogeneous plasma for the case of relativistic and charge-displacement propagation with $I_0 = 3 \times 10^{19}$ W/cm², $r_0 = 3$ μm, $\lambda = 0.248$ μm, and $N_0 = N_{c,0} = 7.5 \times 10^{20}$ cm⁻³. (a) The distribution of the normalized intensity. (b) The distribution of the normalized electron density. (c) Radial dependence of the asymptotic solutions for the normalized amplitude $[I_e(r)/I_0]^{1/2}$ and the normalized electron density $N_e(r)/N_0$ for $s = 0.505$.

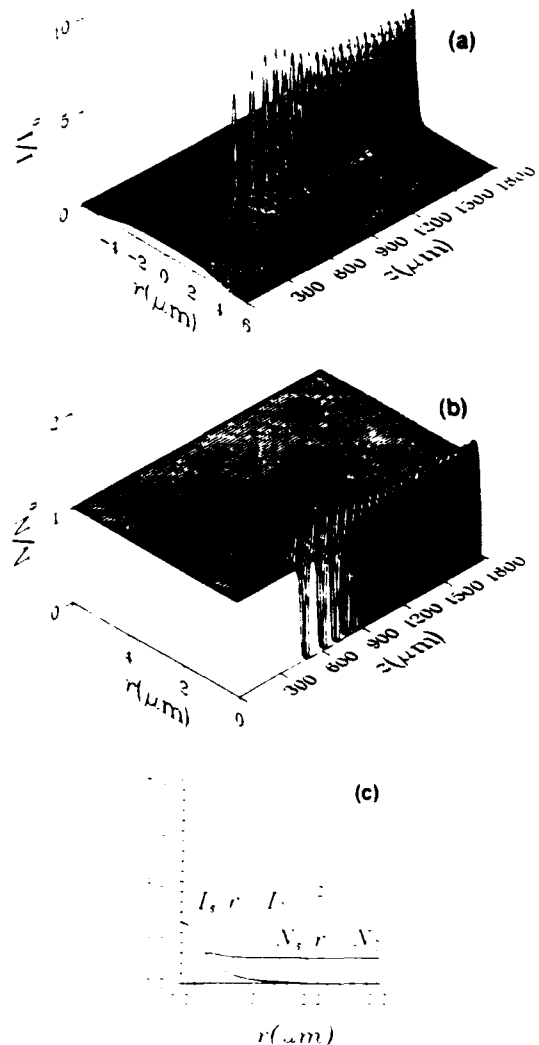


FIG. 11. The self-channeling of an initially defocused [$R_f = -R_{f,0}/2$ in Eq. (35)] pulse with a Gaussian incident-transverse-intensity distribution [$N_2 = 2$ in Eq. (35)] in initially homogeneous plasma for the case of relativistic and charge-displacement propagation with $I_0 = 3 \times 10^{19}$ W/cm², $r_0 = 3$ μm, $\lambda = 0.248$ μm, and $N_0 = N_{c,0} = 7.5 \times 10^{20}$ cm⁻³. (a) The distribution of the normalized intensity. (b) The distribution of the normalized electron density. (c) Radial dependence of the asymptotic solutions for the normalized amplitude $[I_e(r)/I_0]^{1/2}$ and the normalized electron density $N_e(r)/N_0$ for $s = 0.800$.

$s \approx 0.800$.

For these values of the dimensionless parameters assumed in these examples (Figs. 9–11) ($a_1 = 248.6192$, $a_2 = \frac{1}{3}$, that is $P_0/P_{cr} = 22.252$ for Gaussian incident wave form), the magnitude of the quantity $R_f = R_{f,0}/2$, the factor determining the degree of the initial focusing (defocusing), is 0.124. For $\lambda = 0.248 \mu\text{m}$ and $r_0 = 3 \mu\text{m}$, the focusing distance $R = kr_0^2 R_{f,0}/2$, used in the examples above, has a magnitude of $28.35 \mu\text{m}$. The fact that the self-channeling of such extremely focused or defocused distributions occurs (Figs. 9–11) means the self-channeling should be expected to be nearly independent of the initial conditions of focusing or defocusing.

A critical power P_{cr} for self-channeling arising from the relativistic charge-displacement mechanism can be defined. We now discuss this issue with a model developed in an earlier study. The threshold power P_{cr} is defined as the power that separates the asymptotic behavior, with respect to large distance of propagation (z), into two distinct classes. Since its definition rests on an asymptotic property, it can only exist in the limiting case of vanishing losses ($\mu = 0$ in Ref. [24]). For a power $P < P_{cr}$, the asymptotic transverse-intensity profile tends to zero at large z . In contrast, for $P \geq P_{cr}$ the asymptotic profile of the intensity tends to the lowest eigenmode of the governing nonlinear Schrödinger equation. Addition-

ally, the normalized value of this critical power is exactly twice the corresponding normalized value of the critical power for the Kerr effect self-focusing found in cubic media for initially flat wave forms [34,37]. The expression corresponding to this critical power [36] for the relativistic and charge-displacement mechanism is

$$P_{cr} = (m_{e,0}^2 c^5 / e^2) \int_0^\infty g_0^2(\rho) \rho d\rho (\omega / \omega_{p,0})^2 \\ \approx 1.6198 \times 10^{10} (\omega / \omega_{p,0})^2 \text{ W}, \quad (36)$$

where $g_0(\rho)$ is the Townes mode [34].

It has also been shown that the value of the relativistic and charge-displacement self-channeling threshold power, in cases involving initially focused or defocused beams, exceeds P_{cr} and depends on the degree of the initial focusing or defocusing. For a given magnitude of the curvature of the wave front, the value of the threshold power for initially defocused beams is greater than that for initially focused beams. Finally, it has been shown both analytically and numerically that for self-channeling of an arbitrary wave form to occur, it is sufficient that the Hamiltonian of the purely relativistic case, considered as a functional of the initial transverse amplitude distribution, should be negative [36]. The precise statement for this condition is

$$P_2(u_0) = \int_0^\infty \left[\left| \frac{du_0}{dr} \right|^2 - a_1 \{ u_0^2 - (2/a_2) [(1 + a_2 u_0^2)^{1/2} - 1] \} \right] r dr < 0. \quad (37)$$

We now comment on the behavior of pulses having initial amplitude distributions $U_0(r)$ close to higher eigenmodes $V_{s,n}(r)$, $n \geq 1$. These higher modes generally are associated with electronically cavitated channels. The self-channeling in these cases could result in asymptotic distributions of intensity and electron density corresponding to certain higher eigenfunctions $I_{s,n}(r) = V_{s,n}^2(r)$, $N_{s,n}(r)$, $n \geq 1$. In particular, this conjecture has established an initial amplitude distribution $U_0(r)$, which is close to the first eigenmode $V_{s,1}(r)$ with $s = 0.544$. Direct numerical calculations showed that the asymptotic distributions of both intensity and electron density that evolved in this case correspond to the first eigenmode $I_{s,1}(r) = V_{s,1}^2(r)$, $N_{s,1}(r)$ with s essentially equal to 0.544. It should be additionally noted, however, that these higher eigenmodes ($n \geq 1$) are quite possibly unstable against small azimuthal perturbations that destroy their axial symmetry.

The principal result of this section is the finding that the combined action of the relativistic and charge-displacement mechanisms can result in self-channeling with the formation of stabilized paraxial modes over a rather wide range of physical conditions. Moreover, these spatially confined modes are generally associated with corresponding cavitated channels in the electron density. Finally, the characteristics of these channeled

modes have asymptotic behavior that is described by the appropriate lowest eigenmodes of the governing nonlinear Schrödinger equation.

V. CONCLUSIONS

A theoretical approach suitable for the numerical investigation of the two-dimensional (r, z) dynamics of propagation of coherent ultrashort ($\tau_i \gg \tau \gg \tau_e$) relativistic laser pulses in cold underdense plasmas has been developed. Four basic physical phenomena are included within the scope of this method. They are (1) the nonlinear dependence of the index of refraction due to the relativistic increase in the mass of the electrons, (2) the variation of the index of refraction resulting from the perturbation of the electron density by the ponderomotive force, (3) the diffraction of the radiation, and (4) the refraction caused by nascent transversely inhomogeneous electron-density distributions. The equations studied in this work may be regarded as the generalization of those treated previously in other studies [18,19,33] involving initially inhomogeneous plasmas. Further studies are continuing with an extension of this analysis, which includes the azimuthal coordinate in the description of the propagation.

The main conclusions stemming from the calculations are the following.

(1) The cooperative effect of the relativistic and charge-displacement mechanisms leads asymptotically to stable high-intensity z -independent modes of self-channeling, and a major fraction of the incident power can be confined in these paraxial modes. Stable cavitation of the electron density is a general feature of these spatially confined modes.

(2) The z -independent modes, to which the solutions of the equation describing the relativistic and charge-displacement propagation tend asymptotically, are recognized as the *lowest* eigenmodes of the governing nonlinear Schrödinger equation.

(3) A separate study of purely relativistic propagation shows that beams with flat incident phase fronts exhibit a pulsing behavior in homogeneous plasmas but can undergo quasistabilization in suitably configured plasma columns. However, sufficiently sharply initially focused

beams generally exhibit the development of only a single focus. In significant contrast, the present study shows that with both the relativistic and charge-displacement mechanisms, initially focused beams also generally lead to confined modes of propagation. Finally, it should be noted that the equation for relativistic self-focusing can be considered as a general model equation of propagation in saturable nonlinear media.

ACKNOWLEDGMENTS

The authors acknowledge fruitful discussions with A. R. Hinds, R. R. Goldstein, and A. McPherson. Support for this research was provided by the U.S. Air Office of Scientific Research, the U.S. Office of Naval Research, the Strategic Defense Initiative Organization, the Army Research Office, the Department of Energy, and the National Science Foundation under Grant No. PHY-9021265.

*Present address: Department of Physics, University of Illinois at Chicago, Chicago, Illinois 60680.

- [1] U. Johann, T. Luk, H. Egger, and C. K. Rhodes, *Phys. Rev. A* **34**, 1084 (1986).
- [2] T. S. Luk, U. Johann, H. Egger, H. Pummer, and C. K. Rhodes, *Phys. Rev. A* **32**, 214 (1985); K. Boyer, T. S. Luk, J. C. Solem, and C. K. Rhodes, *ibid.* **39**, 1186 (1989).
- [3] A. I. Akhiezer and R. V. Polovin, *Zh. Eksp. Teor. Fiz.* **30**, 915 (1956) [*Sov. Phys. JETP* **3**, 696 (1956)].
- [4] R. Noble, *Phys. Rev. A* **32**, 460 (1985).
- [5] A. Magneville, *J. Plasma Phys.* **44**, 231 (1990).
- [6] S. V. Bulanov, V. I. Kirsanov, and A. S. Sakharov, *Fiz. Plazmy* **16**, 935 (1990) [*Sov. J. Plasma Phys.* **16**, 543 (1990)].
- [7] P. Sprangle, E. Esarey, and A. Ting, *Phys. Rev. Lett.* **64**, 2011 (1990); P. Sprangle, C. M. Tang, and E. Esarey, *Phys. Rev. A* **41**, 4663 (1990); A. Ting, E. Esarey, and P. Sprangle, *Phys. Fluids* **B2**, 1390 (1990).
- [8] L. D. Landau and E. M. Lifshits, *The Classical Theory of Fields* (Pergamon, New York, 1971).
- [9] E. S. Sarachik and G. T. Schappert, *Phys. Rev. D* **1**, 2738 (1970).
- [10] J. Krüger and M. Bovy, *J. Phys. A* **9**, 1841 (1976).
- [11] D. M. Volkov, *Z. Phys.* **34**, 250 (1935).
- [12] J. N. Bardsley, B. M. Penetrante, and M. H. Mittleman, *Phys. Rev. A* **40**, 3823 (1989).
- [13] C. Max, J. Arons, and A. B. Langon, *Phys. Rev. Lett.* **33**, 209 (1974).
- [14] G. Schmidt and W. Horton, *Comments Plasma Phys. Controlled Fusion* **9**, 85 (1985).
- [15] H. Hora, *Physics of Laser-Driven Plasmas* (Wiley, New York, 1981).
- [16] P. Sprangle and C. M. Tang, in *Laser Acceleration of Particles (the Norton Simon Malibu Beach Conference Center of the University of California, Los Angeles)*, Proceedings of the Second Workshop on Laser Acceleration of Particles, edited by C. Joshi and T. Katsouleas, AIP Conf. Proc. No. 130 (AIP, New York, 1985), p. 156.
- [17] P. Sprangle, C. M. Tang, and E. Esarey, *IEEE Trans. Plasma PS-15*, 145 (1987).
- [18] Gou-Zheng Sun, E. Ott, Y. C. Lee, and P. Guzdar, *Phys. Fluids* **30**, 526 (1987).
- [19] T. Kurki-Suonio, P. J. Morrison, and T. Tajima, *Phys. Rev. A* **40**, 3230 (1989).
- [20] E. Esarey, A. Ting, and P. Sprangle, *Appl. Phys. Lett.* **53**, 1266 (1988).
- [21] W. B. Mori, C. Joshi, J. M. Dawson, D. W. Forslund, and J. M. Kindel, *Phys. Rev. Lett.* **60**, 1298 (1988).
- [22] P. Gibbon and A. R. Bell, *Phys. Rev. Lett.* **61**, 1599 (1988).
- [23] C. J. McKinstrie and D. A. Russell, *Phys. Rev. Lett.* **61**, 2929 (1988).
- [24] A. B. Borisov, A. V. Borovskiy, V. V. Korobkin, A. M. Prokhorov, C. K. Rhodes, and O. B. Shiryayev, *Phys. Rev. Lett.* **65**, 1753 (1990).
- [25] J. C. Solem, T. S. Luk, K. Boyer, and C. K. Rhodes, *IEEE J. Quantum Electron.* **25**, 2423 (1989).
- [26] A. B. Borisov, A. V. Borovskiy, V. V. Korobkin, A. M. Prokhorov, O. B. Shiryayev, T. S. Luk, J. C. Solem, K. Boyer, and C. K. Rhodes (unpublished); A. B. Borisov, A. V. Borovskiy, V. V. Korobkin, A. M. Prokhorov, O. B. Shiryayev, J. C. Solem, K. Boyer, and C. K. Rhodes (unpublished); A. B. Borisov, A. V. Borovskiy, V. V. Korobkin, A. M. Prokhorov, O. B. Shiryayev, and C. K. Rhodes, *Kratkie Soobsheniya po Fizike*, No. 9, 3 (1991) (in Russian).
- [27] A. B. Borisov, A. V. Borovskiy, V. V. Korobkin, A. M. Prokhorov, O. B. Shiryayev, X. M. Shi, T. S. Luk, A. McPherson, J. C. Solem, K. Boyer, and C. K. Rhodes (unpublished).
- [28] T. S. Luk and C. K. Rhodes, *Phys. Rev. A* **38**, 6188 (1988).
- [29] G. A. Askaryan, *Zh. Eksp. Teor. Fiz.* **42**, 1567 (1962) [*Sov. Phys. JETP* **15**, 1088 (1962)].
- [30] T. S. Luk, A. McPherson, K. Boyer, and C. K. Rhodes, *Opt. Lett.* **14**, 1113 (1989).

- [31] A. J. Taylor, C. R. Tallman, J. P. Roberts, C. S. Lester, T. R. Gosnell, P. H. Y. Lee, and G. A. Kyrala, *Opt. Lett.* **15**, 39 (1990).
- [32] P. Maine, D. Strickland, P. Bado, M. Pessot, and G. Mourou, *IEEE J. Quantum Electron.* **24**, 398 (1988).
- [33] P. Sprangle, A. Zigler, and E. Esarey, *Appl. Phys. Lett.* **58**, 345 (1991).
- [34] R. Y. Chiao, E. Garmire, and C. H. Townes, *Phys. Rev. Lett.* **13**, 479 (1964).
- [35] H. A. Haus, *Appl. Phys. Lett.* **8**, 128 (1966).
- [36] A. B. Borisov, A. V. Borovskiy, V. V. Korobkin, A. M. Prokhorov, O. B. Shiryayev, and C. K. Rhodes, *J. Laser Phys.* **1**, 103 (1991).
- [37] V. E. Zakharov, V. V. Sobolev, and V. S. Synakh, *Zh. Eksp. Teor. Fiz.* **60**, 136 (1971) [*Sov. Phys. JETP* **33**, 77 (1971)].
- [38] A. B. Borisov, A. V. Borovskiy, V. V. Korobkin, C. K. Rhodes, and O. B. Shiryayev (unpublished); A. B. Borisov, A. V. Borovskiy, V. V. Korobkin, C. K. Rhodes, and O. B. Shiryayev, in *Short Wavelength Lasers and Their Applications*, edited by V. V. Korobkin and M. Yu. Romanovskiy (Nova Science, Commack, NY, 1992), p. 261.

Appendix H: "X-Ray Amplifier Energy Deposition Scaling with Channeled Propagation"

X-RAY AMPLIFIER ENERGY DEPOSITION SCALING WITH CHANNELED PROPAGATION +

K. Boyer*, T. S. Luk*, A. McPherson*, X. Shi*, J. C. Solem**, C. K. Rhodes*,
A. B. Borisov†, A. V. Borovskiy††, O. B. Shiryaev†, V. V. Korobkin ††

* Department of Physics, University of Illinois at Chicago, Chicago, IL 60680, USA.

** Theoretical Division, Los Alamos National Laboratory, Los Alamos, NM 87545, USA.

† Laboratory for Computer Simulation, Research Computer Center, Moscow State University, Moscow, 119899, RUSSIA

†† General Physics Institute, Academy of Sciences RUSSIA, Moscow, 117942, RUSSIA.

Abstract

The spatial control of the energy deposited for excitation of an x-ray amplifier plays an important role in the fundamental scaling relationship between the required energy, the gain and the wavelength. New results concerning the ability to establish confined modes of propagation of short pulse radiation of sufficiently high intensity in plasmas lead to a sharply reduced need for the total energy deposited, since the concentration of deposited power can be very efficiently organized.

I. Discussion of Research

Recent theoretical^{1,2} and experimental³ studies have led to a fundamental development concerning the generation of high-brightness x-ray sources. These results affect our ability to controllably apply very high power densities in materials, the basic issue for the creation of bright and efficient sources of radiation in the x-ray range. The main significance of this work is the establishment of the scaling law concerning the energy requirements for x-ray amplification in the kilovolt range shown in Fig. 1. Importantly, the parameters represented in Fig. 1, and which define the relationship presented, are based on both theoretical and experimental information.

The critical governing issue, which determines the scaling relationship between the required excitation energy (E) and the amplifier gain (G) of x-ray lasers, is the spatial control of the deposited energy. The information presented in Fig. 2 shows that optimizing the gain (G) per unit energy (E) calls for the guided mode of propagation in order to optimally control the deposition of the energy.⁴ Overall, in comparison to traditional forms of excitation, for a fixed x-ray energy output (E_x) and wavelength (λ_x), a reduction of several orders of magnitude in the necessary energy (E) results, as shown in Fig. 1, if this form of confined (channeled) propagation can be achieved. Therefore, if this scaling holds, a relatively small and useful laboratory-scale technology becomes feasible.

Recent experiments,³ which are supported by carefully developed theoretical analysis,¹⁻² have demonstrated the basic physics of a new form propagation exactly of the type necessary for the implementation of x-ray lasers of a fundamentally new regime of electromagnetic propagation is expected to arise in plasmas for short-pulse radiation at sufficiently high intensity. Dynamical calculations of the propagation in plasmas, incorporating both relativistic^{1,5} and charge-displacement mechanisms,^{2,6-9} indicate that the combined action of these processes can lead to a new stable form of spatially channeled propagation. Specifically, these experimental studies which have examined a new relativistic regime of high-intensity short-pulse propagation in plasmas, present evidence for the information of such a stable mode of spatially confined (channeled) propagation. For an electron density of $\sim 1.35 \times 10^{21} \text{ cm}^{-3}$ and a power of $\sim 3 \times 10^{11} \text{ W}$, the results indicate a channel radius $< 1 \text{ } \mu\text{m}$ and a peak intensity $\sim 10^{19} \text{ W/cm}^2$. Comparison of these findings with

+ To be published in Proceedings of the International Conference on Lasers '91,
edited by S. J. Duarte and D. G. Harris

Energy (E)/Wavelength (λ) Scaling

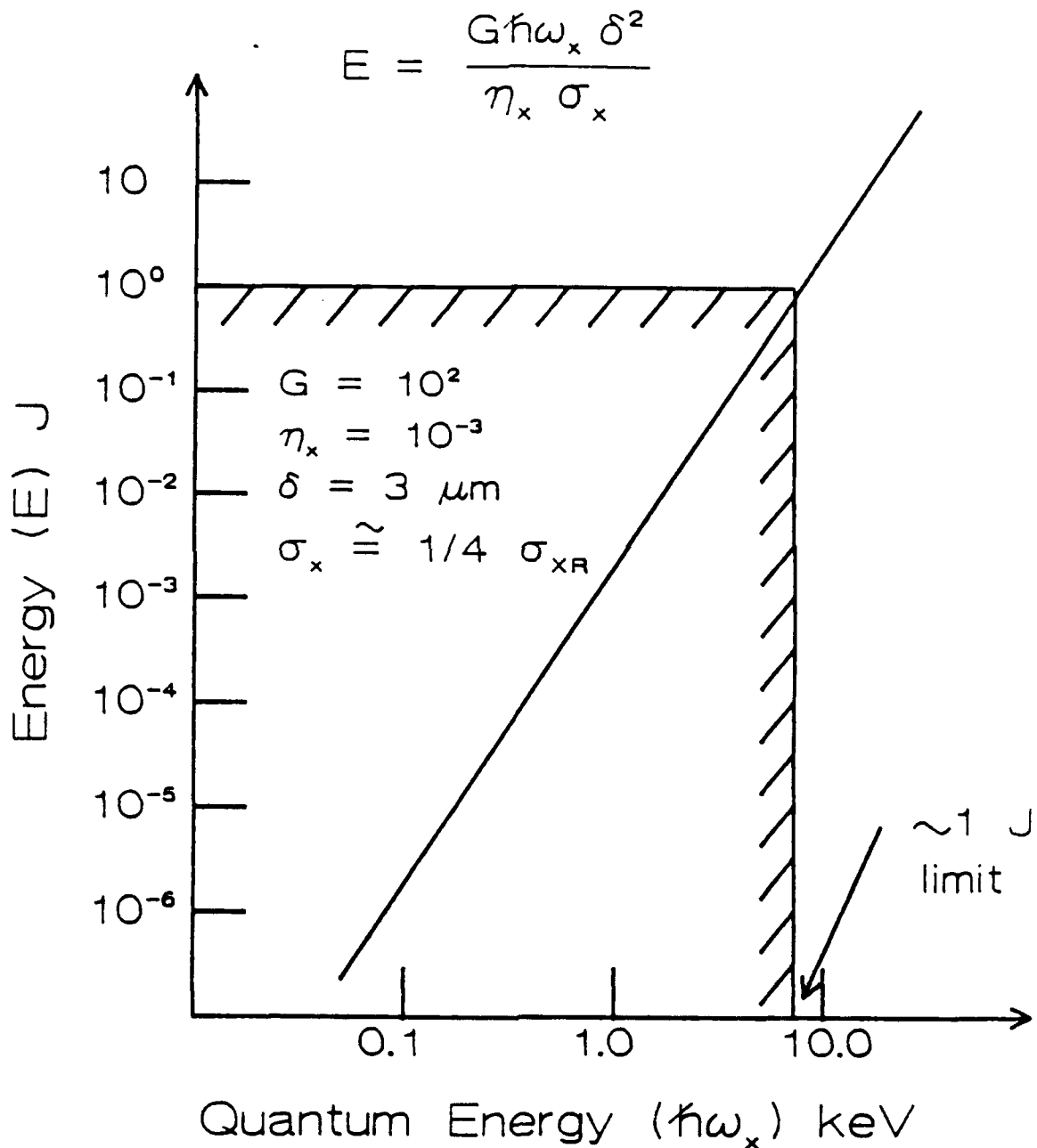
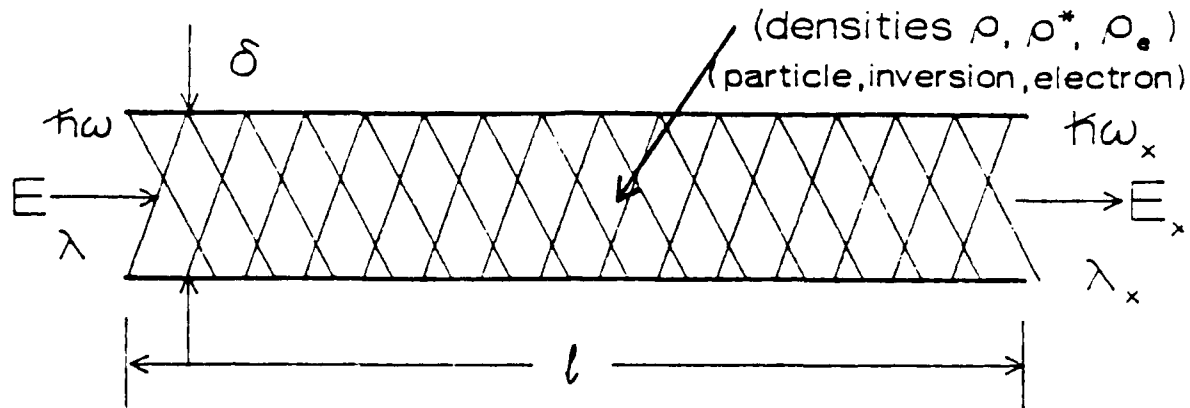


Fig. 1: Scaling relationship between required excitation energy (E) and quantum energy ($\hbar\omega_x$), characteristic of the amplifier. Parameters: total gain exponent $G = 100$, energy efficiency $\eta_x = 10^{-3}$, channel diameter $\delta = 3 \mu\text{m}$, x-ray ($\hbar\omega_x$) cross section for stimulated emission σ_x , x-ray cross section for stimulated emission for radiatively-broadened transition σ_{xR}

X-Ray Laser Scaling

Spatial Distribution/Amplifying Volume



$$E = \frac{\hbar\omega_x \rho^* \delta^2 l}{\eta_x}$$

$$G = \rho^* \sigma_x l$$

Laboratory Scale Technology--

$$\frac{G}{E} = \frac{\eta_x \sigma_x}{\hbar\omega_x \delta^2} \quad \Rightarrow \quad \text{small } \delta$$

\therefore Large l/δ , but $\delta \geq \sqrt{\lambda l}$ free space propagation

Really want to set--

$l \gg$ Rayleigh range $l_R \sim \delta^2 / \lambda$

$l \sim$ loss length

δ small

ρ^* large as possible

\therefore **Guided Mode of Propagation**

Fig. 2: Spatial distribution of energy of excitation (E) for an x-ray ($\hbar\omega_x$) amplifier. Parameters are the same as in Fig. 1 with λ the wavelength of the excitation energy, assumed longitudinally delivered, and with ρ , ρ^* , and ρ_e representing the particle, inversion and electron densities, respectively. The analysis shows that optimization of G/E requires a guided mode of propagation so that high concentrations of power can be organized in high-aspect-ratio spatial volumes.

a dynamical theory² yield close agreement for both the longitudinal structure and the radial extent of the propagation observed. These results represent a profound change in the field of x-ray laser research because they alter drastically the fundamental scaling relationships among the relevant physical variables.

The implications of this development for general applications to x-ray imaging and the micro-characterization of condensed matter are extremely important and propitious. In terms of the x-ray source, they are (1) that a properly controlled energy deposition rate, sufficient for the production of stimulated x-ray sources up to a few kilovolts in quantum energy, can now be achieved with an excitation energy of ~ 1 J, (2) that an x-ray output energy of ~ 1 mJ per pulse is achievable with laboratory-scale technology, and (3) that an x-ray beam diameter ($\sim 2 - 3$ μ m) arises as a natural consequence of the physics. These parameters represent an exceptionally high peak brightness figure that permits a new and completely unexplored range of physical measurements to be made. Indeed, a high-brightness source of this nature is ideal for the microimaging of condensed matter. In particular, an x-ray source with these parameters is perfectly matched to the requirements for holographic imaging of biological materials¹⁰⁻¹⁴ in terms of all its relevant properties, specifically, wavelength (10 - 40 Å), pulse energy (~ 1 mJ), pulse length ($\sim 10^{-13}$ s), beam diameter ($\sim 2 - 3$ μ m), and divergence (~ 1 mrad).

II. Conclusion

Recent experimental and theoretical results on electromagnetic propagation at high intensities in plasmas lead to very favorable scaling relationships for high-brightness x-ray amplifiers. Such x-ray sources will have important applications in the holographic imaging of biological materials.

III. Acknowledgements

The authors acknowledge the expert technical assistance of J. Wright and P. Noel in addition to fruitful conversations with A. R. Hinds, R. R. Goldstein, and B. Bouma. Support for this research was partially provided under contracts AFOSR-89-0159, (ONR) N00014-91-J-1106, (SDI/NRL) N00014-91-K-2013, (ARO) DAAL 3-91-G-0174, (DoE) DE-FG02-91ER1208, and (NSF) PHY-9021265.

IV. References

1. A. B. Borisov, A. V. Borovskiy, V. V. Korobkin, A. M. Prokhorov, C. K. Rhodes, and O. B. Shiryayev, "Stabilization of Relativistic Self-Focusing of Intense Subpicosecond Ultraviolet Pulses in Plasmas", Phys. Rev. Lett. **65**, 1753 (1990).
2. A. B. Borisov, A. V. Borovskiy, O. B. Shiryayev, V. V. Korobkin, A. M. Prokhorov, J. C. Solem, T. S. Luk, K. Boyer, and C. K. Rhodes, "Relativistic and Charge-Displacement Self-Channeling of Intense Ultrashort Laser Pulses in Plasmas", Phys. Rev. A, in press.
3. A. B. Borisov, A. V. Borovskiy, V. V. Korobkin, A. M. Prokhorov, O. B. Shiryayev, X. M. Shi, T. S. Luk, A. McPherson, J. C. Solem, K. Boyer, and C. K. Rhodes, "Observation of Relativistic/Charge-Displacement Self-Channeling of Intense Subpicosecond Ultraviolet (248 nm) Radiation in Plasmas", Phys. Rev. Lett., submitted.
4. K. Boyer, A. B. Borisov, A. V. Borovskiy, O. B. Shiryayev, D. A. Tate, B. E. Bouma, X. Shi, A. McPherson, T. S. Luk, and C. K. Rhodes, "Methods of Concentration of Power in Materials for X-Ray Amplification", Appl. Optics, in press.
5. C. Max, J. Arons, and A. B. Langdon, "Self-Modulation and Self-Focusing of Electromagnetic Waves in Plasmas," Phys. Rev. Lett. **33**, 209 (1974).
6. J. C. Solem, T. S. Luk, K. Boyer, and C. K. Rhodes "Prospects for X-Ray Amplification with Charge-Displacement Self Channeling," IEEE J. Quantum Electron. QE-**25**, 2423 (1989).
7. P. Sprangle, E. Esarey, and A. Ting, "Nonlinear Theory of Intense Laser Plasma Interactions," Phys. Rev. Lett. **64**, 2011 (1990); Phys. Rev. A **41**, 4463 (1990); P. Sprangle, C. M. Tang,

- and E. Esarey, "Relativistic Self-Focusing of Short-Pulse Radiation Beams in Plasmas," *IEEE Trans. Plasma Sci.* 15, 145 (1987).
8. G. Z. Sun, E. Ott, Y. C. Lee, and P. Guzdar, "Self Focusing of Short Intense Pulses in Plasmas," *Phys. Fluids* 30, 526 (1987).
 9. T. Kurki-Suonio, P. J. Morrison, and T. Tajima, "Self-Focusing of an Optical beam in a Plasma," *Phys. Phys. Rev. A* 40, 3230 (1989).
 10. J. C. Solem and G. C. Baldwin, "Microholography of Living Organisms", *Science* 218, 229 (1982)
 11. W. S. Haddad, D. Cullen, K. Boyer, C. K. Rhodes, J. C. Solem and R. S. Weinstein, "Design for a Fourier-Transform Holographic Microscope," in X-Ray Microscopy II, D. Sayre, M. Howells, J. Kirz and H. Rarback, eds. (Springer-Verlag, Berlin, 1988) pp. 284-287.
 12. W. S. Haddad, J. C. Solem, D. Cullen, K. Boyer, and C. K. Rhodes, "A Description of the Theory and Apparatus for Digital Reconstruction of Fourier Transform Holograms," in Electronics Imaging '87, Advanced Printing of Paper Summaries, Vol. II (Institute for Graphic Communication, Inc., Boston, 1987) pp. 683-688.
 13. W. S. Haddad, D. Cullen, J. C. Solem, K. Boyer, and C. K. Rhodes, "X-Ray Fourier-Transform Holographic Microscope," in Short Wavelength Coherent Radiation: Generation and Applications, Vol. 2, R. W. Falcone and J. Kirz, eds. (Optical Society of America, Washington, D.C., 1988) pp. 284-289.
 14. W. S. Haddad, D. Cullen, J. C. Solem, J. W. Longworth, A. McPherson, K. Boyer, and C. K. Rhodes, "Fourier Transform Holographic Microscope", *Appl. Opt.*, in press.